Conceptual Design and Control of Walking and Transportation Assist Devices Considering Human Motion

July 2015

A thesis submitted in partial fulfilment of the requirements for the degree of
Doctor of Philosophy in Engineering

Keio University

Graduate School of Science and Technology
School of Integrated Design Engineering

Chuan Yang

Acknowledgements

I had a lot of help both during my Ph.D. researches and on the life path leading up to the degree.

First to my respectable advisor, Professor Toshiyuki Murakami, who in the span of three years helped shape me from a theoretical study rookie to a capable and confident researcher. No one has been more influential during my Ph.D. process than him. During my time at Keio, he has become a lifelong friend and mentor, someone I could always approach during the happy times and the sad. I admire his kind character and the high emotional quotient way he connects and relates to students.

I am grateful to all of the professors on my dissertation committee, Professor Kouhei Ohnishi and Professor Toru Namerikawa who are from the System Design Engineering, and Associate Professor Naomichi Ogihara from the Mechanical Engineering, thankfully agreed to sit on my committee and get acquainted with my research. In addition, I would like to thank Monbukagakusho of Japanese Government for its full scholarship.

I want to thank all my friends both inside and outside the lab who have been there throughout my time at Keio. In the past three years, I got a lot of help and useful comments given by members of Murakami laboratory for my Japan life and researches. Also, the kind and warm comments and suggestions given from the SUM seminars inspired and improved my researches. Thanks to Professor Hiroaki Nishi, Associate Professor Takahiro Yakoh and Associate Professor Seiichiro Katsura for their comments in the seminars. I still clearly remember that Mr. Hansheng Wang and Mr. Kiyotoshi Komuta who picked me up three years ago when I was the first time to Japan. For the other companionship, I must thank Mr. Bizzotto Davide, Dr. Yamashita Haruka and Mr. Jie Zhu. Thanks to them as well.

Finally, I would like to offer my most heartfelt thanks to my parents, my sister Cui and my girlfriend Nan, for always being there to support and encourage me.

July, 2015
Chuan Yang

Contents

List of Figures

List of Tables

Chapter 1

Introduction

As the aging population problem becomes increasingly significant, robots are being widely applied as walking assist devices for people suffering from walking disabilities. In this dissertation, three kinds of human walking assist and mobility devices are proposed from different points. All of them are designed for elderly or patients who want to move independently. The validity of the proposed approaches were confirmed through several experiments. Also, these studies will lay a foundation for their practical applications and commercialization in the future.

1.1 Motivation

Today, lacking in adequate care for the elderly, especially those who are walking with inconvenience is becoming a growing problem for the aging society. Especially in the rapidly aging Japanese society, the problem of population trend is not going well. Fig. 1-1 shows a population projection for Japan from 2015 [1]. It indicates that the population ratio of 65 years old and older will be 40% in 2060. On the other hand, the ratio of 0-19 years old will be 13%. It means that there will be a very serious shortage of young labor. The elderly must take care of themselves especially when they want to move. Thus in Japan, elderly with walking assisting devices are quite common. And surprisingly, from the statistical data of Japan Ministry of Health, Labour and Welfare, the number of deaths due to fall is more than the number of traffic accident deaths in recent Japanese daily life [2]. Fig. 1-2 shows the international home care and rehabilitation exhibition which is held in Japan every year. It is popular and the most prominent feature has been its visitors. The largest group was the general public (31%), and then people from the

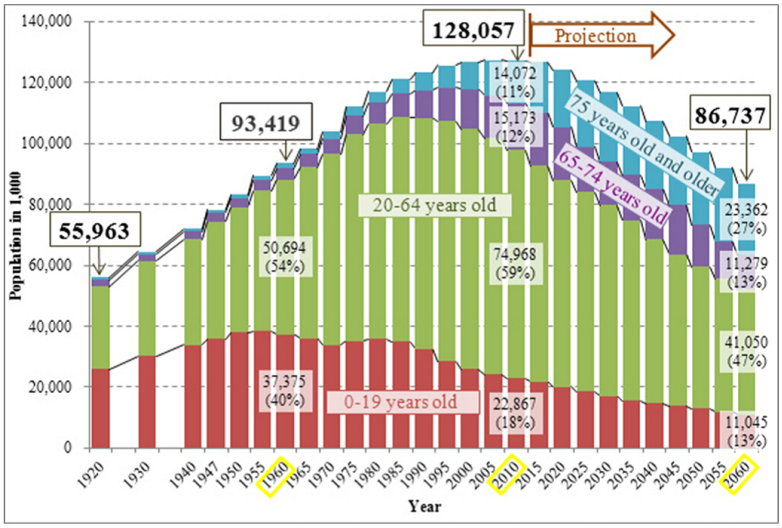

Data source : For data up to 2010, census data by Statistics Bureau of Ministry of Internal Affairs and Communication.
For the data from 2015, "Population Projection for Japan", by National Institute of Population and Social Security Research.

Fig. 1-1: Population trend by age group in Japan (1920-2060) [1].

Fig. 1-2: International home care and rehabilitation exhibition (in Japan) [3].

(a) Folding Walker (b) Lightweight Walkers

Fig. 1-3: Walk-assist devices of nursing plaza kohoku in Yokohama city.

the welfare institutions (16%) in 2014 [3]. This international exhibition is also the largest health and welfare exhibition in Asia. For the elderly or patients who want to move independently, there has been many kinds of products so far. Like wheelchairs, powered wheelchairs, powered three and four wheeled scooters, bicycles, walkers, canes, stretchers, transfer aids, floor lifts, ceiling/fixed lifts, stationary hoists, powered assist suits, walking assist robots, and so on. Most of the exhibition products are useful, but what are being used in practical applications now is also important. Therefore, the author visited a special nursing home for the elderly of Yokohama city in 2013. The name is “Nursing Plaza Kohoku”. Fig. 1-3 shows a folding walker and two lightweight walkers. All of them are mechanical equipments.

From the expostor’s words, the author got some useful information about walkers. For safety, convenient aid to performing daily activities, the walker can be a good solution. Fig. 1-3(a) combines the strength and durability with lightweight ease of use. Its U-shaped frame provides the user with good stability. The front two big wheels and rear small two wheels with brakes are for easy moving, and the brakes while the contoured hands push down make it safe to use. The lightweight walkers/rollators shown in Fig. 1-3(b) come with soft-grip caster tires are good for indoor and outdoor use. Their brake systems feature loop lock handles, making them the good walking aid for arthritic fingers. They also come with padded seats when the users need to sit down and rest. These mechanical equipments are widely used in home care and rehabilitation since they are inexpensive and convenient. However, they are difficult to be used in long distance or long time because they mechanical equipments require human force to move. On the other hand, they have no way to prevent users fall down. Obviously, it is very dangerous that the elderly or patients walking with inconvenience when they fall down. This also

Fig. 1-4: Honda's robot technologies [6].

explains that why there are so many new powered machines appearing in the international home care and rehabilitation exhibition. As the research target, different from the existing equipments, the author focuses on preventing fall down, ease of use and fast-safety movement. Thus this dissertation presents three kinds of human walking assist and mobility devices from these three points of view.

1.2 Related Works

Nowadays, lacking in adequate care for the elderly, especially those who are walking with inconvenience is becoming a growing problem for the aging society. It is very dangerous when the elderly who walking with inconvenience fall down. It is also necessary for the elderly to exercise walking in order to keep normal social life. While walking, elderly with little strength usually use canes to keep balance. Consequently, they can not balance their own bodies with one leg, making them walk in a very slow pace while having to step forward quite fast in order to keep balance. For the elderly with enough strength in their upper bodies, the canes do work. However, for those without enough strength, keeping balance is nearly impossible merely by canes. Therefore, kinds of powered walking assist devices are developed. In Japan, the most representative ones are walking assist devices of Honda Motor Company. Fig. 1-4 shows the Honda's robot technologies. Honda walking assist device with bodyweight support system [4] reduced the floor reaction force of the user was based on biomedical engineering analysis results. Honda prototype stride management assist device [5] was designed to help lift each leg at the thigh as it moves

forward and backward. It helps lengthen the user's stride, covering longer distances at a greater speed. The unicycle U3-X [6] of the future moves as rider's move, wheeling rider to rider's destination simply by sensing rider's body tilting this way or that, Segway style.

Inspired from the Honda's technologies of walking assist and mobility devices, the author proposed three kinds of powered devices from three different aspects. Firstly, in order to solve the elderly's problem of lacking in strength, many researchers have invented sorts of machine suits for elderly to put on. H. Herr with MIT Media Lab classified exoskeletons and orthoses into devices that act in series and in parallel to a human limb, providing a few examples within each category [7]. Y. Sankai et al. proposed an estimation algorithm that infers the intention related to the forward leg-swing in order to support the gait by HAL [8][9] robot suits. They are able to enhance human walking ability, but they paid little attention to keep elderly from fall down motion. D. Matsuura et al. proposed a motion control algorithm of walking assist machine using crutches [10]. M. Higuchi et al. developed a walking assist machine using crutches [11]. But both of them paid little attention to prevent elderly from fall down as well. In the first approach, the author proposed a novel walking assist multi-legged device that is fixed on the waist, with two machine legs independent from human legs, helps elders walk and climb stairs without any manipulation of the machine. In order to measure the human body posture and prevent from falling down, an inertial measurement unit (IMU) sensor fixed on the waist part of human is applied in this research. The IMU sensor contains a triaxial accelerometer, a triaxial gyro (angular rate sensor), and a triaxial magnetometer. Thus it can not only measure posture but also measure human walking motion. Y. Hirata et al.[12] focused on the support of walking on slope, and estimated slope angle based on accelerometer and force sensors. The method was able to apply to Wearable Walking Helper but it was a little complicated. In order to improve the reliability of the system, however, this approach introduces links with two encoders to measure human normal walking motion. To analyse the stability of the proposed multi-legged system, zero-moment point (ZMP) concept is used. C. Zhu et al.[13] analysed walking principle of biped robot was clarified by means of ZMP concept, friction constraint, and inverted pendulum model. A. Suzumura et al.[14] proposed a four-wheel-legged mobile robot, and the ZMP was introduced as a stability index. In the proposed device, based on the ZMP, the stability of the device is analyzed to confirm the feasibility and effectiveness of this device. In a word, the multi-legged device can help the elderly who have poor walking ability walk by themselves and give them simple walking exercise.

Secondly, since the conventional walking stick and four wheels handcart are needed moving by labour

power and the human's walking posture while using them are not healthy, to replace the labour's power, R. Annicchiarico *et al.* [15] proposed an intelligent pedestrian mobility aid which was base on force sensor and operated by human's hand. However, it is not easy to operate by the elderly whose hands have already tremble and lack of flexibility. Also, if the elderly whose feet don't have much physical strength to stand instability keep no attention, they are easy to fall down and that is dangerous undoubtedly. Nowadays, to help the elderly who have poor walking ability walking by themselves and exercising from the simple walking, a robot which can serve the elderly as a partner or a nurse to walk is needed. In order to achieve this target, detecting human walking motion and robot control strategy are needed. M. Watanabe *et al.* [16] proposed a method to assist human walking base on two-wheel mobile manipulator. The two-wheel robot had nice mobility, and the algorithm was base on force control. But it also needed labour power to moving. And it employed two encoder sensors tied on human's legs to obtain the walking distance. These led to a load for the elderly and a not ideal tracking result. To obtain a good walking distance measuring to track human's walking position, recently, there are numerous approaches has been proposed. Most of them employed sensors to obtain walking motion such as posture and velocity. N. Hata *et al.* [17] and H. Kawamoto *et al.* [18] proposed methods to get walker's motion information by some encoders tied on human's legs. They got good human's walking motion information. But these studies/assistive devices were focused on how to design the robotic structures as human-like as possible. For tacking a human's position, a much more simple and effective measurement method is needed. K. Sagawa *et al.* [19] proposed a approach to measure walking distance non-restrictedly by a 3-D inertial sensor. This wearable sensor was novel and got human's walking information for medical research successfully. O.H. Madgwick et al.[20] presented a novel orientation algorithm by a wearable inertial human motion tracking system. The results indicated the algorithm achieving levels of accuracy matching. However, they are not real-time systems and only for detecting human's walking motion. For counting steps and estimating walking distance more accurately, others researches also reported good results [21]-[27]. In these methods, the 3-D inertial and magnetic sensor was fixed at a foot toe of human and measured acceleration during swing phase of the feet. Their works got good results for tacking human's walking, but no one of them focused on the cooperation between human and mobile machines which must be a closed-loop control system. In the second approach, the author focus on obtaining a non-restricted measurement of walking distance by using an IMU sensor. However, the acceleration data from the inertial and magnetic sensor is noisy and always drift, Y.W. Guo *et al.* [28] proposed four kinds of filters (Median filter, Low-pass filter, Wavelet filter and Kalman filter) to reduce the acceleration signal

noise. It indicated that Kalman filter and Low-pass filter were appropriate to real-time system. C.Y. Lee *et al.* [29] also proposed a Butterworth filter which was easy to realized and similar as a Low-pass filter. To reduce the noise and drift of acceleration signal, a Butterworth filter and compliance control are needed. The second order Butterworth filter filtrated the noise and the compliance control are designed to compensate acceleration drift. Other researches [30]-[34] also proposed human body motion tracking methods by using small inertial/magnetic sensors. They also got some good measurement results by filtering. In addition, a manipulator fixed on this mobile robot can support and help the elderly with their walking. And it can compensate the moving position error between human and robot. This manipulator had two links, one link is used to correct moving distance error and the other one link can compensate the orientation error. The foot motion data process algorithm consists orientation estimation, walking acceleration estimation, and gait detection. Foot orientation command is obtained by Euler angles from the IMU sensor. Walking acceleration and velocity commands are accomplished by a Butterworth filter and compliance control. To make sure that robot is able to stop when human stop walking, gait detection with zero velocity updating is obtained by using a simple timer algorithm.

Thirdly, the author focus on the elderly who merely have limited walking ability so that robots can provide these people with walking or transportation support. With the development of new technology, self-balancing two-wheel electric bicycles with good flexibility were proposed and utilized as means of transportation. These transportation vehicles make possible the children and elderly could ride a bicycle or motorcycle very easily. A.V. Beznos *et al.* [35] described a bicycle with a gyroscopic stabilization capable of autonomous motion along a straight line as well as along a curve. B.T. Thanh *et al.* [36] proposed a structure-specified mixed $H_2/H\infty$ controller for a bicyrobo by the gyroscopic stabilizer too. By applying a mass balancer, the bicycle self-balancing can also be achieved. M. Yamakita *et al.* [37] and A. Murayama *et al.* [38] studied the automatic control of bicycle with a balancer. However, the gyroscopic stabilizer and mass balancer are so weighed that the electric power costs largely increased, and the cruising distance is accordingly reduced. Instead of the gyroscopic, H. Niki *et al.* [39] and Y. Tanaka *et al.* [40] proposed a self-balancing bicycle robot by steering controller. Also, J.D.G. Kooijman *et al.* [41] proposed a riderless bicycle can automatically steer itself so as to recover from falls. To improve the stability performance, L. Keo *et al.* [42] and T. Kimura *et al.* [43] proposed both balancer controlling and steering controlling for the bicycle stabilization. Adding a pose estimation, Y. Zhang *et al.* [44] [45] proposed a balance control for riderless the bicycle or motorcycle based on the steering controller. The nonlinear balance control for the one wheel steering systems was studied. They also got

Fig. 1-5: Some representative powered human walking assist and mobility devices.

some good experimental results. In order to analyze the stability, an integral and succinct dynamics of bicycles or motorcycles need to be studied. K.J. Astrom *et al.* [46] focused on the bicycle dynamics and control. Also, D.J.N. Limebeer and R.S. Sharp [47] proposed the modeling of bicycles and motorcycles. Based on the dynamics and steering controller, trajectory tracking is possible too. Y. Tanaka *et al.* [48] studied a straight-line tracking control for the bicycle. J. Yi *et al.* [49] proposed a trajectory tracking and balance stabilization control for autonomous motorcycles. S. Lee *et al.* [50] focused on self-stabilizing strategy in tracking control for unmanned electric bicycles. Other related researches [51]-[56] are also got some good results. However, all of the above studies only considered about the one steering electric bicycle system. All of the systems cannot keep self-balancing when they stopping or moving with slow speed due to the dynamics. To get a full speed range self-balancing electric motorcycle, in the third approach, the dynamics to keep the balance by two-wheel steering control for three different steering modes is studied. T. Kimura with Yamaha company *et al.* [57] developed a new mechanical two-wheel steering system for motorcycles. But the dynamics of this system was not included. C. Nakagawa *et al.* [58] proposed a personal mobility vehicle with two-wheel steering and two-wheel driving. However, it was also based on the theory of Segway, although a two-wheel steering was added. And it was not a self-balancing system. For a motorcycle system, the challenge is keeping the self-balancing even it stops. Segway [59] and two-wheel wheelchair [60] [61] [62] or wheeled mobile robot [63] have a good stability performance when they stop or move slowly. Also, in Murakami laboratory of Keio University, two-wheel driven wheelchairs [64]-[71] has been studied. Lyapunov method [72], sliding mode control [73], and other controllers [74]-[79] are utilized in these underactuated mechanical systems to realize self-balancing and robust control. In Murakami laboratory, the controllers based on disturbance compensators [80]-[84] were proposed too. The third research of this dissertation studied the self-balancing control method for the two-wheel electric bicycle system when it stops and moves with slow speed. In order to precisely measure the posture of the motorcycle, an IMU sensor is utilized in this research as well. Moreover, the proposal is a handy tool for the children and elders who want to ride a bicycle.

Fig. 1-5 shows some representative modern powered human walking assist and mobility devices. In accordance with the moving speed and supporting the objects' age, there is a main idea of research in the dissertation. In simple terms, the order of description of Fig. 1-5 is:

1) for 75 years older or walking difficultly objects, Fig. 1-5 (a) and Fig. 1-5 (b) support human body and help them walk slowly;

2) for 65 years older or walking relatively easily, Fig. 1-5 (c) and Fig. 1-5 (d) give a hand to human

and help human move at normal speed;

3) for younger objects who want to move faster and more convenient, Fig. 1-5 (e) and Fig. 1-5 (f) provide a convenient and quick transportation idea to help human moving.

The following section will introduce three approaches in this order. The design inspiration is from these devices, but the approaches are proposed to overcome some disadvantages of these existing devices.

1.3 Dissertation Approaches and Contributions

This dissertation makes several contributions to the novel human walking assist and mobility devices from different emphasis. Three different kinds of novel devices are proposed. Fig. 1-6 shows the three dissertation approaches. Also, all of the approaches are demonstrated experimentally. The detailed contributions for each approach are explained as following subsections.

1.3.1 Approach 1: Multi-legged walking assist device

In order to prevent the elderly fall down and enhance their walking ability, a novel walking assist multi-legged device that is fixed on the waist, with two machine legs independent from human legs, helps elders walk and climb stairs without any manipulation of the machine. In this proposed device, an IMU sensor is employed and fixed on the waist of the elder in order to gauge the posture of the waist thereby preventing an emergency such as a fall. Further, based on the ZMP conception, the stability of the device is analyzed to confirm the feasibility and effectiveness of this device. The primary contributions of the study are summarized as follows:

1) the kinematics modeling and dynamics modeling are introduced for this novel multi-legged system;

2) the controller of keeping the elders from falling down and help the them walk is proposed;

3) ZMP is introduced as a stability index for the system.

1.3.2 Approach 2: Walking assist cart operated by human foot

The first approach can prevent the elderly fall down but the moving speed is slow. Thus it is suitable for the elderly who have very poor walking ability. For the elderly who have a better walking ability but cannot walk without walking assist devices. This study presents a method for walking assist control that uses an IMU sensor fixed to an elderly person's foot to estimate his or her walking motion. In this proposed approach, a mobile device is synchronously driven by the user's walking motion. Furthermore,

(a) Multi-Legged Device (Approach 1)

(b) Novel Walk-Assist Cart (Approach 2)

(c) Self-Balancing Device (Approach 3)

Fig. 1-6: Dissertation approaches (left to right): the ability of movement speed is increasing.

a manipulator mounted on the mobile device can support and help the user walk. These functions make it possible for the device to move beside the user and coordinate with his or her steps. The validity of the proposed approach was confirmed through several experiments too. The contributions of this study can be generalized as:

1) human walking motion is measured by an IMU sensor;

2) the modeling of the proposed device is introduced;

3) the device performance are demonstrated by experiments.

1.3.3 Approach 3: Self-balancing two-wheel electric motorcycle

If one people want to move a long distance, a fast and safe mobility device is needed. Electric two-wheel motorcycle is very popular. But for the elderly, it is not an easy thing to ride a traditional electric motorcycle. Thus the self-balancing electric motorcycle should be a good solution. However, keeping the motorcycles balanced in full speed range, which is a valuable research to solve the above problem, has not been thoroughly researched. In this study, a novel self-balancing electric motorcycle without the handlebar is put forward to cover this deficiency. By controlling the steering, the balance of the motorcycle can be kept with its wheels swaying. And the motorcycle direction can be controlled by the rider's body. Also, three different steering phases of handleless motorcycles were discussed. The difference of these three modes were shown by the comparison experiments. In order to achieve a full

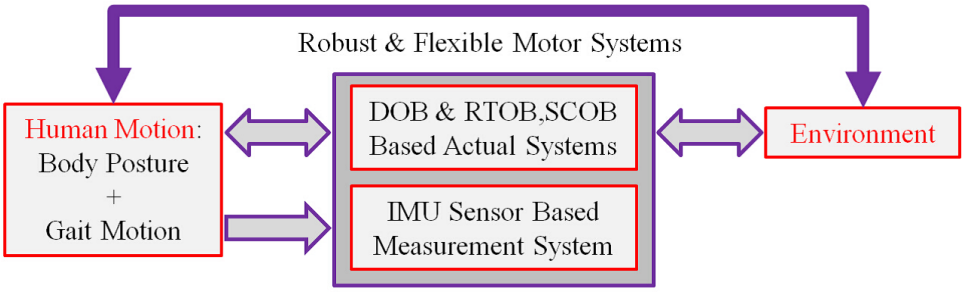

Fig. 1-7: General conception of the dissertation.

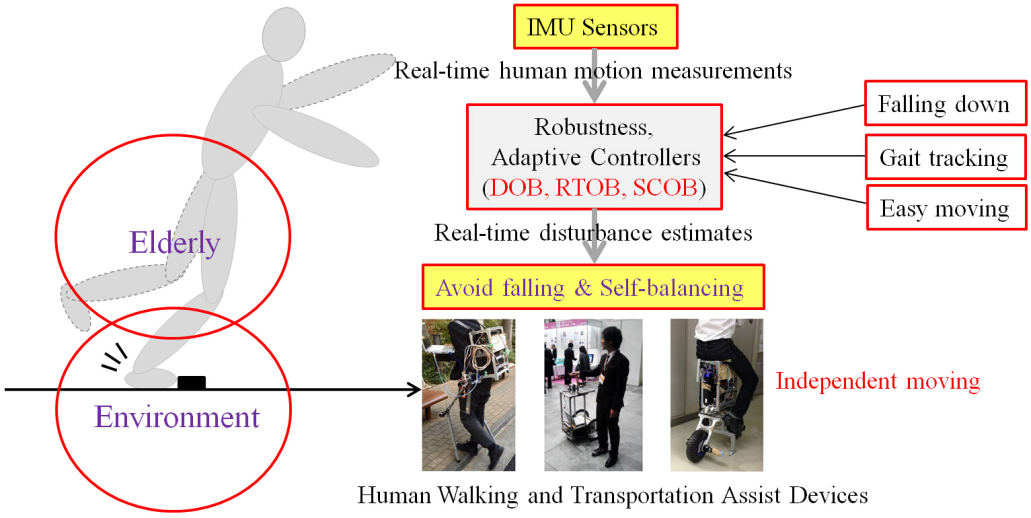

Fig. 1-8: Real applications of the general conception in the dissertation.

speed range self-balancing motorcycle system, two different modes were applied in zero/low speed and normal/high speed respectively. The stability of them were analysed, and some experimental results proved them as well. The contributions of this study are:

1) the dynamics are introduced for the proposed electric motorcycle in different modes;

2) the performance of the three kinds of steering working modes are compared;

3) a control strategy is introduced for the system without the handlebar at zero or low speed;

4) the stability for the system is analysed.

1.4 Dissertation Outline

Consider human motion and environment, Fig. 1-7 shows the general conception of the dissertation. Applying the three approaches, the real applications of the general conception is shown in Fig. 1-8. The

proposed walking and transportation assist devices let human avoid falling and move easy by adaptive controllers. Since the human motion accords to geographic coordinates of the IMU sensor, when the proposed devices are applied in variable environment, the mathematical definition of different environment such as stiffness, should be considered. However, in real applications, the mathematical definition of environment is very difficult to learn. This makes the adaptability of the approaches to be limited in different environment. The remainder of this dissertation is organized as follows:

Chapter 2: (Human Motion Measurement) focuses on human motion measurement by IMU sensor. In the man-machine coordination control, human motion or posture is an important information for machine controlling. In order to avoid the limitation in measurement, inertial sensors are the popular method to be applied. This chapter introduce the measurement method and explain why measure people's feet is more appropriate by a comparative experiment.

Chapter 3: (Observers) gives a detailed introduction to disturbance observer (DOB), reaction torque observer (RTOB) and synthesized camber angle disturbance observer (SCOB). DOB is widely used in motor control and motion control. With the pseudo differentiation, DOB can achieve high performance robust motor control systems. And the motors are indispensable roles in machine devices. As the extension of DOB, both RTOB and SCOB are based on the theory of it.

Chapter 4: (Body Balancing Assist Control) propose a novel multi-legged walking assist device which can keep the elders from falling down and help them walk. Modeling of this device is established firstly. Also, the stability of the device is analyzed by ZMP conception. The validity of this approach is confirmed through several experiments.

Chapter 5: (Partner's Cooperation Control) propose a novel walking assist robot which can serve the elders as a partner or a nurse, it can help the elders who have poor walking ability walking independently and exercising from the simple walking. Human walking behavior is estimated by the IMU Sensor. Using this measurement information, the device can be controlled by human foot easily. Kinematics, dynamics and experimental results are introduced as well.

Chapter 6: (Easy Moving and Self-Balancing Control) propose a novel self-balancing electric motorcycle without the handlebar. The balance of the motorcycle can be kept with its wheels swaying, and the direction can be controlled by the rider's body. In order to achieve a full speed range self-balancing motorcycle system, two different modes are applied in zero/low speed and normal/high speed respectively. The stability of them are analysed, and the final experimental results proved them.

Chapter 7: (Conclusions) provides a summary of the dissertation. This chapter also highlights the

contribution of the researches to the future society.

Chapter 2

Human Motion Measurement

2.1 Inertial Sensor and Quaternion

This dissertation focuses on the walking cooperation between human and robot. Thus the human motion measurement is an important issue. In the three approaches of this dissertation, all of them need human walking or posture motion information. In the past researches, most of the studies applied inertial sensors to measure human motion. In this chapter, IMU sensors made by x-io Technologies are utilized. Before discussing about topics in this dissertation, two IMU sensors that only for detecting human's walking motion is studied. One IMU sensor (IMU 1) is fixed on foot and the other one (IMU 2) is fixed on chest. In this testing, the human walks 9 steps on a straight and horizontal way. In the IMU sensor, a quaternion is applied to represent the orientation of a rigid body or coordinate frame in 3-D space. A quaternion (a, b, c, d) is a four-dimensional complex number. Fig. 2-1 shows an arbitrary orientation of frame h relative to frame w. $\boldsymbol{q}_h^w$ describes the arbitrary orientation and r is a unit vector described in frame w [20].

$$\boldsymbol{q}_h^w = [a \quad b \quad c \quad d] = [cos\frac{\sigma}{2} \ -r_x sin\frac{\sigma}{2} \ -r_y sin\frac{\sigma}{2} \ -r_z sin\frac{\sigma}{2}] \tag{2.1}$$

where r_x, r_y and r_z define the components of the unit vector $\boldsymbol{r}$ in the x, y and z axes of frame w respectively.

The Euler angles φ, θ and ψ describe an orientation of human body frame h achieved by the sequential rotations from alignment with earth world frame w. This Euler angles' representation can be calculated

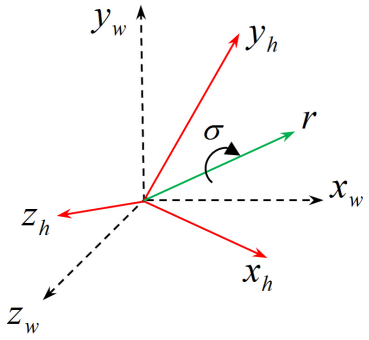

Fig. 2-1: Frame h rotates from frame w with angle σ around the axis r.

by the following equations.

$$\varphi = atan2(2cd - 2ab, 2a^2 + 2d^2 - 1) \tag{2.2}$$

$$\theta = -arctan(\frac{2bd + 2ac}{\sqrt{1 - (2bd + 2ac)^2}}) \tag{2.3}$$

$$\psi = atan2(2bc - 2ad, 2a^2 + 2b^2 - 1) \tag{2.4}$$

2.2 Calibration Method

After obtaining the Euler angles, raw acceleration data must be filtered. The accelerometer magnitude $\alpha_m$is computed by,

$$\alpha_m = \sqrt{\alpha_x^2 + \alpha_y^2 + \alpha_z^2} \tag{2.5}$$

where α_x, α_y and α_z represent the messured acceleration of x, y and z axes respectively. Then applying a high-pass Butterworth filter to filter low frequency drift. The cut off frequency is designed as 0.007 Hz in this testing. Also, high frequency noise must be filtered. A low-pass Butterworth filter with 2.05 Hz cut off frequency is applied in this testing. However, both the high-pass and low-pass filters could not measure the accurate data. A threshold stationary detection is applied to correct the acceleration data. When the IMU sensor moving, the stationary value is equal to zero. And, when it stopping, the stationary value is equal to one. The threshold stationary value α_s is designed as 0.09.

$$\alpha_s = \begin{cases} 1, & (-0.09 < \alpha_m < 0.09) \\ 0. & (\alpha_m < -0.09 \ \& \ 0.09 < \alpha_m) \end{cases} \tag{2.6}$$

Fig. 2-2 shows the raw acceleration data and stationary motion identification of IMU 1. Fig. 2-2 (a) shows the 3-D raw angular velocity data from the gyroscope of IMU 1, and Fig. 2-2 (c) shows the details of stationary motion identification in Fig. 2-2 (b). When the human walking, her or his chest part

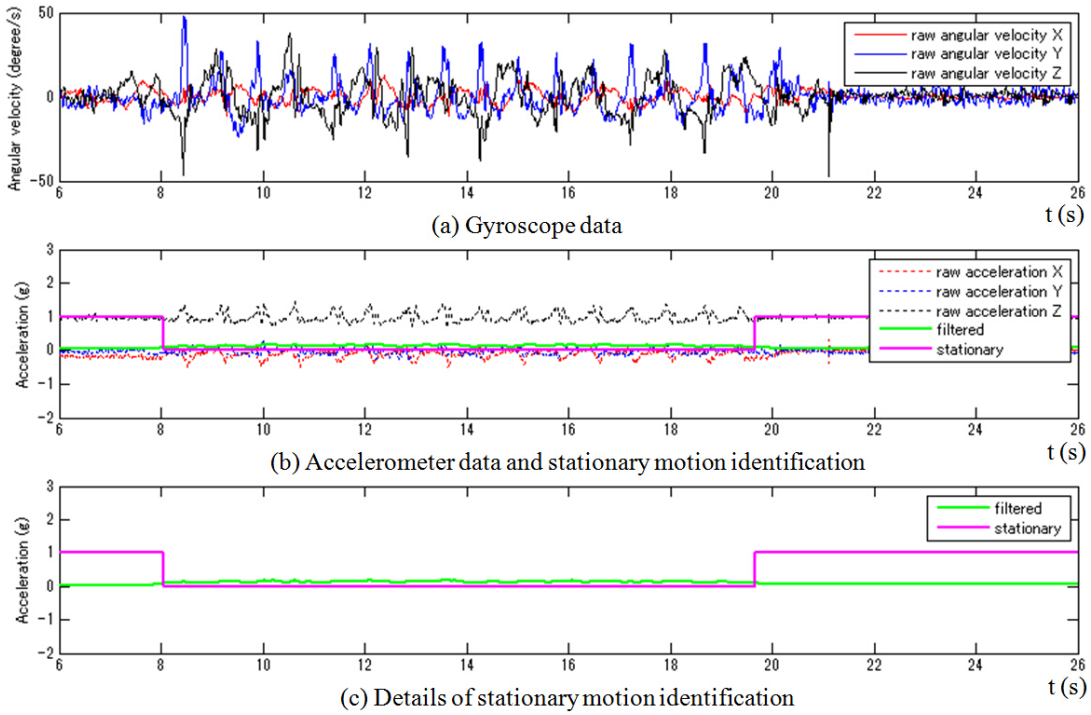

Fig. 2-2: Raw acceleration data and stationary motion identification of IMU 1.

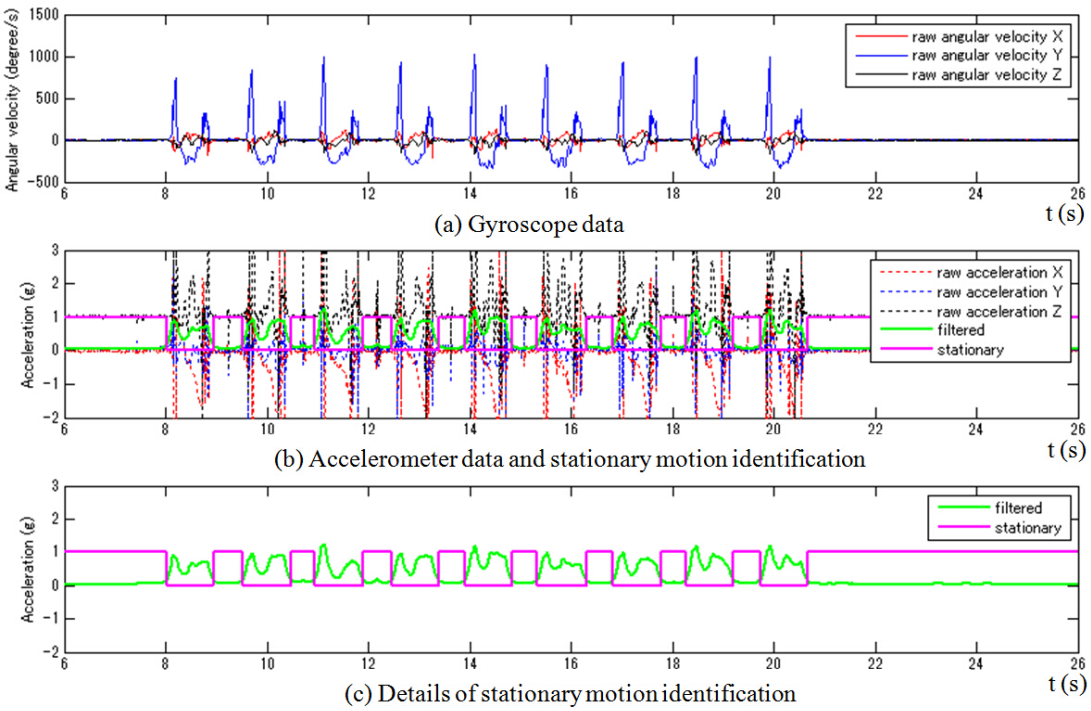

Fig. 2-3: Raw acceleration data and stationary motion identification of IMU 2.

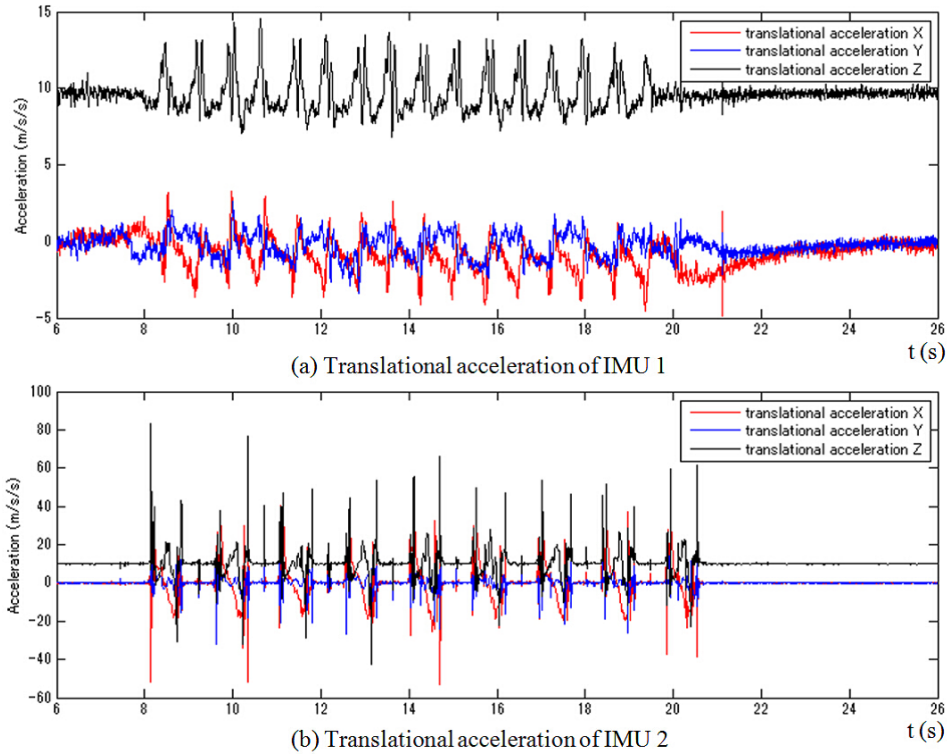

(a) Translational acceleration of IMU 1

(b) Translational acceleration of IMU 2

Fig. 2-4: Translational acceleration data.

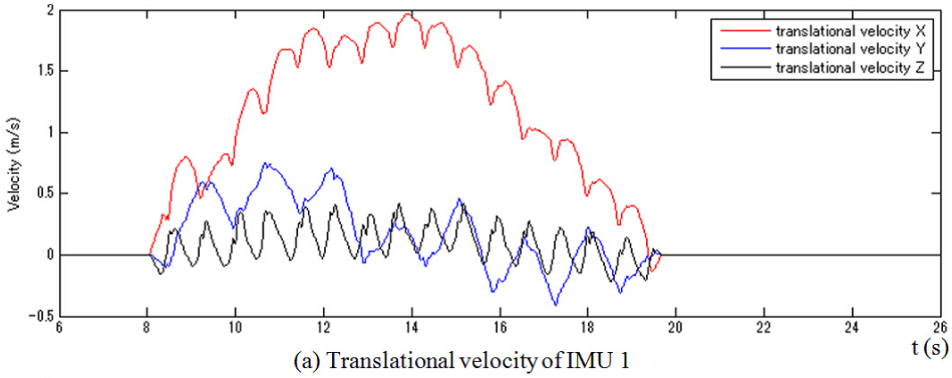

(a) Translational velocity of IMU 1

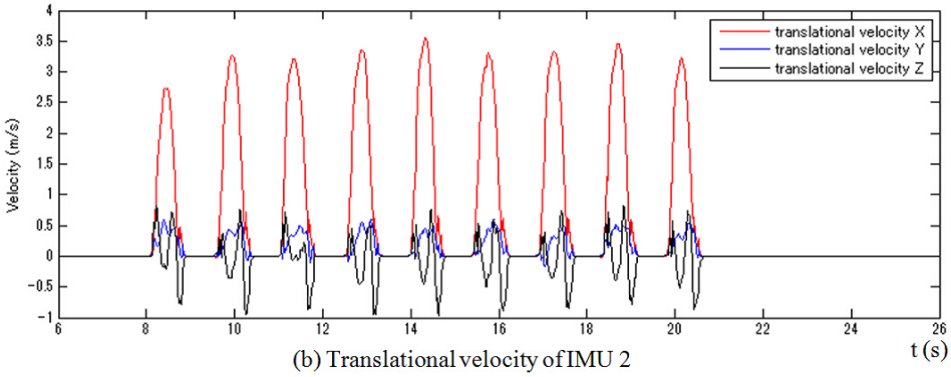

(b) Translational velocity of IMU 2

Fig. 2-5: Translational velocity (by once integration of acceleration and correction).

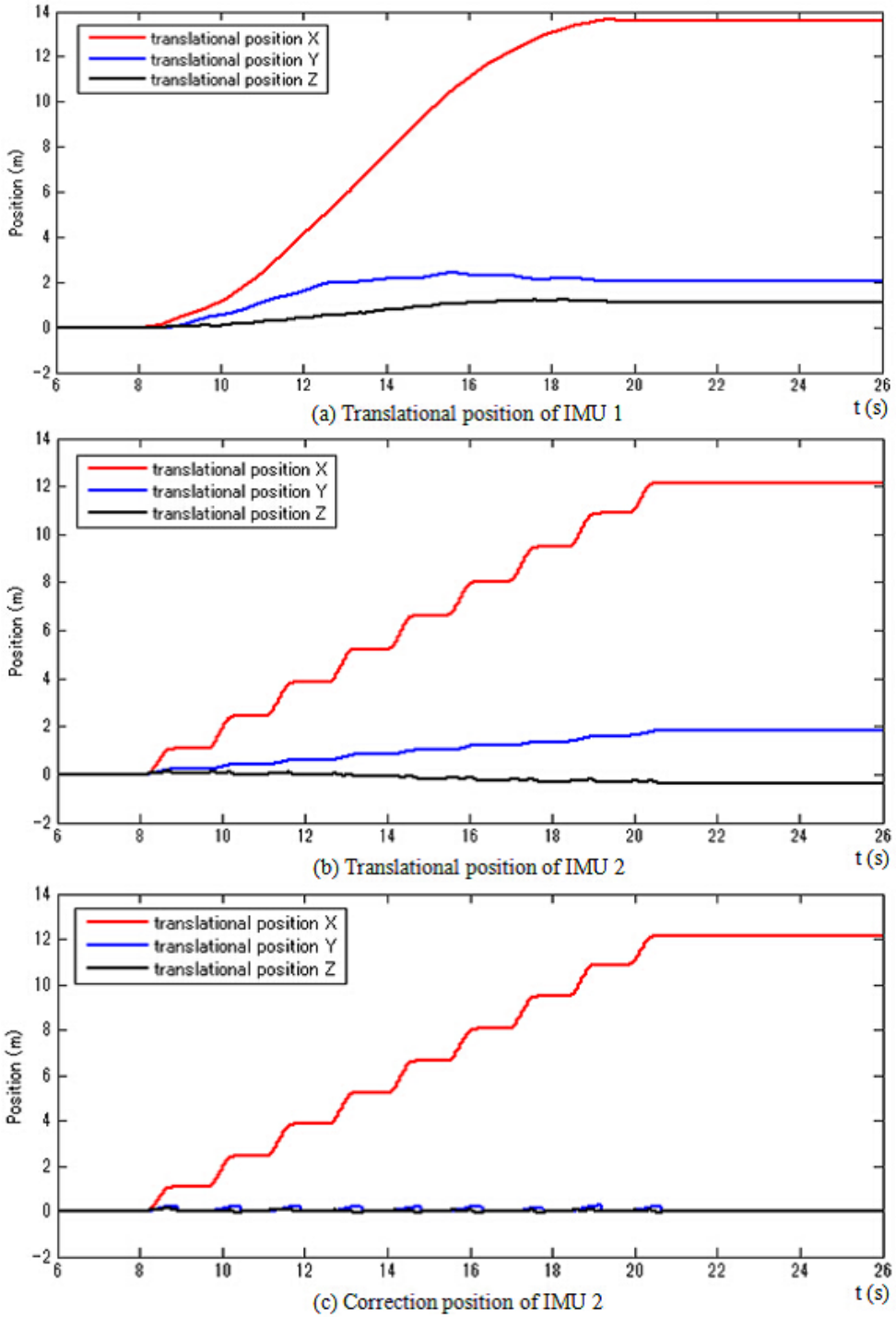

Fig. 2-6: Translational position (by once integration of velocity and correction).

keeps moving without stopping. Therefore, the stationary value is always equal to zero when the human walking. Due to there is no chance to modify the measured data, it may lead to a large deviation for the human motion measurement data. Fig. 2-3 shows the raw acceleration data and stationary motion identification of IMU 2. Fig. 2-3 (a) shows the 3-D raw angular velocity data, it is much bigger than IMU 1 when the foot swaying. Fig. 2-3 (c) shows the details of stationary motion identification in Fig. 2-3 (b). When the human walking, her or his feet keep swaying and stopping moving circularly. Thus the stationary value is changing when the human walking. It is easy to correct the drift and error of the measurement data timely.

By applying the quaternion, the human body accelerations can be rotated to earth world frame. For the unit quaternion (a, b, c, d) the corresponding rotation matrix R is defined as follows,

$$\boldsymbol{R} = \begin{bmatrix} 2a^2 + 2b^2 - 1 & 2(bc + ad) & 2(bd - ac) \\ 2(bc - ad) & 2a^2 + 2c^2 - 1 & 2(cd + ab) \\ 2(bd + ac) & 2(cd - ab) & 2a^2 + 2d^2 - 1 \end{bmatrix} \tag{2.7}$$

Then the 3-D translational acceleration $[\alpha_x^w, \alpha_y^w, \alpha_z^w]^T$ can be represented by,

$$\begin{bmatrix} \alpha_x^w \\ \alpha_y^w \\ \alpha_z^w \end{bmatrix} = \boldsymbol{R} \begin{bmatrix} \alpha_x \\ \alpha_y \\ \alpha_z \end{bmatrix} \tag{2.8}$$

Fig. 2-4 shows the translational acceleration data in earth world frame. Fig. 2-4 (a) shows the 3-D translational acceleration of IMU 1. And Fig. 2-4 (b) shows the 3-D translational acceleration of IMU 2. When the human walking, the acceleration of IMU 1 keeps small changing ($8s \sim 20.5s$), but the acceleration of IMU 2 keeps big changing. Fig. 2-5 shows the translational velocity by once integration of acceleration and correction. For IMU 2, if the threshold stationary value α_s is 1, force the velocity to be 0. Since there is no threshold stationary 1 during human walking period for IMU 1, the velocity cannot be corrected. Fig. 2-6 shows the translational position by once integration of velocity and correction. Fig. 2-6 (a) shows the translational position of IMU 1, the measurement error is a little big because of the drift and no correction. Fig. 2-6 (b) shows the translational position of IMU 2 only with velocity correction, the measurement error should be small theoretically. Fig. 2-6 (c) shows the translational position of IMU 2 with velocity and position corrections, the stationary position of Y and Z are forced to be 0 again according to the actual situation of the testing.

Fig. 2-7 shows the 3-D demonstration of IMU 1. Obviously, the drift of Y and Z are a little big. Also, the drift of X should be big. This means that the IMU fixed on chest part can not measure the human

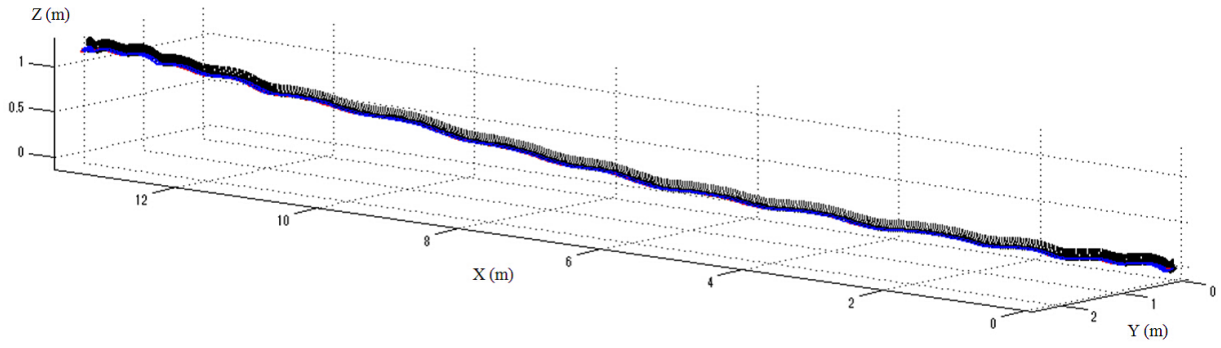

Fig. 2-7: Three dimensional demonstration of IMU 1.

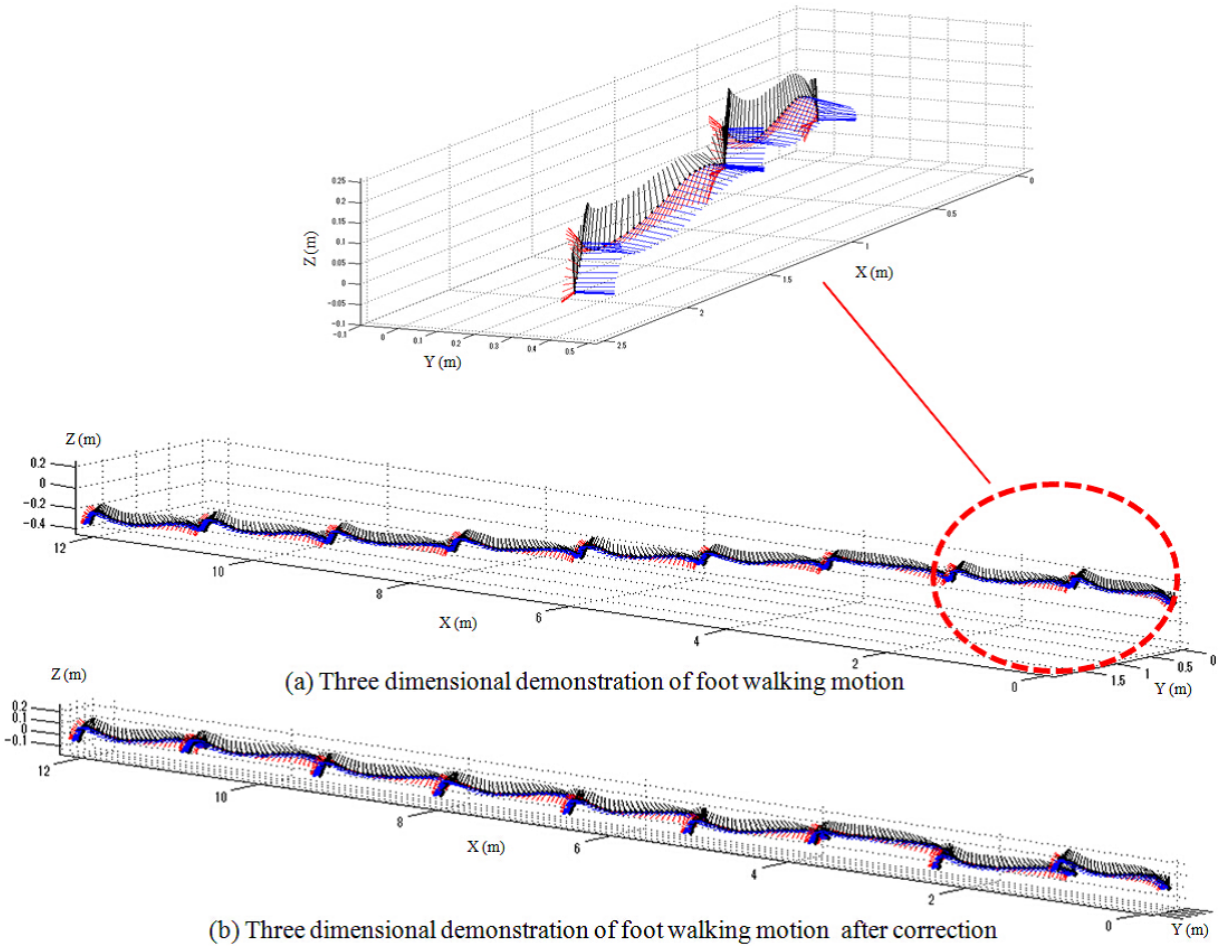

Fig. 2-8: Three dimensional demonstration of IMU 2.

Fig. 2-9: A photo of the testing (IMU 1 is fixed on chest and IMU 2 is fixed on foot).

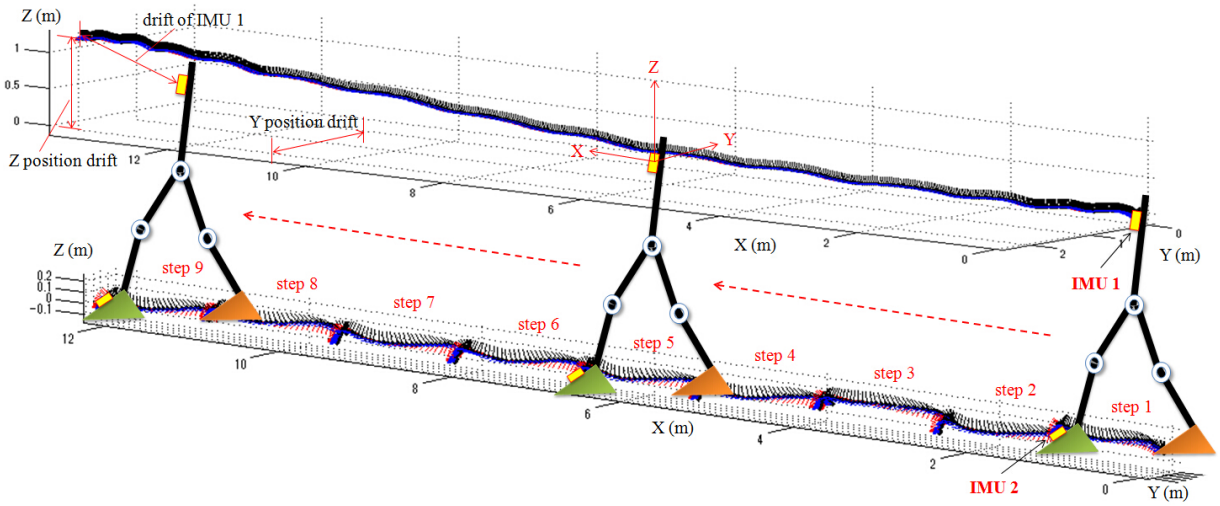

Fig. 2-10: Final integrated three dimensional demonstration of human straight walking.

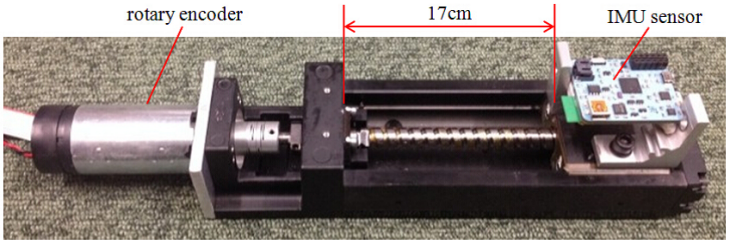

Fig. 2-11: IMU precision testing by a linear motor base.

walking motion accurately. But the human body posture can be measured well by the Euler angles. Fig. 2-8 shows the 3-D demonstration of IMU 2. Fig. 2-8 (a) shows the three dimensional demonstration without position correction (only velocity correction). Fig. 2-8 (b) shows the three dimensional demonstration with both velocity and position corrections. Obviously, the drift of Y and Z become very small at last. This means that the IMU fixed on foot can measure the human walking motion well.

Fig. 2-9 shows a photo of the testing by real human. IMU 1 is fixed on chest and IMU 2 is fixed on foot. The IMU sensors are small and easy to wear. And the data was sent through the Bluetooth module of IMU sensors. Fig. 2-10 shows the final integrated 3-D demonstration of human straight walking. By the calibration of integrated velocity value, the position measurement precision of IMU 1 is relatively large. But the posture measurement performance of IMU 1 (Euler angles) is good. By both of the calibration of integrated velocity and position value, the position measurement precision of IMU 2 is relatively small. Also the posture measurement performance of IMU 2 is good.

2.3 Measurement Precision

In the previous section, human walking motion was measured by two IMU sensors. The specification of sensors made by x-io Technologies are shown in Table 2.1. The data from the IMU sensors is provided in either the raw inertial/magnetic data and raw battery and thermometer data packets or the calibrated inertial/magnetic data, calibrated battery, thermometer data and quaternion data packets. The data output rate of these packets may be set to 1 Hz, 2 Hz, 4 Hz, 8 Hz, 16 Hz, 32 Hz, 64 Hz, 128 Hz, 256 Hz or 512 Hz. The output signals used in this dissertation are gyro angle velocity, acceleration and quaternion. Euler angles which can measure the human posture are calculated by quaternion. One IMU sensor was fixed on chest and the other one was fixed on foot. Their measurement performance and 3-D demonstration were introduced too. However, how is the accuracy of the IMU sensor measurement was not discussed. In this section, measurement precision of the utilized IMU sensor is studied. In theory, the output of an

Table 2.1: Main specification of the IMU sensor.

Name	Specification
Dimensions	33 × 42 × 10 mm
Weight	12 g
Triple axis 16-bit gyroscope	Selectable range up to ± 2000°/s
Triple axis 12-bit accelerometer	Selectable range up to ± 78.4 m^2/s
Triple axis 12-bit magnetometer	Selectable range up to ± 8.1 G
Data rates	Selectable rates up to 512 Hz
External power	3.6 V to 6.3 V
Bluetooth connectivity	Class 1, 100m range, SPP
Micro SD card connectivity	Supports FAT16/32 and SDHC

accelerometer can be integrated twice to obtain displacement information. But low-cost accelerometers are susceptible to drift errors. The position estimates based on double integration can diverge in a short time period lasting only a few seconds. Therefore, the velocity and position precision was studied by a linear motor base firstly. Fig. 2-11 shows the equipment of this testing. The IMU sensor was moved on the base and the encoder got a reliable measurement. Fig. 2-12 indicates that the errors is existing and there is an impact in the end of this testing. However, human walking step cycle measurement does not need a high precision. That is because all of the measurement data of IMU sensor is set to zero. Without the impact motion, the position accuracy can be achieved to about 95%. Thus the reliability of velocity and orientation measurement can be guaranteed. But the drift correction is essential for tracking position using low-cost accelerometers. In the previous section, a drift correction method is described as well. The drift of IMU sensors is not white noise. Therefore, some other methods (like compliance control) will be introduced to reduce this drift in the real approaches.

2.4 Concluding Remarks

Human motion measurement is an interesting and challenging issue. It plays an important role in the field of the man-machine coordinated control. This dissertation attempts to use IMU sensors to measure human walking and posture motions, and then propose some real-time systems to help the elderly walk or move well. As explained in this chapter human feet walking motion and human posture motion can be measured well by low-cost IMU sensors. The measurement precision is not very high but it is good enough for human walking step cycle measurement by some calibration methods. Also, not only human

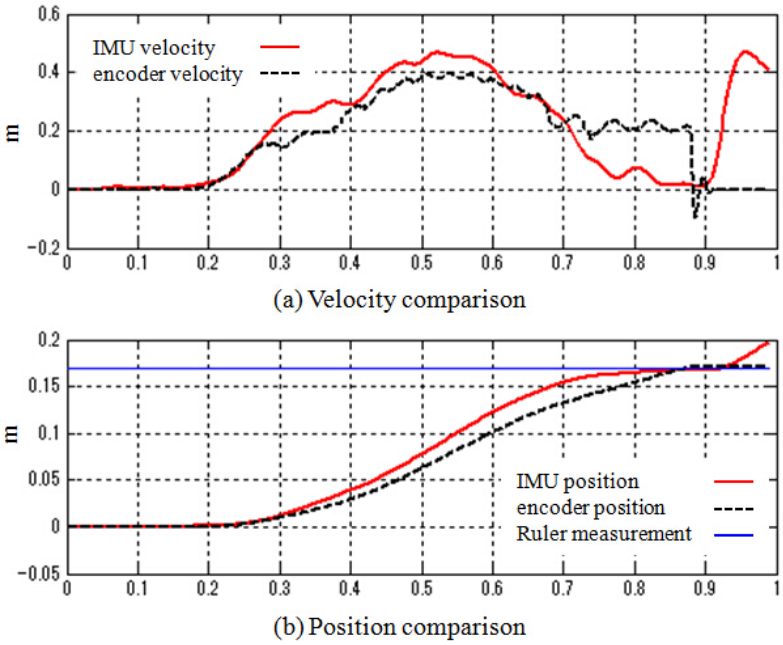

(a) Velocity comparison

(b) Position comparison

Fig. 2-12: Results of the IMU sensor precision testing.

posture but also robot posture can be measured by them. In later chapters their applications in proposed real-time systems will be explained in more details.

Chapter 3

Observers

Since actuators (motors) are indispensable in robot systems, knowledge about robust system is introduced in this chapter before discussing about topics in the dissertation. For a controllable system, like a DC motor, disturbance and external force always affect the velocity or position tracking performance and stability. It is necessary to design a dedicated disturbance suppression controller to achieve high performance systems. Fig. 5-8 shows a general feedback system with disturbance and observer. In the following sections, disturbance observer and other two observers that based on the theory of disturbance observer will be introduced. These observers will be utilized in later chapters.

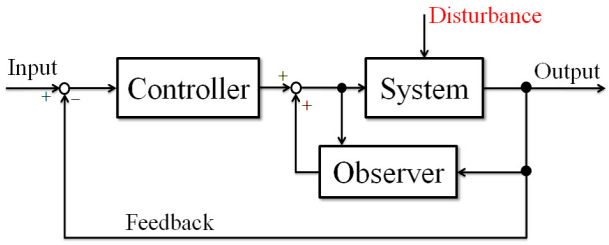

Fig. 3-1: An elementary feedback system with disturbance and observer.

3.1 Dynamics Based DC Motor Control

In industrial applications, DC motors are widely used as the actuators. DC motors are driven from electromagnetic effect with permanent magnet and coil. Effect of rotation performance of them is complicated. It relates to controller design and external disturbance. Especially external disturbance not only

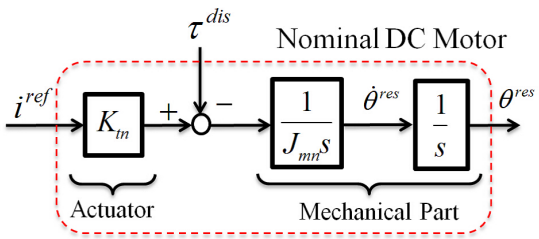

Fig. 3-2: Nominal dynamics model of DC Motors.

has complex uncertain causes, but also effects the robustness. From the motor datasheet, the actuated effect is modeled by a torque constant K_t.

$$K_t i^{ref} = J_m \ddot{\theta}^{res} + \tau^l \tag{3.1}$$

$$\tau^l = \tau^{int} + \tau^{ext} + \tau^{fri} \tag{3.2}$$

where τ^l is load torque, it includes motor internal interfering torque τ^{int}, external reaction torque τ^{ext} and friction force τ^{fri}. i^{ref} indicates the reference current. In real applications, the torque constant K_t consists of complicated matters. Also, the motor inertia constant J_m contains uncertain variation. Although they are modeled as constants, they contain perturbations,

$$J_m = J_{mn} + \Delta J_m \tag{3.3}$$

$$K_t = K_{tn} + \Delta K_t \tag{3.4}$$

where J_{mn} is nominal inertia constant, K_{tn} is nominal torque constant. ΔJ_m and ΔK_t are inertia perturbation and torque perturbation respectively. Assuming the motor is placed in the vertical plane, the gravity changing of load is negligible. Consider about the inertia uncertain variation and torque perturbation and define the disturbance torque as,

$$\tau^{dis} = \tau^{int} + \tau^{ext} + \tau^{fri} + \Delta J_m \ddot{\theta}^{res} - \Delta K_t i^{ref} \tag{3.5}$$

Based on the above eq. (3.1) to eq. (3.5), the disturbance torque can be calculated as,

$$\tau^{dis} = K_{tn} i^{ref} - J_{mn} \ddot{\theta}^{res} \tag{3.6}$$

Fig. 3-2 gives a block diagram of nominal dynamics model of DC motors. For a feedback control system, both rotating velocity $\dot{\theta}^{res}$ and position θ^{res} can be used as feedback terms. The position is usually measured by encoders and the velocity is usually calculated by position. In order to achieve

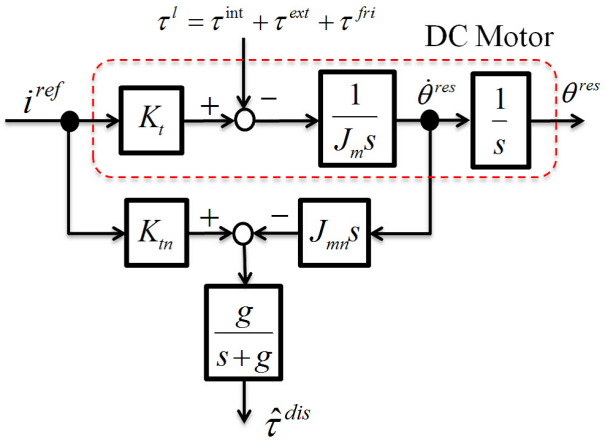

Fig. 3-3: Disturbance calculation with a first order low pass filter.

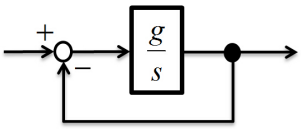

Fig. 3-4: Equivalent block diagram of low pass filter.

precise motor control, disturbance torque τ^{dis} should be compensated well. Generally, DC motor control is nothing more than generating the appropriate reference current i^{ref} for the desired position, velocity, acceleration, or torque. But because of the disturbance torque, a perfect i^{ref} is not easy to be decided without any disturbance compensation. Thus the next section will introduce an observer method to compensate this disturbance torque.

3.2 Disturbance Observer

Today, disturbance observer (DOB) is widely used in motor control to achieve high performance robust systems. It was proposed by Prof. Kouhei Ohnishi in the early 1980s [90] [91] [92]. After that many researches and papers are applied it and got many good results. In DOB, disturbance torque τ^{dis} is calculated by reference current i^{ref} and acceleration response $\ddot{\theta}^{res}$. However, the acceleration is calculated by twice digital differential calculation of position response θ^{res} measured by encoders. Because of the differential calculation error and encoder measurement noise, $\ddot{\theta}^{res}$ must has high frequency noise. If this high frequency noise is not be filtered, the performance and robustness of motor systems are affected. Therefore, a first order low pass filter is applied to filter the noise. Fig. 3-3 describes eq. (3.6) with a first

order low pass filter in the DC motor system. Denote the cutoff frequency is g, thus,

$$\hat{\tau}^{dis} = \frac{g}{s+g}\tau^{dis} \tag{3.7}$$

Fig. 3-4 shows the equivalent block diagram of the low pass filter. According to Fig. 3-3 and Fig. 3-4, the observed disturbance torque τ^{dis} can be obtained by a simple integretion calculation. It means that this method can be easily realized in the practical application of digital systems. Change the nominal inverse model of DC motors $J_{mn}s$ like,

$$J_{mn}s = \frac{J_{mn}s}{s}(s+g-g) = gJ_{mn}\frac{s+g}{g} - gJ_{mn} \tag{3.8}$$

Substitute eq. (3.8) and eq. (3.6) in eq. (3.7), then,

$$\begin{aligned}\frac{g}{s+g}(K_{tn}i^{ref} - J_{mn}\ddot{\theta}^{res}) &= \frac{g}{s+g}[K_{tn}i^{ref} - (gJ_{mn}\frac{s+g}{g} - gJ_{mn})\dot{\theta}^{res}] \\ &= \frac{g}{s+g}K_{tn}i^{ref} + \frac{g}{s+g}gJ_{mn}\dot{\theta}^{res} - gJ_{mn}\dot{\theta}^{res}\end{aligned} \tag{3.9}$$

Fig. 3-5 describes eq. (3.9) by a block diagram. Also, this is the normal structure of DOB.

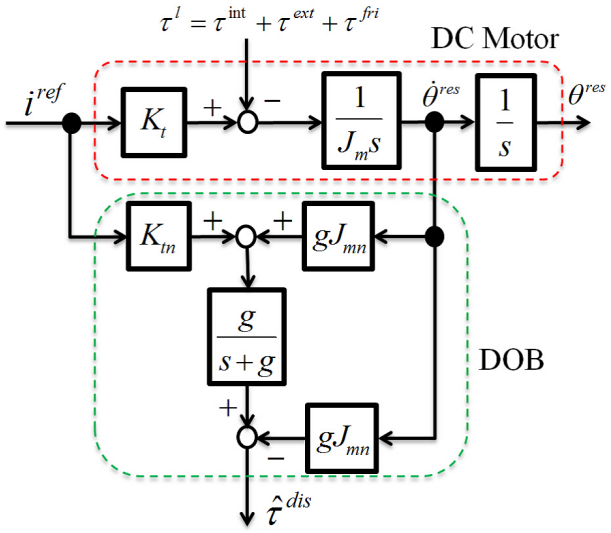

Fig. 3-5: Block diagram of DOB.

After obtaining the observed disturbance torque $\hat{\tau}^{dis}$, the disturbance can be compensated by a feedback $\frac{\hat{\tau}^{dis}}{K_{tn}}$. Fig. 3-6 describes the final block diagram of DOB control. It can reduce the disturbance and achieve high performance robust systems. Fig. 3-7 shows the equivalent block diagram of Fig. 3-6. It also describes the visualized effection of DOB. In this equivalent block diagram, disturbance is diminished by low pass filter forward term. If the system bandwidth is infinite ($g = \infty$), complete robust

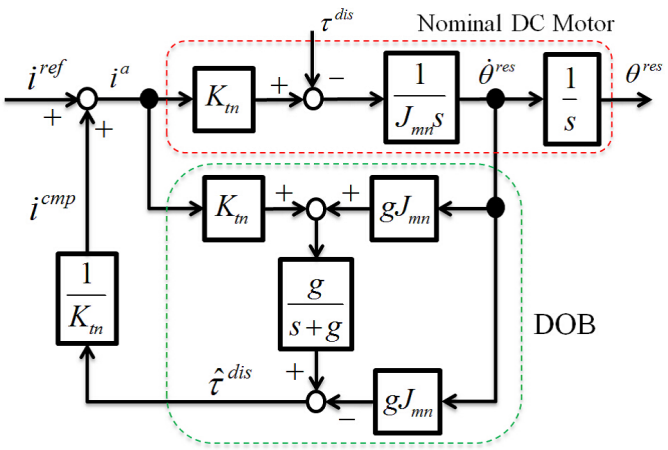

Fig. 3-6: Reduce disturbance via current feedback compensation.

control system is achieved by DOB compensation method. Fig. 3-8 explains the visualized effection of DOB with $g = \infty$.

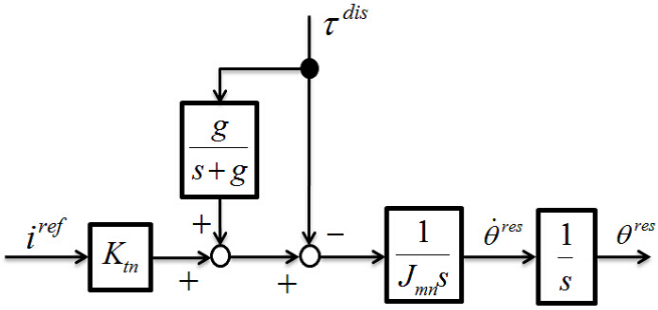

Fig. 3-7: Visualization of effect of DOB.

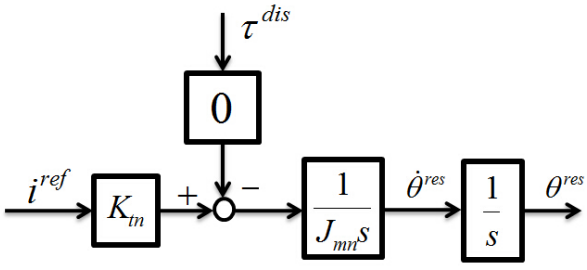

Fig. 3-8: Equivalent block diagram of Fig. 3-7.

In previous contents, a first order low pass filter but not other filters was utilized to reduce the high frequency noise in DOB. Also, the problem of time delay of the low pass filter was not discussed. For a feedback control system, time delay is an important issue for its stability. Therefore, the effect of differentiation and the low pass filter in DOB will be discussed from the next paragraph.

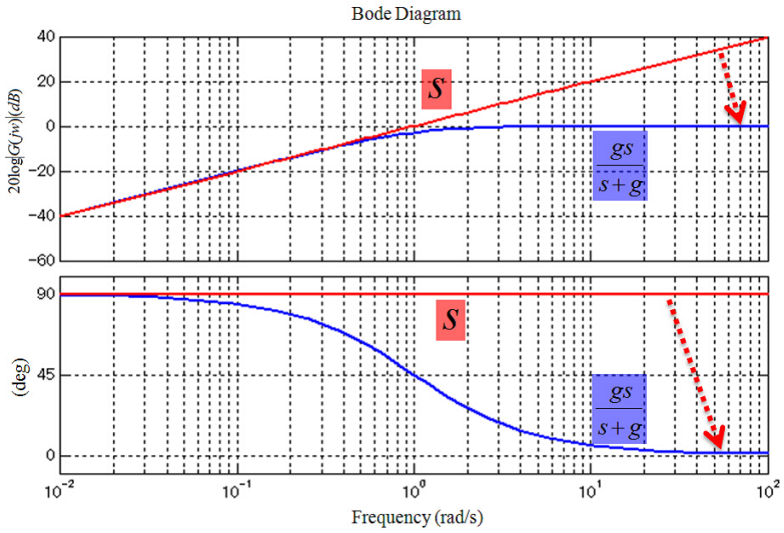

Fig. 3-9: The gain in high frequency is decreased by pseudo differentiation.

In real applications of DOB, acceleration response is required for estimating the disturbance torque τ^{dis}. The term $J_{mn}s$ is once differentiation in Fig. 3-3. Fig. 3-9 shows the bode diagram of pure s and pseudo differentiation $\frac{gs}{s+g}$ respectively. From this bode diagram, the higher feedback noise is, the bigger gain will be. In order to achieve the lower gain in high frequency, the pseudo differentiation $\frac{gs}{s+g}$ is applied in DOB. Fig. 3-10 shows the detailed analysis of DOB with pseudo differentiation. There are two feedback loop in DOB.

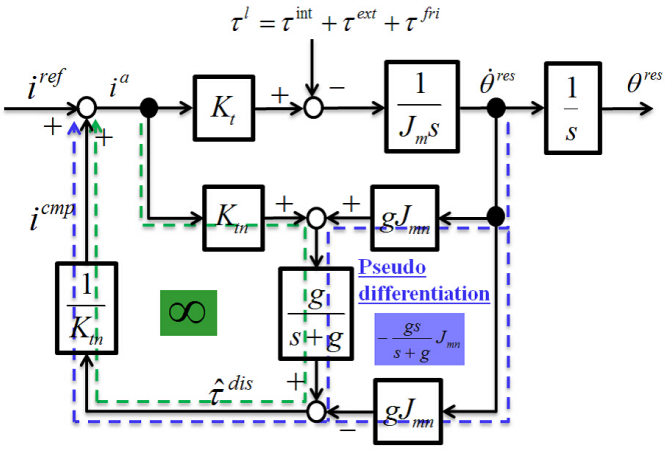

Fig. 3-10: Detailed analysis of DOB with pseudo differentiation.

If $g = \infty$, the low pass filter can be changed as (the green loop),

$$\frac{g}{s+g} \approx 1 \tag{3.10}$$

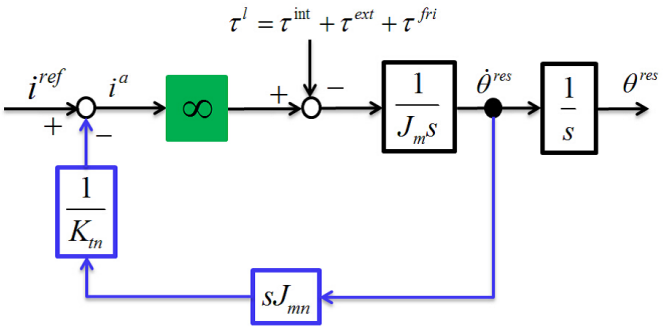

Fig. 3-11: Equivalent block diagram of Fig. 3-10.

In the blue loop, feedback can be obtained by pseudo differentiation as,

$$\frac{g}{s+g} g J_{mn} \dot{\theta}^{res} - g J_{mn} \dot{\theta}^{res} = -\frac{gs}{s+g} J_{mn} \dot{\theta}^{res} \approx -s J_{mn} \dot{\theta}^{res} \tag{3.11}$$

Fig. 3-11 shows a equivalent block diagram of Fig. 3-10. The green loop is equivalent to an infinite gain and the blue loop is equivalent to an acceleration feedback. This equivalent block diagram makes the function of DOB like an operational amplifier. Fig. 3-12 shows the visualization of function of DOB.

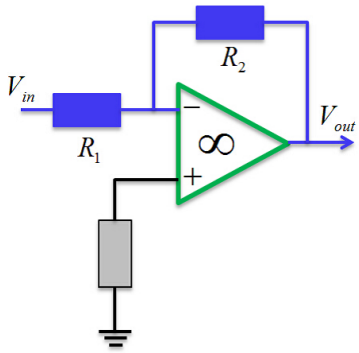

Fig. 3-12: Visualization of function of DOB (as an operational amplifier).

In the operational amplifier,

$$\frac{V_{in}}{R_1} + \frac{V_{out}}{R_2} = 0 \tag{3.12}$$

Denote $\frac{V_{in}}{R_1}$ as i^{ref}, $\frac{V_{out}}{R_2}$ as $\frac{-J_{mn}\ddot{\theta}^{res}}{K_{tn}}$, thus,

$$i^{ref} - \frac{J_{mn}\ddot{\theta}^{res}}{K_{tn}} = 0 \tag{3.13}$$

Then the relationship of input torque and output torque can be shown as,

$$K_{tn} i^{ref} = J_{mn} \ddot{\theta}^{res} \tag{3.14}$$

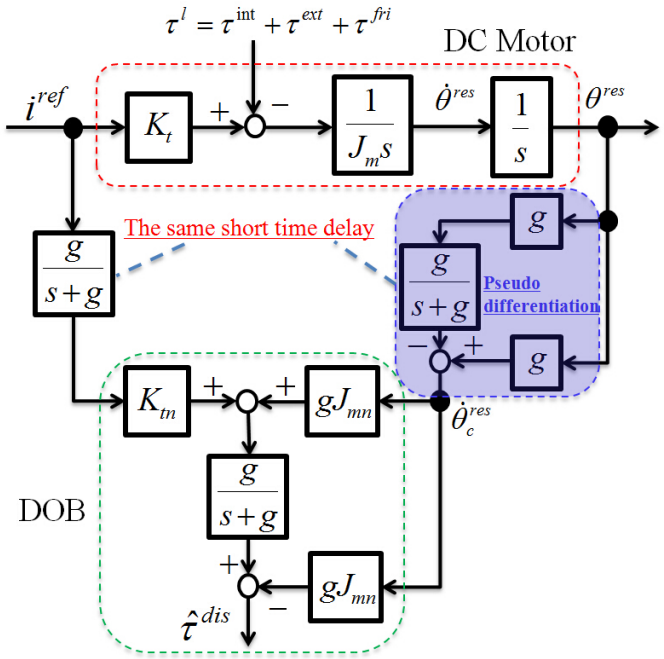

Fig. 3-13: DOB block diagram with position feedback.

This means that the disturbance torque has been compensated completely by DOB. It also explains that why the gain of disturbance torque can be zero in Fig. 3-8. However, all above contents about DOB are based on velocity feedback. In real applications, velocity can not be directly measured by encoders. Encoders can only measure the position response. Since the low pass filter has a time delay problem, the velocity response can not be calculated from position response without time delay even applying pseudo differentiation. In order to keep the same time delay for both input torque and output torque, a low pass filter should be added in the input torque calculation loop. Fig. 3-13 shows a new DOB block diagram with position feedback. By this method, the effect of differentiation and the low pass filter in DOB can be reduced completely.

By using DOB, disturbance torque has been compensated. After that, a basic DC motor position controller with DOB is shown in Fig. 3-14. In this controller, a PD and acceleration command are included in the reference,

$$\ddot{\theta}^{ref} = \ddot{\theta}^{cmd} + K_v(\dot{\theta}^{cmd} - \dot{\theta}^{res}) + K_p(\theta^{cmd} - \theta^{res}) \tag{3.15}$$

Assuming $\ddot{\theta}^{res}$ is equal to $\ddot{\theta}^{ref}$, thus,

$$(s^2 + K_v s + K_p)(\theta^{cmd} - \theta^{res}) = 0 \tag{3.16}$$

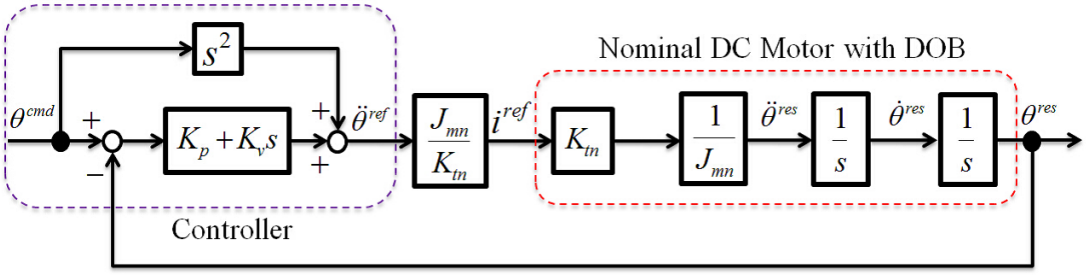

Fig. 3-14: A basic DC motor position controller with DOB (based on acceleration input).

When $(\theta^{cmd} - \theta^{res})$ is toward to zero,

$$\frac{\ddot{\theta}^{res}}{\ddot{\theta}^{cmd}} = \frac{\dot{\theta}^{res}}{\dot{\theta}^{cmd}} = \frac{\theta^{res}}{\theta^{cmd}} = 1 \tag{3.17}$$

It achieves the purpose of acceleration tracking, velocity tracking and position tracking at the same time. This motor position controller will be utilized in the approaches of this dissertation in later chapters. Based on this method of DOB, other two observers are introduced in following sections.

3.3 Reaction Torque Observer

The theory of DOB is not limited to control a DC motor, in this section, it is extended to robustly control a manipulator by force but without any force sensor. Based on DOB, Prof. Toshiyuki Murakami proposed reaction torque observer (RTOB)/ reaction force observer (RFOB) in the early 1990s [93] [94]. In multi-degree of freedom manipulator systems, torque/force sensorless control is an important issue. Because force sensors increase the cost and reduce the durability of the systems. RTOB/RFOB can solve these problems well. For simplicity, a manipulator with two links fixed horizontally is applied to explain RTOB. Fig. 3-15 shows the model of the manipulator.

Assuming mass points are at the end of each link, and they are m_1, m_2, from the end to origin, l_1, l_2 are the length of link 1 and link 2, respectively. The relative rotation angle are θ_1 and θ_2. x, y is the end position of the manipulator, therefore,

$$x = l_1 \sin\theta_1 + l_2 \sin(\theta_1 + \theta_2) \tag{3.18}$$

$$y = l_1 \cos\theta_1 + l_2 \cos(\theta_1 + \theta_2) \tag{3.19}$$

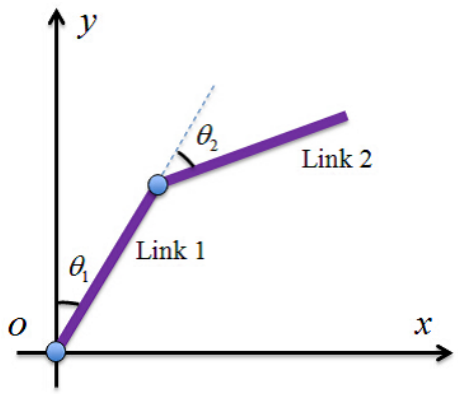

Fig. 3-15: A manipulator with two links.

Denote the vector position and angle as,

$$\boldsymbol{x} = [x, y]^T \tag{3.20}$$

$$\boldsymbol{\theta} = [\theta_1, \theta_2]^T \tag{3.21}$$

Then the velocity and acceleration can be described by Jacobian matrix,

$$\boldsymbol{x} = \boldsymbol{f}(\boldsymbol{\theta}) \tag{3.22}$$

$$\dot{\boldsymbol{x}} = \frac{\partial \boldsymbol{f}(\boldsymbol{\theta})}{\partial \boldsymbol{\theta}^T} = \boldsymbol{J}\dot{\boldsymbol{\theta}} \tag{3.23}$$

$$\ddot{\boldsymbol{x}} = \boldsymbol{J}\ddot{\boldsymbol{\theta}} + \dot{\boldsymbol{J}}\dot{\boldsymbol{\theta}} \approx \boldsymbol{J}\ddot{\boldsymbol{\theta}} \qquad (\dot{\boldsymbol{J}}\dot{\boldsymbol{\theta}} \approx 0) \tag{3.24}$$

$$\boldsymbol{J} = \begin{bmatrix} J_{11} & J_{12} \\ J_{21} & J_{22} \end{bmatrix} \tag{3.25}$$

where,

$$J_{11} = l_1 \cos\theta_1 + l_2 \cos(\theta_1 + \theta_2) \tag{3.26}$$

$$J_{12} = l_2 \cos(\theta_1 + \theta_2) \tag{3.27}$$

$$J_{21} = -l_1 \sin\theta_1 - l_2 \sin(\theta_1 + \theta_2) \tag{3.28}$$

$$J_{22} = -l_2 \sin(\theta_1 + \theta_2) \tag{3.29}$$

In the real application of manipulator, inverse kinematics is needed to control the end position. Assuming the manipulator moving motion is not very fast, therefore,

$$\dot{\boldsymbol{\theta}} = \boldsymbol{J}^{-1}\dot{\boldsymbol{x}} \tag{3.30}$$

$$\ddot{\boldsymbol{\theta}} = \boldsymbol{J}^{-1}(\ddot{\boldsymbol{x}} - \dot{\boldsymbol{J}}\dot{\boldsymbol{\theta}}) \approx \boldsymbol{J}^{-1}\ddot{\boldsymbol{x}} \ \ (\text{in case } \ddot{\boldsymbol{x}} \gg \dot{\boldsymbol{J}}\dot{\boldsymbol{\theta}}) \tag{3.31}$$

Assuming the mass of each link is on the end, the dynamics of the manipulator can be calculated by the Lagrange method. Denote K is the kinetic energy and P is the potential energy. Therefore L can be given by,

$$L = K - P \tag{3.32}$$

In Fig.3-15, the manipulator is fixed on a horizontal plane. Thus the gravity energy P is equal to zero. The total kinetic energy of the two links K is,

$$K = \frac{1}{2}m_1 l_1^2 \theta_1^2 + \frac{1}{2}m_2(\dot{x}^2 + \dot{y}^2) \tag{3.33}$$

Denote $\boldsymbol{\tau}$ is $[\tau_1 \ \ \tau_2]^T$ for the torque of link 1 and link 2. Then the manipulator dynamics can be calculated by the following method,

$$\boldsymbol{\tau} = \frac{d}{dt}\left(\frac{\partial L}{\partial \dot{\boldsymbol{\theta}}}\right) - \frac{\partial L}{\partial \boldsymbol{\theta}} \tag{3.34}$$

Calculate the eq. (3.34), the final dynamics of the manipulator is given by,

$$\boldsymbol{\tau} = \boldsymbol{M}(\boldsymbol{\theta})\ddot{\boldsymbol{\theta}} + \boldsymbol{H}(\boldsymbol{\theta}, \dot{\boldsymbol{\theta}}) \tag{3.35}$$

$$\boldsymbol{M} = \begin{bmatrix} M_{11} & M_{12} \\ M_{21} & M_{22} \end{bmatrix} \tag{3.36}$$

$$\boldsymbol{H} = [H_1 \ \ H_2]^T \tag{3.37}$$

where, $\boldsymbol{M}$ is the inertia matrix, $\boldsymbol{H}$ represents the Coriolis and centrifugal force. And the matrix terms are given by,

$$\begin{aligned} M_{11} &= l_1^2(m_1 + m_2) + l_2^2 m_2 + 2l_1 l_2 m_2 \cos\theta_2 \\ M_{12} &= l_2^2 m_2 + l_1 l_2 m_2 \cos\theta_2 \\ M_{21} &= l_2^2 m_2 + l_1 l_2 m_2 \cos\theta_2 \\ M_{22} &= l_2^2 m_2 \\ H_1 &= -l_1 l_2(2\dot{\theta}_1 + \dot{\theta}_2)\dot{\theta}_2 m_2 \sin\theta_2 \\ H_2 &= l_1 l_2 \dot{\theta}_1^2 m_2 \sin\theta_2 \end{aligned}$$

In section 3.2, DOB has been introduced. Based on the theory of DOB, the disturbance torque is given by,

$$\tau^{dis} = \tau^{int} + \tau^{ext} + \tau^{fri} + (M - M_n)\ddot{\theta}^{res} + (K_{tn} - K_t)i^{ref} \tag{3.38}$$

If the motion speed of the manipulator is not very high, the torque ripple is enough small to be ignored. Also, the changing of inertia is much smaller than the friction force τ^{fri}, thus it can be ignored. Then the reaction torque can be given by,

$$\tau^{ext} = \hat{\tau}^{dis} - (\tau^{int} + \tau^{fri}) \tag{3.39}$$

Therefore, the reaction torque can be calculated by the disturbance torque subtracting $(\tau^{int} + \tau^{fri})$ in real time. It means that the reaction torque can be calculated by this method. Fig. 3-16 shows the block diagram of RTOB.

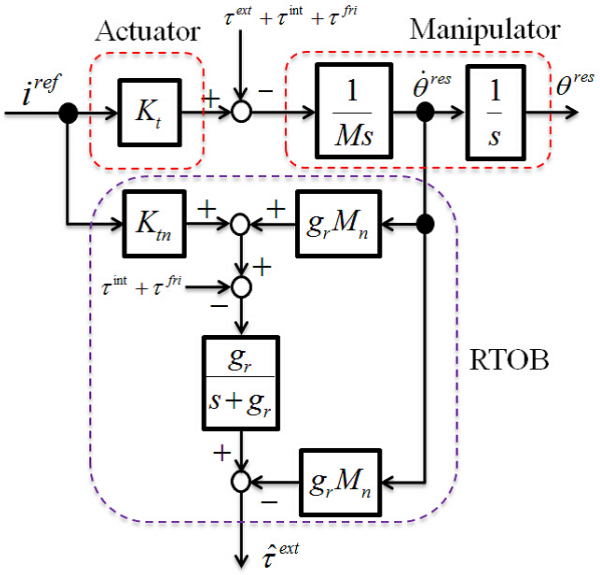

Fig. 3-16: Block diagram of RTOB.

The internal interfering torque τ^{int} and friction force τ^{fri} depend on the physical structure of motors. Both of them can be obtained by identity test before applying the actual motor. By using Jacobian matrix, reaction/external torque of each link is obtained by,

$$\boldsymbol{\tau}^{ext} = \boldsymbol{J}^T \boldsymbol{F}^{reac} \tag{3.40}$$

where $\boldsymbol{\tau}^{ext} = \hat{\boldsymbol{\tau}}^{ext}$ is reaction torque observed by RTOB of each joint, $\boldsymbol{F}_{reac}$ is the end force of the manipulator. From eq. (3.40), it can also be calculated by calculated reaction torque,

$$\boldsymbol{F}^{reac} = \left(\boldsymbol{J}^T\right)^{-1} \boldsymbol{\tau}^{ext} \tag{3.41}$$

By using the above equation and RTOB, sensorless force control for manipulator systems becomes possible.

3.4 Synthesized Camber Angle Disturbance Observer

The theory application of DOB/RTOB can go a step further to be applied in other systems. One-wheeled inverted pendulum system is an application example to be extended. In this section, a synthesized camber angle disturbance observer (SCOB) for the one-wheeled inverted pendulum system will be introduced. It synthesizes a wheel motor disturbance observer (WDOB) and a camber angle disturbance observer (CDOB). For the one-wheeled inverted pendulum system, camber angle disturbance observer is an important issue to be studied. Fig. 3-17 shows the model of the inverted pendulum system. For simplicity, only two dimensions is introduced to explain SCOB. Table 3.1 shows parameters of the one-wheeled inverted pendulum system.

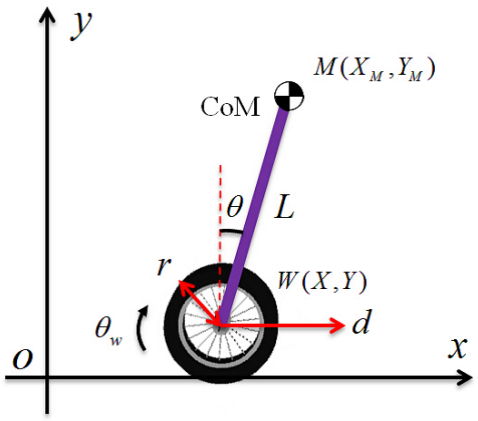

Fig. 3-17: One-wheeled inverted pendulum system.

Assuming there is no slipping motion for the wheel, the kinematics can be derived as,

$$r\dot{\theta}_w = \dot{d} \tag{3.42}$$

The vectors of work space and jiont space are given by eq. (3.43) and eq. (3.44) respectively.

$$\boldsymbol{X} = \begin{bmatrix} \theta & d \end{bmatrix}^T \tag{3.43}$$

$$\boldsymbol{\theta} = \begin{bmatrix} \theta & \theta_w \end{bmatrix}^T \tag{3.44}$$

From eq. (3.42), the kinematics is given by,

$$\begin{bmatrix} \dot{\theta} \\ \dot{d} \end{bmatrix} = \begin{bmatrix} 1 & 0 \\ 0 & r \end{bmatrix} \begin{bmatrix} \dot{\theta} \\ \dot{\theta}_w \end{bmatrix} = \boldsymbol{J}_{aco}\dot{\boldsymbol{\theta}} \tag{3.45}$$

Table 3.1: One-wheeled inverted pendulum system's parameters

Variables	Explanation
W	Reference point for controlling (wheel axle centre)
d	Moving distance
M	Center of mass (CoM) of the inverted pendulum
r	Wheel radius
θ	Camber angle
θ_w	Wheel rotation angle
X, Y	Real world coordinates for the wheel
X_M, Y_M	Real world coordinates for CoM
m_p	Inverted pendulum mass
m_w	Wheel mass
L	Inverted pendulum length for CoM
J_w	Wheel inertia moment

The inverse kinematics is given by,

$$\begin{bmatrix} \dot{\theta} \\ \dot{\theta_w} \end{bmatrix} = \begin{bmatrix} 1 & 0 \\ 0 & \frac{1}{r} \end{bmatrix} \begin{bmatrix} \dot{\theta} \\ \dot{d} \end{bmatrix} = \boldsymbol{J}_{aco}^{-1} \dot{\boldsymbol{X}} \tag{3.46}$$

The dynamics can be calculated by the Lagrange method. Denote K is the kinetic energy and P is the potential energy. The torque term can be derived by Lagrangian L,

$$\tau_i = \frac{d}{dt}\left(\frac{\partial L}{\partial \dot{\theta}_i}\right) - \frac{\partial L}{\partial \theta_i} \tag{3.47}$$

where i is the number of joints. In this one-wheeled inverted pendulum system, the total number of joints is 2. The reference point for controlling (wheel axle centre) W and the inverted pendulum CoM vectors are given by,

$$\boldsymbol{X}_W = \begin{bmatrix} d & r \end{bmatrix}^T \tag{3.48}$$

$$\boldsymbol{X}_M = \begin{bmatrix} d + L\sin\theta & r + L\cos\theta \end{bmatrix}^T \tag{3.49}$$

From the time derivation of eq. (3.48) and eq. (3.49),

$$\dot{\boldsymbol{X}}_W = \begin{bmatrix} \dot{d} & 0 \end{bmatrix}^T \tag{3.50}$$

$$\dot{\boldsymbol{X}}_M = \begin{bmatrix} \dot{d} + L\dot{\theta}\cos\theta \\ -L\dot{\theta}\sin\theta \end{bmatrix} \tag{3.51}$$

The total kinetic energy T includes wheel moving energy T_1, inverted pendulum CoM moving energy T_2 and wheel rotation energy T_3.

$$\begin{aligned} T_1 &= \frac{1}{2} m_w \dot{\boldsymbol{X}}_W^T \dot{\boldsymbol{X}}_W \\ &= \frac{1}{2} m_w \dot{\theta_w}^2 r^2 \qquad (3.52) \\ T_2 &= \frac{1}{2} m_p \dot{\boldsymbol{X}}_M^T \dot{\boldsymbol{X}}_M \\ &= \frac{1}{2} m_p (\dot{\theta_w}^2 r^2 + L^2 \dot{\theta}^2 + 2\dot{\theta_w} r L \dot{\theta} \cos\theta) \qquad (3.53) \\ T_3 &= \frac{1}{2} J_w \dot{\theta_w}^2 \qquad (3.54) \end{aligned}$$

Since the wheel height r is a constant, the gravity energy for the wheel U_1 is equal to zero. The gravity energy of the inverted pendulum CoM is given by,

$$U_2 = m_p g L \cos\theta \qquad (3.55)$$

Therefore, the Lagrangian L can be given by,

$$L = \frac{1}{2} m_w \dot{\theta_w}^2 r^2 + \frac{1}{2} m_p (\dot{\theta_w}^2 r^2 + L^2 \dot{\theta}^2 + 2\dot{\theta_w} r L \dot{\theta} \cos\theta) + \frac{1}{2} J_w \dot{\theta_w}^2 - m_p g L \cos\theta \qquad (3.56)$$

Applying eq. (3.47), the dynamics of the one-wheeled inverted pendulum system is given by,

$$\boldsymbol{\tau} = \boldsymbol{M}(\boldsymbol{\theta})\ddot{\boldsymbol{\theta}} + \boldsymbol{H}(\boldsymbol{\theta}, \dot{\boldsymbol{\theta}}) + \boldsymbol{G}(\boldsymbol{\theta}) \qquad (3.57)$$

where,

$$\begin{aligned} \boldsymbol{M} &= \begin{bmatrix} M_{uu} & M_{ua} \\ M_{ua} & M_{aa} \end{bmatrix} \\ &= \begin{bmatrix} m_p L^2 & m_p L r \cos\theta \\ m_p L r \cos\theta & J_w + r^2(m_w + m_p) \end{bmatrix} \qquad (3.58) \\ \boldsymbol{M}_n &= \begin{bmatrix} M_{nuu} & M_{nua} \\ M_{nua} & M_{naa} \end{bmatrix} \\ &= \begin{bmatrix} m_p L^2 & m_p L r \\ m_p L r & J_w + r^2(m_w + m_p) \end{bmatrix} \qquad (3.59) \\ \boldsymbol{H} &= \begin{bmatrix} H_u \\ H_a \end{bmatrix} = \begin{bmatrix} 0 \\ -m_p L r \dot{\theta}^2 \sin\theta \end{bmatrix} \qquad (3.60) \\ \boldsymbol{G} &= \begin{bmatrix} G_u \\ 0 \end{bmatrix} = \begin{bmatrix} -m_p L g \sin\theta \\ 0 \end{bmatrix} \qquad (3.61) \end{aligned}$$

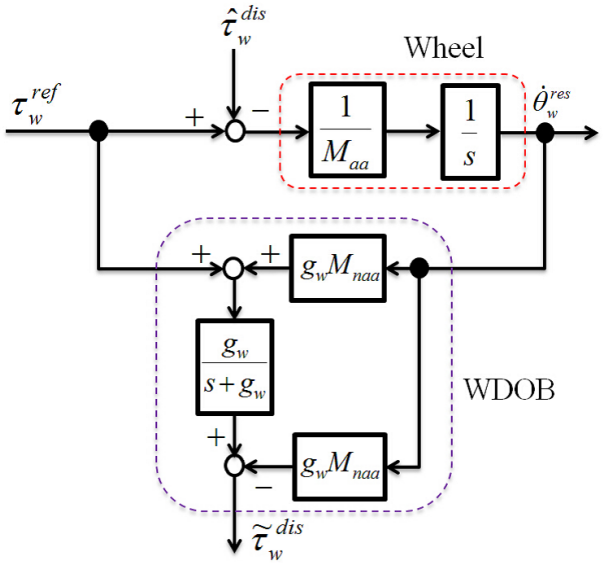

Fig. 3-18: Block diagram of WDOB.

$\boldsymbol{M}_n$ indicates the nominal inertia matrix, $\boldsymbol{\theta}$ and $\boldsymbol{\tau}$ are defined as,

$$\boldsymbol{\theta} = \begin{bmatrix} \theta \\ \theta_w \end{bmatrix} \tag{3.62}$$

$$\boldsymbol{\tau} = \begin{bmatrix} \tau_p \\ \tau_w \end{bmatrix} \tag{3.63}$$

Applying the dynamics of the one-wheeled inverted pendulum system, WDOB can be derived by,

$$\tau_w^{ref} = M_{ua}\ddot{\theta}^{res} + M_{aa}\ddot{\theta}_w^{res} + H_a + \tau_w^{dis} \tag{3.64}$$

where, τ_w^{dis} indicates the wheel motor disturbance. Assuming the modeling inertia error $(\boldsymbol{M} - \boldsymbol{M}_n)$ and the Coriolis and centrifugal force H_a are a part of disturbance, then a new disturbance $\hat{\tau}_w^{dis}$ can be given by,

$$M_{nua}\ddot{\theta}^{res} + M_{naa}\ddot{\theta}_w^{res} = \tau_w^{ref} - \hat{\tau}_w^{dis} \tag{3.65}$$

Assuming the camber angle inertia term $M_{nua}\ddot{\theta}^{res}$ is also a part of the disturbance, then another new disturbance $\hat{\tau'}_w^{dis}$ is given by,

$$M_{naa}\ddot{\theta}_w^{res} = \tau_w^{ref} - \hat{\tau'}_w^{dis} \tag{3.66}$$

From eq. (3.66), eq. (3.67) is obtained.

$$\hat{\tau'}_w^{dis} = \tau_w^{ref} - M_{naa}\ddot{\theta}_w^{res} \tag{3.67}$$

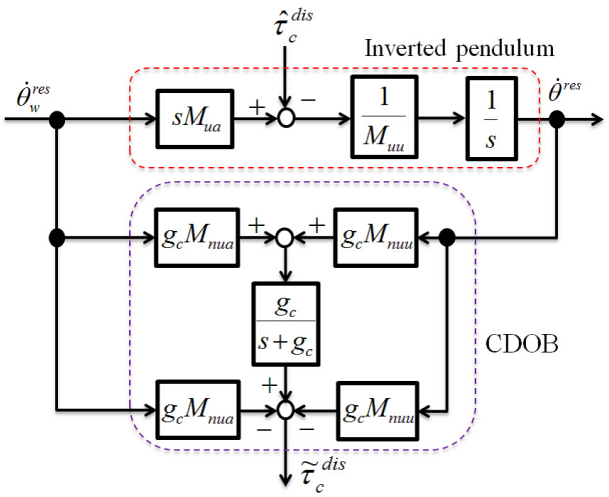

Fig. 3-19: Block diagram of CDOB.

Because the wheel rotation angle is measured by encoders, a low pass filter and the pseudo differentiation are utilized. Then the final wheel motor disturbance $\hat{\tau}_w^{dis}$ is calculated by,

$$\tilde{\tau}_w^{dis} = \frac{g_w}{s+g_w}\left(\tau_w^{ref} + g_w M_{naa}\dot{\theta}_w^{res}\right) - g_w M_{naa}\dot{\theta}_w^{res} \tag{3.68}$$

where g_w is the cut-off frequency of the low pass filter of WDOB. Fig. 3-18 shows the block diagram of WDOB.

For the camber angle of the inverted pendulum, it is measured by an IMU sensor. There are many disturbance factors that can affect the camber angle such as the modeling inertia error, the Coriolis and centrifugal force of the inverted pendulum. To achieve a good performance and robustness system, these disturbance factors should be compensated. CDOB is a method to compensate the camber angle disturbance. Applying eq. (3.57), the dynamics included camber angle disturbance is given by,

$$M_{uu}\ddot{\theta}^{res} + M_{ua}\ddot{\theta}_w^{res} + G_u + H_u + \tau_c^{dis} = 0 \tag{3.69}$$

where, τ_c^{dis} indicates the camber angle disturbance. Assuming the gravity term G_u, Coriolis and centrifugal force H_u, modeling inertia error $(\boldsymbol{M} - \boldsymbol{M}_n)$ are a part of the disturbance, a new disturbance $\hat{\tau}_c^{dis}$ can be given by,

$$M_{nuu}\ddot{\theta}^{res} + M_{nua}\ddot{\theta}_w^{res} = -\hat{\tau}_c^{dis} \tag{3.70}$$

From eq. (3.70), eq. (3.71) is obtained,

$$\hat{\tau}_c^{dis} = -\left(M_{nuu}\ddot{\theta}^{res} + M_{nua}\ddot{\theta}_w^{res}\right) \tag{3.71}$$

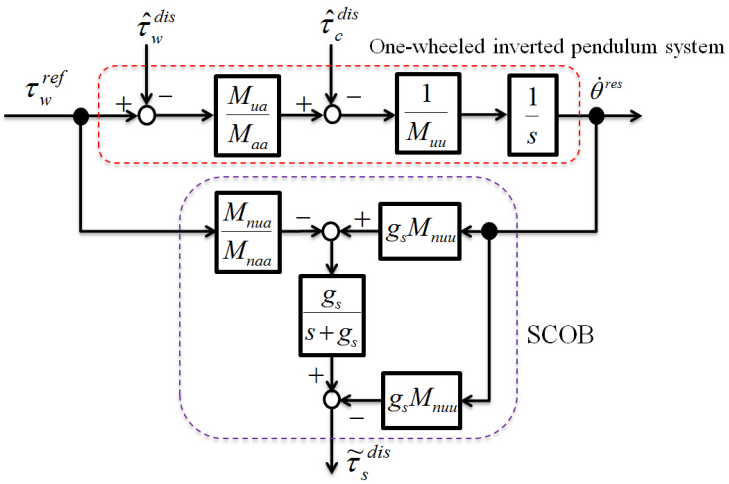

Fig. 3-20: Block diagram of SCOB.

In this system, the inverted pendulum is underactuated. In order to keep the balance, the controlled plant is the wheel. Because the camber angle response is measured by an IMU sensor, a low pass filter and the pseudo differentiation are utilized as well. Therefore, the final observed camber angle disturbance can be given by,

$$\tilde{\tau}_c^{dis} = \frac{g_c}{s+g_c}\left(M_{nuu}g_c\dot{\theta}^{res} + M_{nua}g_c\dot{\theta}_w^{res}\right) - \left(M_{nuu}g_c\dot{\theta}^{res} + M_{nua}g_c\dot{\theta}_w^{res}\right) \tag{3.72}$$

where, g_c is the cut-off frequency of the low pass filter of CDOB. Fig. 3-19 shows the block diagram of CDOB.

In the real application, WDOB and CDOB can be synthesized together as the SCOB. Applying eq. (3.57), the dynamics included wheel disturbance and camber angle disturbance are given by,

$$M_{uu}\ddot{\theta}^{res} + M_{ua}\ddot{\theta}_w^{res} + G_u + H_u + \tau_c^{dis} = 0 \tag{3.73}$$

$$M_{ua}\ddot{\theta}^{res} + M_{aa}\ddot{\theta}_w^{res} + H_a + \tau_w^{dis} = \tau_w^{ref} \tag{3.74}$$

Assuming the modeling inertia error $(\boldsymbol{M} - \boldsymbol{M}_n)$, gravity term $\boldsymbol{G}$, and the Coriolis and centrifugal force $\boldsymbol{H}$ are a part of disturbance, then the new disturbance $\hat{\tau}_p^{dis}$ and $\hat{\tau}_w^{dis}$ can be given by,

$$M_{nuu}\ddot{\theta}^{res} + M_{nua}\ddot{\theta}_w^{res} = -\hat{\tau}_c^{dis} \tag{3.75}$$

$$M_{nua}\ddot{\theta}^{res} + M_{naa}\ddot{\theta}_w^{res} = \tau_w^{ref} - \hat{\tau}_w^{dis} \tag{3.76}$$

Assuming the camber angle torque term $M_{nua}\ddot{\theta}^{res}$ is a part of disturbance as well, the new disturbance $\hat{\tau'}_w^{dis}$ can be included in,

$$M_{naa}\ddot{\theta}_w^{res} = \tau_w^{ref} - \hat{\tau'}_w^{dis} \tag{3.77}$$

Substituting eq. (6.44) into eq. (6.42), thus,

$$M_{nuu}\ddot{\theta}^{res} + \frac{M_{nua}}{M_{naa}}\tau_w^{ref} = -\hat{\tau}_c^{dis} + \frac{M_{nua}}{M_{naa}}\hat{\tau'}_w^{dis} \tag{3.78}$$

Assuming the left side of eq. (3.78) is the synthesized disturbance,

$$\hat{\tau}_s^{dis} = -\left(M_{nuu}\ddot{\theta}^{res} + \frac{M_{nua}}{M_{naa}}\tau_w^{ref}\right) \tag{3.79}$$

Utilizing a low pass filter and the pseudo differentiation, the final synthesized camber angle disturbance can be given by,

$$\tilde{\tau}_s^{dis} = -\frac{g_s}{s+g_s}\left(\frac{M_{nua}}{M_{naa}}\tau_w^{ref} - M_{nuu}g_s\dot{\theta}^{res}\right) - M_{nuu}g_s\dot{\theta}^{res} \tag{3.80}$$

where, g_s is the cut-off frequency of the low pass filter of SCOB. Fig. 6-7 shows the block diagram of SCOB.

3.5 Concluding Remarks

This chapter explained several disturbance observers. All of them are based on the theory of DOB. In real applications, DC motor rotation angle is measured by encoders. But DOB requires angle velocity feedback to calculate torque disturbance and compensates it. From the differentiation of angle response, velocity should be filtered that must produce time delay. In order to synchronize the input toque and output toque calculation, a pseudo differentiation with a first order low pass filter was applied. The calculation result shows the disturbance torque can be compensated completely by DOB. The concept of compensation of DOB is very useful and can be extended to other systems. RTOB and SCOB are the promotion of DOB. The calculation results show that not only a DC motor, but also the manipulator or the one-wheeled inverted pendulum system can get a good disturbance compensation by disturbance observers.

Chapter 4

Body Balancing Assist Control

4.1 The Purpose of Design (Approach 1)

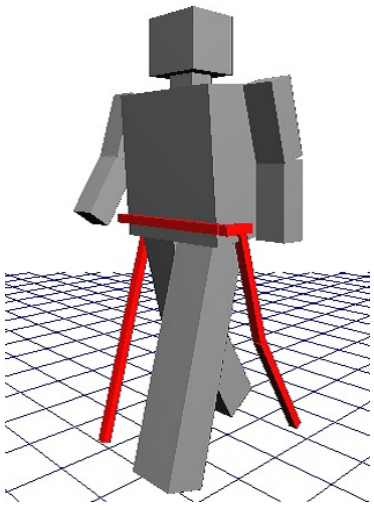

Fig. 4-1: Proposed multi-legged device in simulation (OpenGL).

In the research field of modern walking assist devices, avoiding the elderly or patient from falling down is an important topic. Once they fall down, the consequences would be dangerous. They also hope to walk independently instead of relying on other people's help. Therefore, in this chapter, a multi-legged walking assist device which can keep the elders from falling down and help them walk is proposed as Fig. 4-1. It can also help the elders who have poor walking ability and give them simple walking exercise.

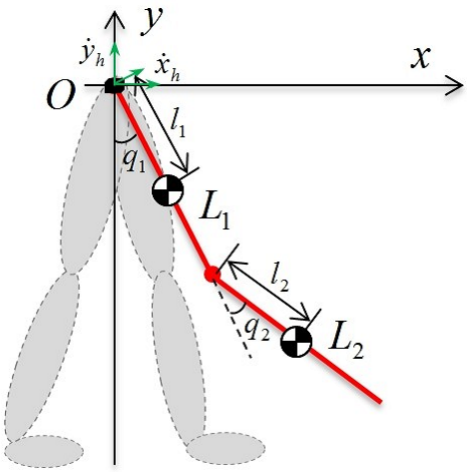

Fig. 4-2: One device leg model.

In order to measure the human body posture, an IMU sensor fixed on the waist part of human is applied in this research. The IMU sensor can not only measure posture but also measure human walking motion. In order to improve the reliability of the system, however, this study introduces links with two encoders to measure human normal walking motion too. To analyse the stability of the proposed multi-legged system, ZMP concept is used. The ZMP is also introduced as a stability index for the multi-legged system.

4.2 Robot Modeling

The model of 2 DOF manipulator used as a leg of the proposed device is described. There are two machine legs for the device. Because the two legs are basically the same, for simplicity, only one leg is modelled in this section. Left device leg consists of link 1 and link 2, right device leg consists of link 3 and link 4. The architecture of a single device leg is shown in Fig. 4-2.

4.2.1 Kinematics and dynamics

In this subsection, kinematics of the device leg is described. The joint space vector can be written as $\boldsymbol{q}_r = [q_1\ q_2]^T$. The end position of the device leg in work space is represented as 2-dimensional vector $\boldsymbol{x}_r = [x_r\ y_r]^T$. Since the base of device leg is not fixed but moved by human waist, the 2-dimensional vector $\boldsymbol{x}_b = [x_h\ y_h]^T$ represents the human waist position measured by the IMU sensor. Forward and

inverse kinematics can be derived as follows.

$$\dot{\boldsymbol{x}}_r = \boldsymbol{J}\dot{\boldsymbol{q}}_r + \dot{\boldsymbol{x}}_b \tag{4.1}$$

$$\dot{\boldsymbol{q}}_r = \boldsymbol{J}^{-1}(\dot{\boldsymbol{x}}_r - \dot{\boldsymbol{x}}_b) \tag{4.2}$$

where $\boldsymbol{J}$ denotes the Jacobian matrix of the device leg. The Jacobian matrix is used to perform mapping from work space to joint space, and it can be written as the following equation.

$$\boldsymbol{J} = \begin{bmatrix} J_{11} & J_{12} \\ J_{21} & J_{22} \end{bmatrix} \tag{4.3}$$

$$\begin{aligned} J_{11} &= L_1 cosq_1 + L_2 cos(q_1 + q_2) \\ J_{12} &= L_2 cos(q_1 + q_2) \\ J_{21} &= -L_1 sinq_1 - L_2 sin(q_1 + q_2) \\ J_{22} &= -L_2 sin(q_1 + q_2) \end{aligned}$$

where $L_1,\ L_2$ represent the length of each device leg link. By using the IMU sensor, the 3-D accelerometer, velocity and position of human waist can be measured. Therefore the kinetic energy of human is given by,

$$K_h = \frac{1}{2} m_h (\dot{x}_h^2 + \dot{y}_h^2) \tag{4.4}$$

Kinetic energy of link 1 can be calculated as,

$$K_1 = \frac{1}{2} m_1 [(\dot{x}_h + l_1 \dot{q}_1 cosq_1)^2 + (\dot{y}_h + l_1 \dot{q}_1 sinq_1)^2] + \frac{1}{2} I_1 \dot{q}_1^2 \tag{4.5}$$

where I_1 is the inertia moment of link 1. l_1 and m_1 represent the center of mass (CoM) length and mass of link 1 respectively. Note the absolute angle of link 2 is $q_2^a = q_1 + q_2$, then the kinetic energy of link 2 can be calculated as,

$$K_2 = \tfrac{1}{2} m_2 [(\dot{x}_h + L_1 \dot{q}_1 cosq_1 + l_2 \dot{q}_2^a cosq_2^a)^2 + (\dot{y}_h + L_1 \dot{q}_1 sinq_1 + l_2 \dot{q}_2^a sinq_2^a)^2] + \tfrac{1}{2} I_2 \dot{q_2^a}^2 \tag{4.6}$$

where I_2 is the inertia moment of link 2. l_2 and m_2 represent the CoM length and mass of link 2 respectively. Potential energy of human is given by,

$$P_h = m_h g y_h \tag{4.7}$$

Potential energy of link 1 can be calculated as,

$$P_1 = m_1 g(y_h - l_1 cosq_1) \tag{4.8}$$

And the potential energy of link 2 can be calculated as,

$$P_2 = m_2 g(y_h - L_1 cosq_1 - l_2 cosq_2^a) \tag{4.9}$$

Thus the Lagrangian of the device leg is given by,

$$L = K_h + K_1 + K_2 - P_h - P_1 - P_2 \tag{4.10}$$

Applying the Lagrangian-Euler formulation for the torque $\boldsymbol{\tau} = [\tau_1 \ \tau_2]^T$ at joint 1 and 2 is,

$$\boldsymbol{\tau} = \frac{d}{dt}\frac{\partial L}{\partial \dot{\boldsymbol{q}}} - \frac{\partial L}{\partial \boldsymbol{q}} \tag{4.11}$$

where $\boldsymbol{q} = [x_h \ y_h \ q_1 \ q_2]^T$. Dynamics equation of the device is derived from the Euler-Lagrange formulation. It can be expressed in the joint space as eq. (4.12).

$$\boldsymbol{\tau} = \boldsymbol{M}(\boldsymbol{q})\ddot{\boldsymbol{q}} + \boldsymbol{C}(\boldsymbol{q}, \dot{\boldsymbol{q}})\dot{\boldsymbol{q}} + \boldsymbol{G}(\boldsymbol{q}) \tag{4.12}$$

where $\boldsymbol{M(q)}$ is the inertia matrix, $\boldsymbol{C}(\boldsymbol{q}, \dot{\boldsymbol{q}})$ represents the Coriolis and centrifugal force, and $\boldsymbol{G}(\boldsymbol{q})$ represents the gravity terms.

$$\boldsymbol{M}(\boldsymbol{q}) = \begin{bmatrix} d_1 cosq_1 & d_1 sinq_1 & d_2 & d_3 cosq_2 \\ d_4 cosq_2^a & d_4 sinq_2^a & d_5 cosq_2 & d_6 \end{bmatrix} \tag{4.13}$$

$$\boldsymbol{C}(\boldsymbol{q}, \dot{\boldsymbol{q}}) = \begin{bmatrix} 0 & 0 & 0 & -d_3 \dot{q}_2^a sinq_2 \\ 0 & 0 & d_5 \dot{q}_1 sinq_2 & 0 \end{bmatrix} \tag{4.14}$$

$$\boldsymbol{G}(\boldsymbol{q}) = \begin{bmatrix} d_1 g sinq_1 \\ d_4 g sinq_2^a \end{bmatrix} \tag{4.15}$$

where,

$$\begin{aligned} d_1 &= m_1 l_1 + m_2 L_1 \\ d_2 &= m_1 l_1^2 + m_2 L_1^2 + I_1 \\ d_3 &= m_2 L_1 l_1 \\ d_4 &= m_2 l_2 \\ d_5 &= m_2 L_1 l_2 \\ d_6 &= m_2 l_1^2 + I_2 \end{aligned}$$

4.2.2 Normal walking behavior

Fig. 4-3 shows how the proposed device cooperates with human walking. In order to measure the human gait motion, two tiny encoder links are fixed on each leg of human. They only measure the rotate angles between posterior and thigh. If human raise his left leg firstly, the right leg of the device will be raised. Similarly, if human raise his right leg firstly, the left leg of device will be raised. Both of the second links of device leg are maintaining an initial angle. Because the impedance control is employed in all of the device links and the joint motion becomes flexible.

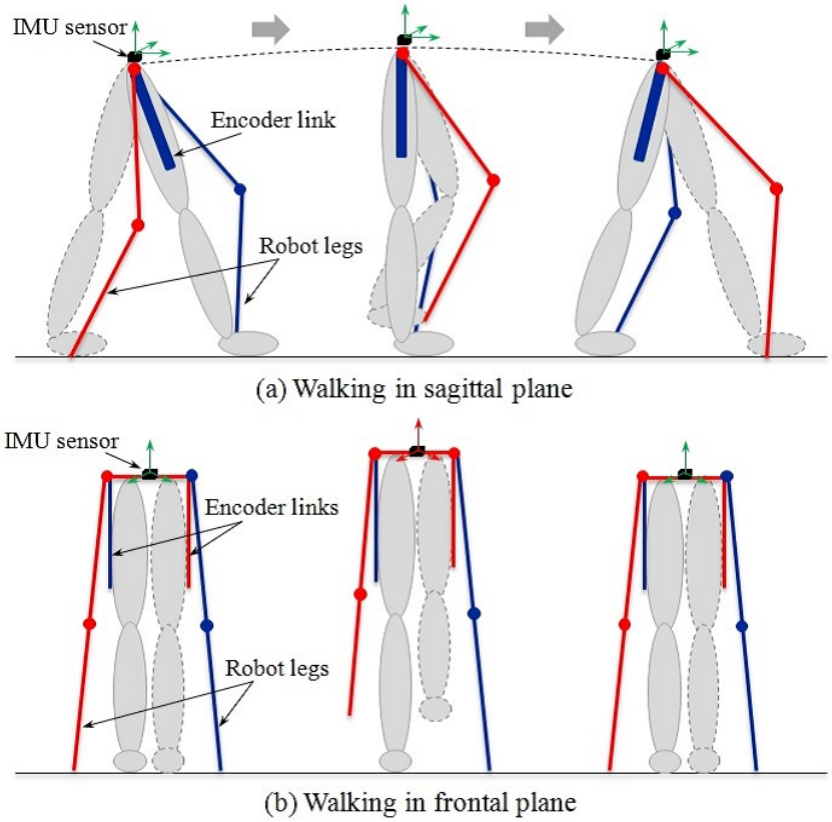

Fig. 4-3: Schematic model of the proposed device.

4.2.3 Avoid falling down motion

The IMU sensor fixed on the waist can also generate 3-D posture information. A quaternion (a, b, c, d) is a four-dimensional complex number that can be used to represent the orientation of a rigid body or coordinate frame in three dimensional space. $\boldsymbol{q}_h^w$ describes the arbitrary orientation and r is a unit vector

described in frame w.

$$\begin{aligned} \boldsymbol{q}_h^w &= [a \quad b \quad c \quad d] \\ &= [\cos\frac{\sigma}{2} \quad -r_x \sin\frac{\sigma}{2} \quad -r_y \sin\frac{\sigma}{2} \quad -r_z \sin\frac{\sigma}{2}] \end{aligned} \tag{4.16}$$

where r_x, r_y and r_z define the components of the unit vector $\boldsymbol{r}$ in the x, y and z axes of frame w respectively.

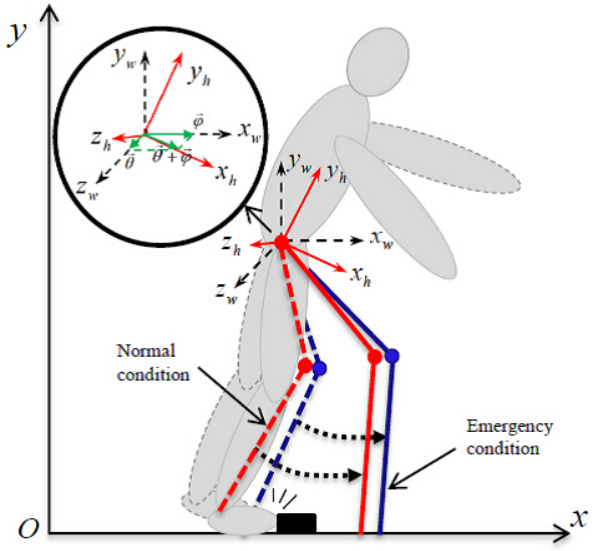

(a) Falling down in sagittal plane

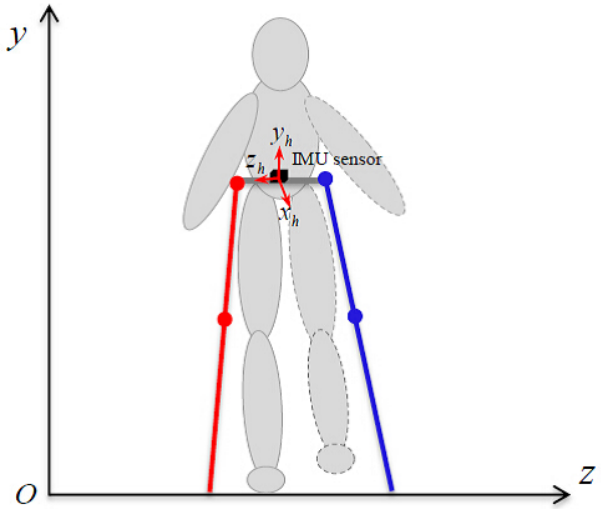

(b) Falling down in frontal plane

Fig. 4-4: Falling down motion.

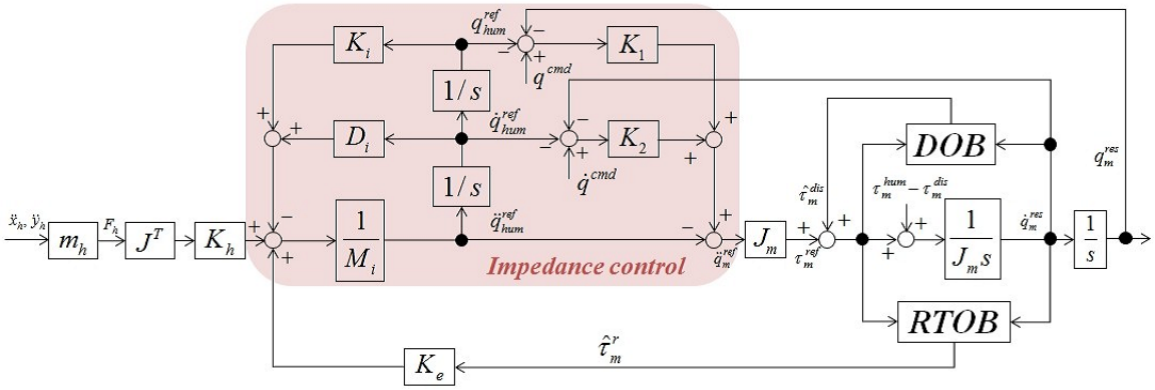

Fig. 4-5: Block diagram of proposed controller.

Applying the quaternion, the Euler angle representation roll θ and pitch φ can be defined by,

$$\theta = -\sin^{-1}(2bd + 2ac) \tag{4.17}$$

$$\varphi = \mathrm{Atan2}(2cd - 2ab, 2a^2 + 2d^2 - 1) \tag{4.18}$$

To avoid the singular point of the pitch angle, the angles are limited by,

$$-90^o \leq \theta \leq 90^o \tag{4.19}$$

$$-180^o < \varphi < 180^o \tag{4.20}$$

In normal walking motion, pitch and roll are almost zero. But in emergency conditions, pitch and roll are not zero absolutely. By applying the vectors of pitch and roll angles, the angle of summation is,

$$\theta^e_{1,3} = \angle(\vec{\theta} + \vec{\varphi}) \tag{4.21}$$

where $\theta^e_{1,3}$ indicates emergent command angle of link 1 or link 3 in Fig. 4-4. Emergency situations are defined as a limitation of $\theta^e_{1,3}$. When $\theta^e_{1,3}$ bigger than the limitation, this avoiding falling down motion starts working. Otherwise, the multi-legged system works in the normal walking assist motion. Fig. 4-4 explains the falling down motion in the world coordinate as well.

4.2.4 Stability analysis

The ZMP stability criterion means it is necessary to keep the ZMP within the support polygon. In this study, in order to prevent the human from falling down, the ZMP stability of the device needs to be analyzed. Since the diameter of the proposed device legs are small, the ground support polygon

is assumed as a point. The IMU sensor that fixed on the human waist part can measure the triaxial acceleration. The position of the IMU sensor can also be assumed as the CoM of the whole system with human. From D'Alembert's principle, ZMP of the proposed two legs device in Fig. 4-4 can be expressed as,

$$ZMP_x = CoM_x - \frac{\ddot{x}y}{\ddot{y} + g} \tag{4.22}$$

$$ZMP_z = CoM_z - \frac{\ddot{z}y}{\ddot{y} + g} \tag{4.23}$$

where $\ddot{x}$ and $\ddot{z}$ are sagittal and frontal acceleration of CoM respectively. y is the vertical position of CoM. CoM_x and CoM_z are sagittal and frontal position of CoM respectively. And ZMP_x and ZMP_z are the sagittal and frontal position of the zero support torque respectively.

4.3 Controller Design

The device motors are based on acceleration control with disturbance observer (DOB) [90] [91] [92]. In addition, by utilizing reaction torque observer (RTOB), force-sensorless control was realized [93] [94]. In this section, in order to make the user feeling comfortable, impedance control is considered. Firstly, command generation of the proposed controller is described.

4.3.1 Command generation

During the normal walking motion, the two encoder links fixed on human legs supply the rotate commands to the device.

$$\boldsymbol{q}^{cmd} = [q_{1e}^{cmd} \quad 0 \quad q_{2e}^{cmd} \quad 0]^T \tag{4.24}$$

where q_{1e}^{cmd} and q_{2e}^{cmd} are encoder link 1 command and encoder link 2 command respectively. In case the pitch or roll angle is bigger than a certain value which means the emergency occurring, the commands are only supplied by IMU sensor. Also, in order to ensure a successful action to stop the falling down motion, the upper limit of rotation angle should be set as well. The command of emergency can be derived as,

$$\boldsymbol{q}^{cmd} = \boldsymbol{q}_s^{cmd} = \boldsymbol{H}(\vec{\theta}, \vec{\varphi}) = \begin{bmatrix} K_r \angle(\vec{\theta} + \vec{\varphi}) - q_{1b}^{cmd} \\ 0 \\ K_l \angle(\vec{\theta} + \vec{\varphi}) - q_{2b}^{cmd} \\ 0 \end{bmatrix} \tag{4.25}$$

where q_{1b}^{cmd} and q_{2b}^{cmd} are initial angle of the device right leg and left leg before the emergency occuring respectively. The details are shown in Fig. 4-6.

4.3.2 Impedance controller

When the device legs touch the ground, the reacting force and the force pushing by human are needed to be considered in Fig. 4-5. During the device leg touching the ground, assuming the end of device leg is not slid. The acceleration of human waist is measured by the IMU sensor, then the extend force for each link motor is,

$$\boldsymbol{\tau}_h = \boldsymbol{J}^T m_h \ddot{\boldsymbol{x}}_b \tag{4.26}$$

where m_h is the mass of testing object. The total extended force for each link motor is,

$$\hat{\boldsymbol{\tau}}_{ext}^{hum} = K_h \boldsymbol{\tau}_h + K_e \hat{\boldsymbol{\tau}}_m^r \tag{4.27}$$

where K_h and K_e are the gains of human force and ground reaction force respectively. $\hat{\boldsymbol{\tau}}_m^r$ is the estimated force of RTOB. By applying the impedance control, the human force acceleration reference is given by,

$$\ddot{\boldsymbol{q}}_{hum}^{ref} = \frac{1}{M_i}(\hat{\boldsymbol{\tau}}_{ext}^{hum} - D_i \dot{\boldsymbol{q}}_{hum}^{ref} - K_i \boldsymbol{q}_{hum}^{ref}) \tag{4.28}$$

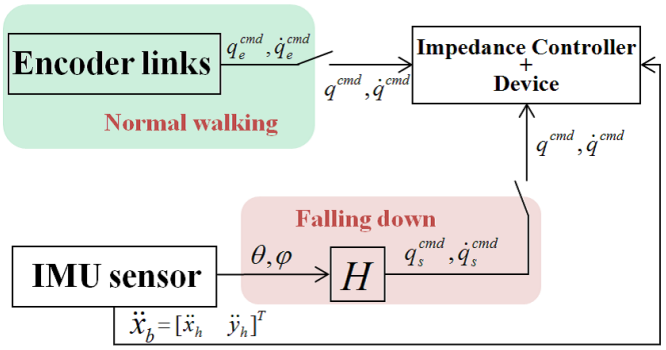

Fig. 4-6: Device joint command generation.

To make a big enough force and hold on the human when they falling down, impedance control gains $M_i, D_i, K_i$are studied. The transfer function of impedance control is,

$$\frac{\boldsymbol{q}_{hum}^{ref}}{\hat{\boldsymbol{\tau}}_{ext}^{hum}} = \frac{1}{M_i s^2 + D_i s + K_i} \tag{4.29}$$

The natural frequency ω_i and damping ratio ζ_i are derived as follows.

$$\omega_i = \sqrt{\frac{K_i}{M_i}} \tag{4.30}$$

$$\zeta_i = \frac{D_i}{2\sqrt{M_i K_i}} \tag{4.31}$$

To adjust a suitable value for the natural frequency and damping ratio, the impedance control gains D_i, K_i are be determined as follows.

$$D_i = 2\zeta_i \omega_i M_i \tag{4.32}$$

$$K_i = {\omega_i}^2 M_i \tag{4.33}$$

By applying the RTOB and IMU sensor to get the environment force, the device motor rotate acceleration reference is given by,

$$\ddot{\boldsymbol{q}}_m^{ref} = -\ddot{\boldsymbol{q}}_{hum}^{ref} + K_1(\boldsymbol{q}^{cmd} - \boldsymbol{q}_{hum}^{ref} - \boldsymbol{q}_m^{res}) + K_2(\dot{\boldsymbol{q}}^{cmd} - \dot{\boldsymbol{q}}_{hum}^{ref} - \dot{\boldsymbol{q}}_m^{res}) \tag{4.34}$$

Fig. 4-6 shows the command generation. For the normal walking cases, the system command $\boldsymbol{q}^{cmd} = \boldsymbol{q}_e^{cmd}, \dot{\boldsymbol{q}}^{cmd} = \dot{\boldsymbol{q}}_e^{cmd}$. For the emergency cases, the system command $\boldsymbol{q}^{cmd} = \boldsymbol{q}_s^{cmd}, \dot{\boldsymbol{q}}^{cmd} = \dot{\boldsymbol{q}}_s^{cmd} = \boldsymbol{v}^{pitch}$.

4.4 Experiments

In this section, experiment procedures and results are explained. In these experiments, normal walking motion and falling down motion were conducted with the proposed controller. Fig. 4-7 shows the real device in the world coordinate. The testing subject of this experiment was a 28 years old man. His height was 175cm and weight was about 60 kg. The iBIS system that is a PC based DSP was used as a processor in this device. A 24V battery was used to supply power for the whole system. The total mass of this device was about 15 kg. The parameters of device and controller are shown in Table 4.1 and Table 4.2 respectively.

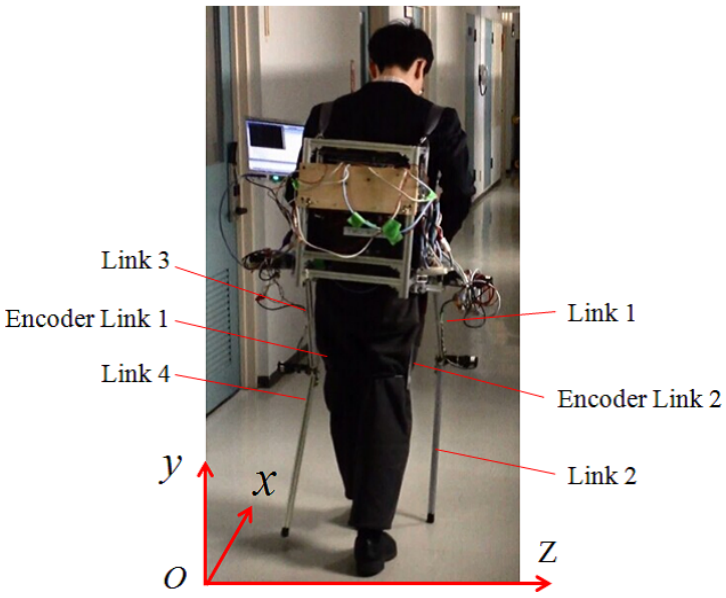

Fig. 4-7: A photograph of the proposed device in normal walking motion.

Table 4.1: Physical parameters of the device.

Name	Value
Width of the machine W	0.420
Length of links (the first link of each leg) L_1, L_3 [m]	0.435
Length of links (the second link of each leg) L_2, L_4 [m]	0.543
CoM length of links l_1, l_3 [m]	0.210
CoM length of links l_2, l_4 [m]	0.270
Length of encoder links [m]	0.310
Mass of link 1 and 3 m_1, m_3 [kg]	0.610
Mass of link 2 and 4 m_2, m_4 [kg]	0.347
Mass of testing object m_h [kg]	60
Rotary encoder resolution R_e [PPR]	400000
Gear reduction of motors G_r	100

Table 4.2: Parameters of controller.

Name	Value
Position gain K_1	200
Velocity gain K_2	10
Human force gain K_h	0.3
Ground reaction force gain K_e	0.7
Virtual mass gain M_i	5.0
Virtual viscosity gain D_i	14.0
Virtual spring gain K_i	40.0
Cut off frequency of DOB	50
Cut off frequency of RTOB	20
Sampling time dt [ms]	0.5

4.4.1 Experiment procedures

1) Experiment 1: Normal walking motion

The device legs can touch the ground like the human using two crutches while walking. Therefore, adding the human two legs, there are four legs in total. Four legs walking can make elders feel there is something to rely. This experiment goal is to know whether the device enables to coordinate with human walking motion.

2) Experiment 2: Falling down motion

Makes the device inclined at a small angle for a test firstly. This test guarantees the system command following the encoder links but not the IMU sensor. Then tests are done for the subject falling forward which means the emergency occurs. After the device legs stop the falling down motion, the testing subject returned to a normal posture by himself. This experiment's goal is to enable the two machine legs to prevent elders from falling down. Fig. 4-4 also describes this falling down motion.

4.4.2 Experiment results

4.4.2.1 Experiment 1 results

Fig. 4-8 shows the results of experiment 1. There are four normal walking steps in the experiment. In Fig. 4-8 (a), the machine leg link 1 motor tracks the encoder link 1 command. The tracking error

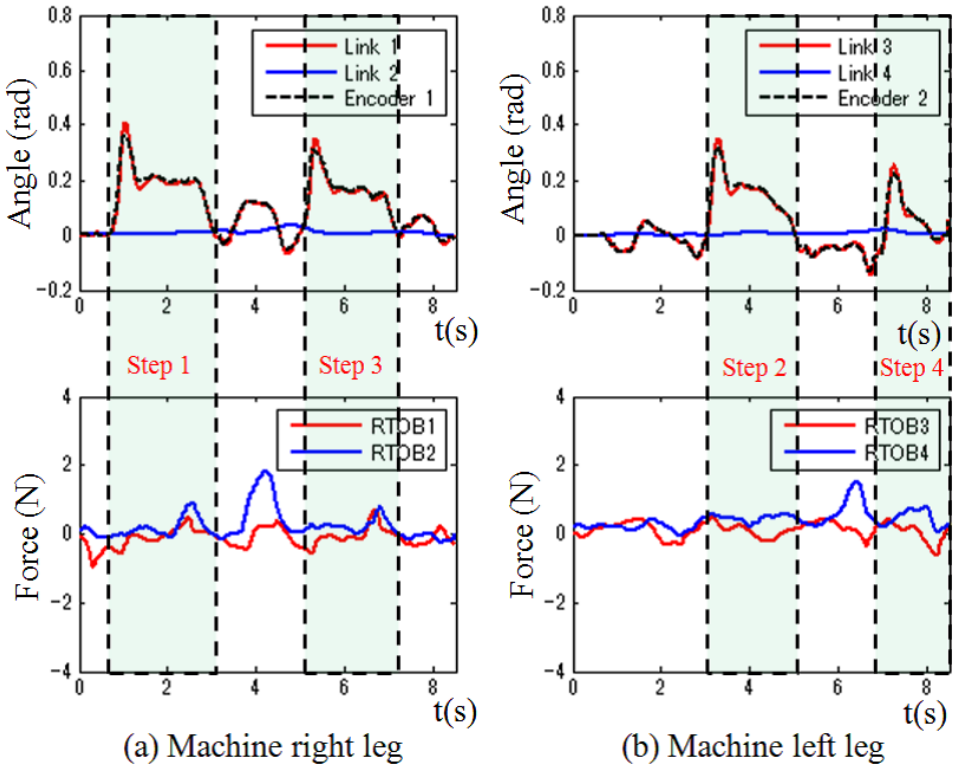

Fig. 4-8: Machine legs rotate angle and contact force in normal walking motion.

depends on the gains K_1, K_2. If the position gain is larger, the tracking error is smaller. But it does not mean that the smaller the error is, a better system response is achieved. In order to reduce the sensitivity of the system, the gains should not be very large. Since the velocity command is noisy, the velocity gain should be reduced accordingly as well. In this study, for link 1 and link 3, the position and velocity gains were chosen as 400 and 40 respectively. The bound of position gain is recommended between 100 to 625. In accordingly, the bound of velocity gain is recommended between 20 to 50. For link 2 and link 4, the position and velocity gains were chosen as 100 and 20 respectively. The bound of position gain is recommended between 81 to 225, and the bound of velocity gain is recommended between 18 to 30. The tracking command of the machine leg link 2 is zero. But because of impedance control, the rotation result is not always zero. The RTOB results indicate that there is an obvious reaction force when the machine leg has contacted with the ground.

To analyse the stability of the device with human walking, ZMP tracking performance is introduced in Fig. 4-9. Measuring CoM_x and measuring CoM_z are obtained by the IMU sensor. ZMP_x and ZMP_z are obtained by eq. (4.22) and eq. (4.23) respectively. Because this device is not similar to the biped

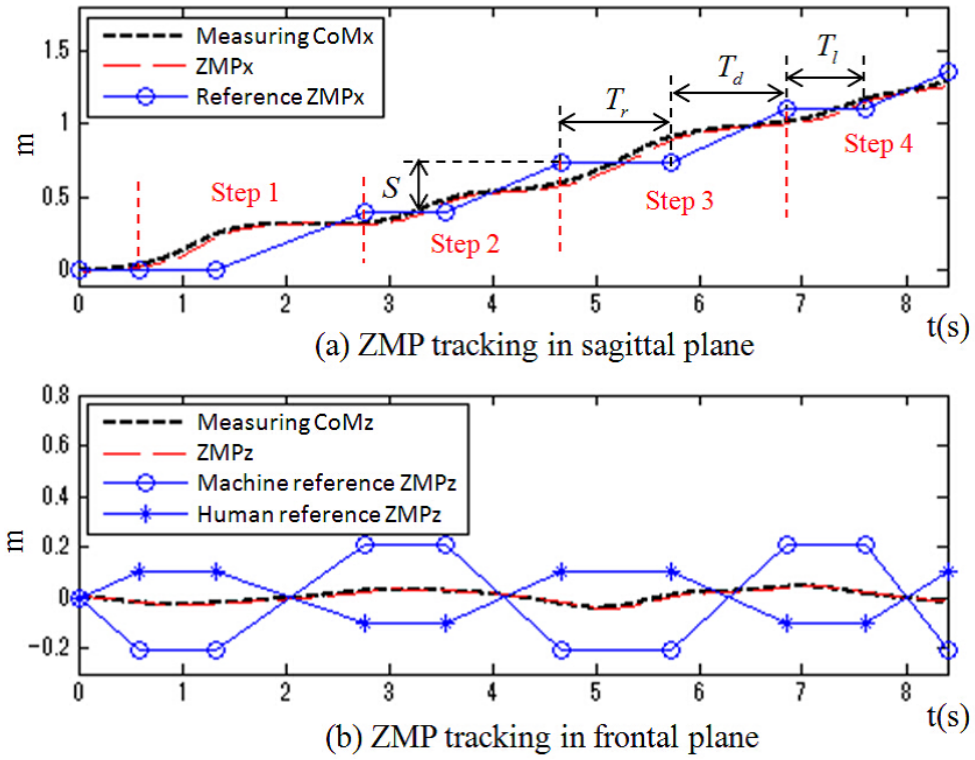

Fig. 4-9: ZMP tracking performance in normal walking motion.

robot, there is no desired ZMP trajectory in advance. In this , reference ZMP_x is a point connection from the experiment data. It is only a reference for the system stability. The flex points are decided by the moments of device contacting or leaving the ground. Denotes the rotate position is 0 m in 0 second as (0, 0), the other flex points are (0, 0.58), (0, 1.33), (0.4, 2.77), (0.4, 3.55), (0.74, 4.67), (0.74, 5.72), (1.1, 6.84), (1.1, 7.47) and (1.35, 8.40). T_r and T_l are the period of single support phase of right and left device leg respectively. T_d is double support phase period, S is the device stride of one step. Reference ZMP_z is obtained by the similar way as ZMP_x. -0.21 m or 0.21 m is a half of the device width W. -0.1 m or 0.1 m is a half of the distance between the two feet fo human. The results show the whole system is very stable during the human walking in a normal slow speed motion.

4.4.2.2 Experiment 2 results

There are many kinds of falling down motion for the elders. For simplicity, only falling forward motion was considered. Also, the device two legs did the same motion in this emergency case. Fig. 4-10 and Fig. 4-11 show the results of experiment 2. In the experiment, the current device motors did not have

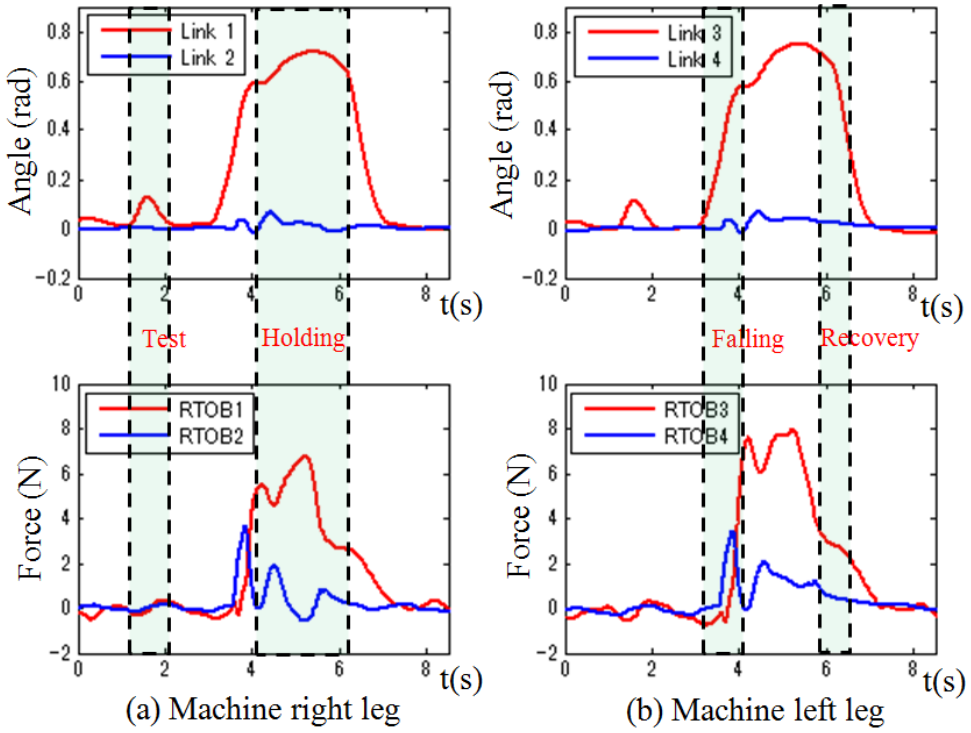

Fig. 4-10: Machine legs rotate angle and contact force in falling down motion.

enough power to hold on the human body when he falls down. In the future work, we need to change bigger motors for the device links. Therefore in this experiment, for the safety, the testing subject fell forward and used his hands to support on a wall. That is why the RTOB force is not very big in Fig. 4-10.

In Fig. 4-11 (a), reference ZMP_x is obtained in the same way as the normal walking motion. Because human feet did not move on the ground in this experiment, there is no reference ZMP_x data for the human. T_f and T_r are the period of falling down and recovery respectively. T_h is device holding period. Maybe this case can not represent all of falling down motions, but at least it can make it possible to prevent elders from falling down. In Fig. 4-11 (b), machine reference ZMP_z and human reference ZMP_z are obtained by the similar way as reference ZMP_x. The time of flex points are 0 s, 2.95 s, 3.94 s, 5.6 s, 6.79 s and 8.3 s. During the period of T_f and T_r, because both of the device two legs are leaving the ground, there is no data for the machine reference ZMP_z. The results show the whole system is stable even in this falling forward down motion. Finally, if this system is applied to various users, the initial joint angle device of two legs should be adjusted according to the height of the user. Also, the impedance control gains are need to be adjusted according to different weight users.

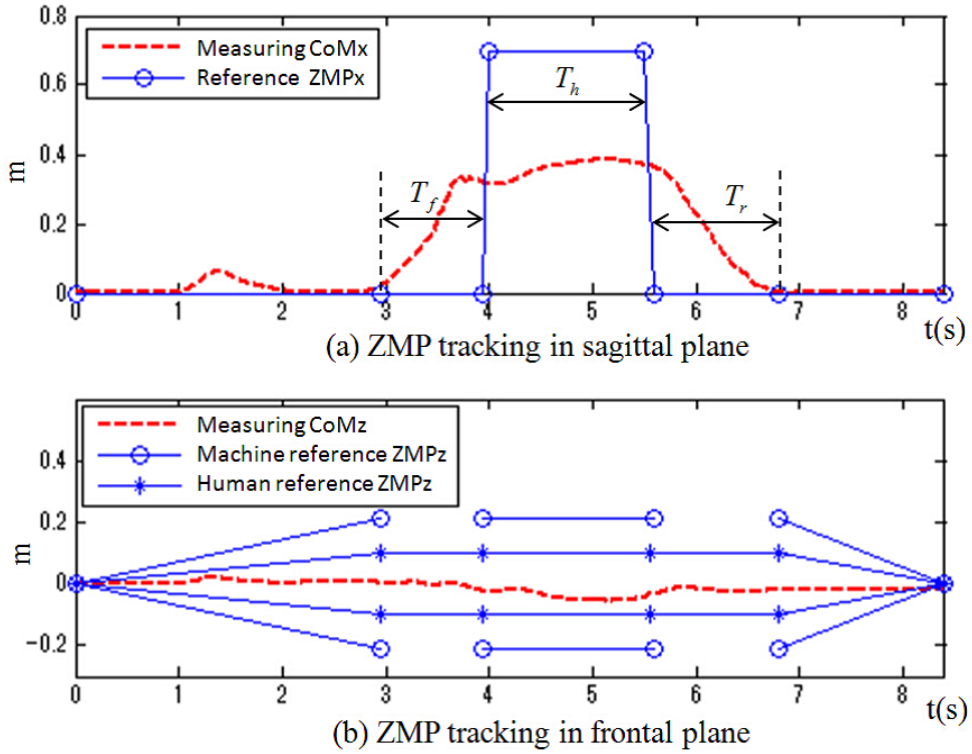

Fig. 4-11: ZMP tracking performance in falling down motion.

4.5 Concluding Remarks

In this chapter, a novel multi-legged system device is proposed. The purpose of this research is to hold and help elders walk using two robotic crutches and prevent them from falling down when an emergency occurs. Since the device legs are 2 DOF manipulators, only forward falling down motions were discussed. ZMP tracking results were introduced as a stability index for the whole system. The results also indicated that the proposed device can stop human from falling down when the emergency occurs. After this falling forward down motion, human can return to the normal safe posture by themselves and keep on normal walking. Finally, Fig. 4-12 shows a photograph of striding over a step of the proposed device. Although this research is not perfect, it can provide a possible solution to prevent the elderly or patient from falling down in the future society.

Fig. 4-12: Striding over a step photograph of the proposed device.

Chapter 5

Partner's Cooperation Control

5.1 The Purpose of Design (Approach 2)

Lacking in adequate care for the elders, especially those who are walking with inconvenience is becoming a growing problem for the aging society. It is also necessary for the elders to exercise walking in order to keep normal social life. Many kinds of walking aids have been developed, such as conventional stick, quad stick, rollator cart, walking frame, gait harness, etc. Recently, some more powerful and effective electrical walking aids have also been developed, among which the walking assist devices invented by HONDA are the most representative ones. However, most of the newly invented devices are not enough to effect as a people who can support the elders with her/his hands. Also, most devices are only suitable for the elders who have a fairly-well walking ability. So far, there are few researches focusing on the walking cooperation between human and robot.

In this chapter, in order to help the elders who have poor walking ability and exercising from the simple walking, a robot which can serve the elders as a partner or a nurse to walk is also needed. Fig. 5-1 shows the proposed walking assist device in simulation. In order to achieve this target, detecting human walking motion and robot control strategy are needed. The IMU sensor fixed on elder's foot to estimate human's walking motion is proposed. A manipulator fixed on a mobile robot can support and help the elders with their walking. Also, it can correct the moving position error between human and robot. Therefore, this mobile manipulator robot moving beside the elders is able to coordinate their steps as the elders swing their feet on the ground, and it leads to a much more human-friendly system. The foot motion filtering algorithm incorporate orientation estimation, walking acceleration/velocity estimation,

and gait detection. Foot orientation estimate is obtained by Euler angles from the IMU sensor. Walking acceleration/velocity estimation is accomplished by a Butterworth filter and compliance control. To sense zero velocity and enable the robot to stop when human stop walking, gait detection is obtained by using a simple timer algorithm. In addition, the manipulator can compensate the moving position error by employing force control. The performance of the approach proposed in this chapter has been examined by both simulations and experiments. Hence, it is prospected that a more human-friendly walking assist robot can be achieved using the method proposed.

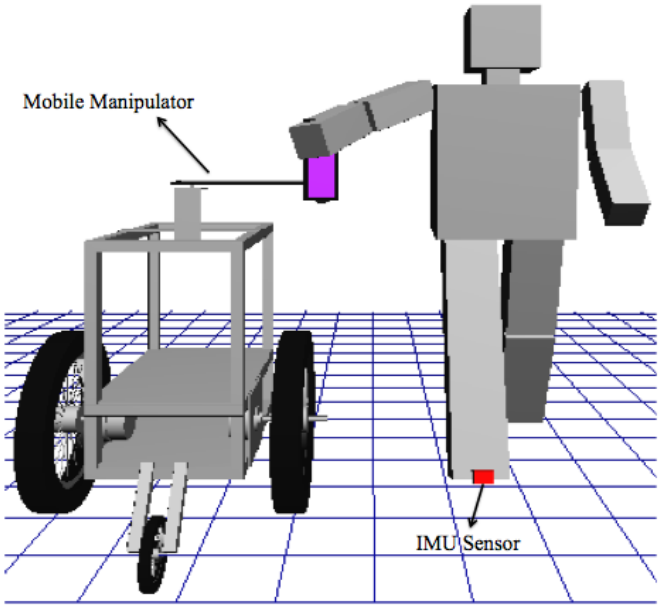

Fig. 5-1: Proposed walking assist device in simulation (OpenGL).

5.2 Walking Behavior Estimation with IMU Sensor

Human walking behavior can be divided into walking phase and standing phase. In Fig. 5-2(a), an IMU sensor is fixed on foot. During the walking phase, the IMU sensor sends human walking acceleration signal to the device. In order to detect starting walking and stopping walking which indicate zero velocity, walking phase consists of double support (DS), single support (SS) and starting counter motion, see Fig. 5-2(b). During the standing phase, human can compensate the walking position error by operating the manipulator mounted on a mobile device. Also, human can change the orientation of device by rotating her/his foot. These two phases are independent of each other, and all data are reset while starting walking or stopping.

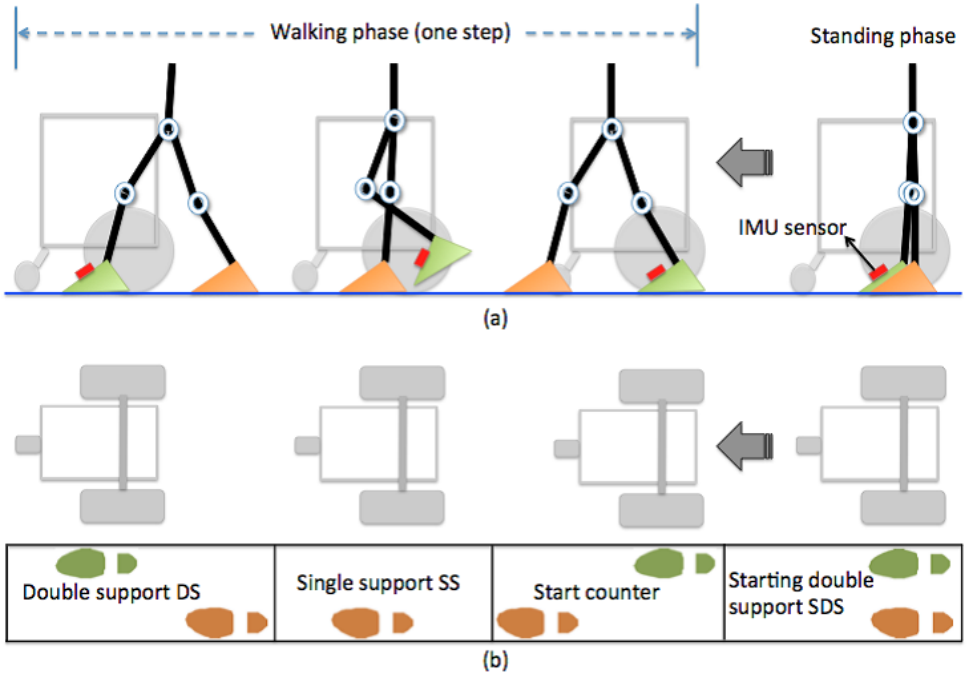

Fig. 5-2: Human walking behavior.

The IMU sensor is designed to replace traditional mechanical gyroscopic instruments and provide superior reliability and accuracy. Fig. 5-3 shows the data process from the IMU sensor fixed on human's foot. To avoid the singularity of Euler angles, pitch, roll and yaw angles are obtained by once integral calculation of gyroscope (angle rate sensor). The gait motion can be divided into walking phase and standing phase in simply. Gait phase detection can update the zero velocity to the device and make sure that the device stop moving while the elders stop walking. The following subsections explain the details.

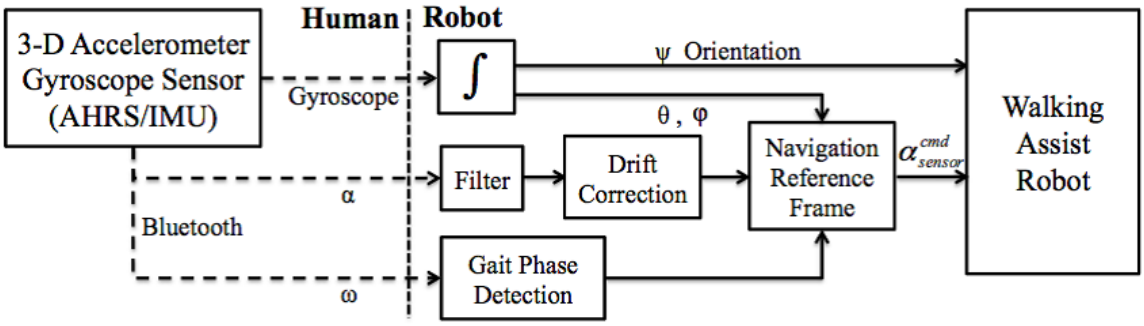

Fig. 5-3: 3-D IMU sensor data processing.

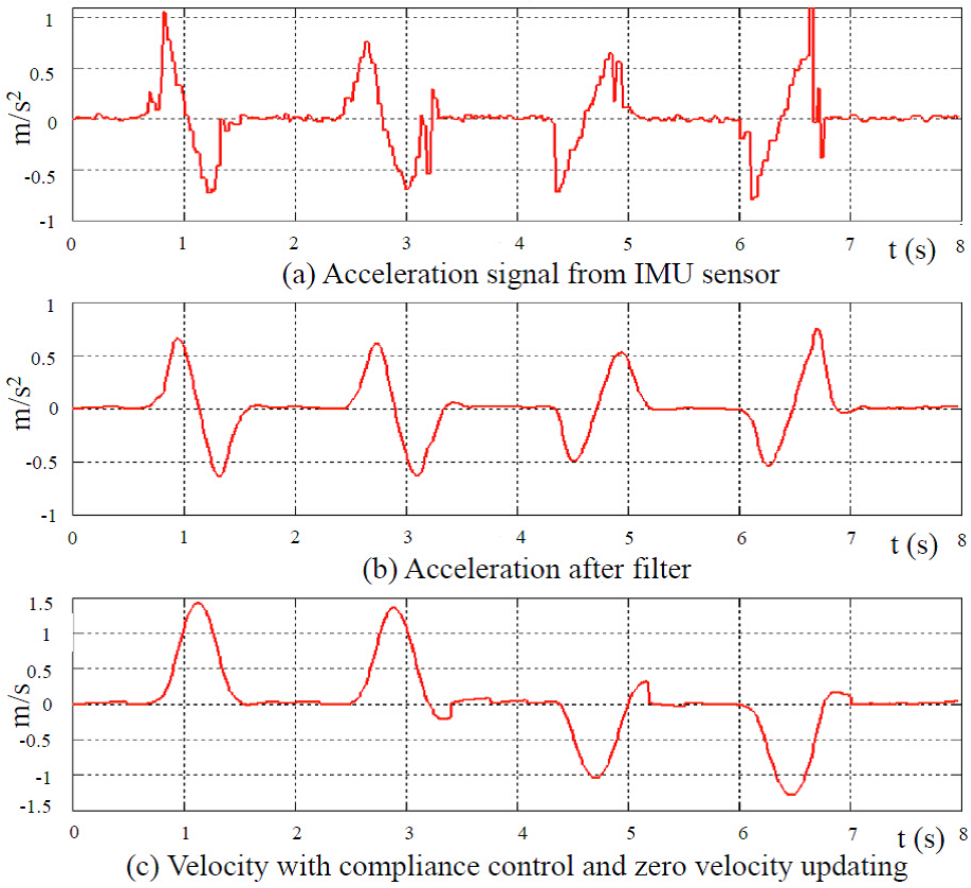

Fig. 5-4: Acceleration data after filter.

5.2.1 Butterworth filter

From the first DS phase to the SS phase and the second DS phase, one step can be defined. Assuming the walking frequency of elders is 60 steps/min (1 Hz), the stride frequency is 0.5 Hz. The format of a digital second-order Butterworth filter, which processes the acceleration data in the time domain(9), is as follows,

$$y(k) = m_0x(k) + m_1x(k-1) + m_2x(k-2) + n_1y(k-1) + n_2y(k-2) \tag{5.1}$$

Consider the effect of filtering and appropriate time delay, the cut-off frequency is designed as 10 Hz and the sampling frequency is selected 256 Hz. Thus the coefficients of the filter can be chosen as,

$$y(k) = 0.0128x(k) + 0.0256x(k-1) + 0.0128x(k-2) + 3.3112y(k-1) - 1.4135y(k-2) \tag{5.2}$$

Fig. 5-4 shows the original acceleration signal and the filtered signal by using this filter in simulation. This simulation is done in OpenGL, the original data is obtained by an IMU sensor.

5.2.2 Human gait velocity measurement

Many studies(10)-(14) have already focused on detecting human walking motion by inertial sensors. For convenience, assume the axis y is the orientation of walking. The human walking forward horizontal acceleration α^m_{sensor} is,

$$\alpha^m_{sensor} = \alpha^m_z \cos\theta_y - \alpha^m_y \sin\theta_y \tag{5.3}$$

where α^m_z and α^m_y represent the measurement acceleration of z-axis and y-axis respectively. θ_y is the pitch angle. The forward and backward horizontal velocity is,

$$v(t) = \int_0^t \alpha^m_{sensor}(t)dt, \quad (t \in [0, T]) \tag{5.4}$$

Note the initial pitch angle as θ_{init}, thus,

$$\theta_y(t) = \int_0^t \dot{\theta}_y(t)dt + \theta_{init} \tag{5.5}$$

$$\theta_{init} = sin^{-1}\frac{\alpha_z}{g} \tag{5.6}$$

During the integrations, there must exist error. Assuming the measured acceleration containing error α_e, thus the acceleration command is given by,

$$\alpha^{cmd}_{sensor}(t) = \alpha^m_{sensor}(t) + \alpha_e, \quad (\alpha_e = \frac{v(T)}{T}) \tag{5.7}$$

where $v(T)$ is the velocity at the end of the swing phase and T is the total time of one step. In a real-time experiment, T is decided by an average value of steps.

Fig. 5-5 shows the velocity offset that is due to acceleration drift and Yaw signal curve. The velocity curve indicates two steps forward and two steps backward. The Yaw signal is from Euler angle of IMU sensor, it also means the orientation of human. The walking velocity during the walking phase can be computed as,

$$v(t) = \int_0^t [\alpha_a(t) + \alpha_e]dt = \int_0^t \alpha_a(t)dt + \int_0^t \alpha_e dt = v_a(t) + \alpha_e t \tag{5.8}$$

The command velocity $v(T)$ is composed of the actual velocity and bias error. It can be assumed the bias error is a parameter that is proportional to the time t. In this study, the bias error is compensated by the compliance control based on the equivalent acceleration force. And it is explained in the next section.

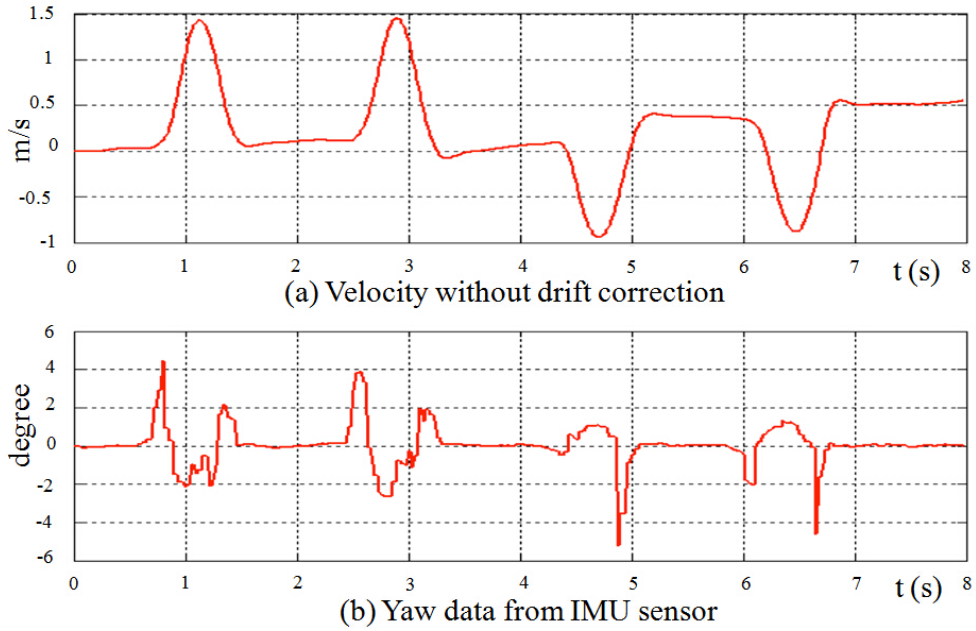

Fig. 5-5: Velocity offset and Yaw data.

5.2.3 Human walking orientation measurement

The gyroscope sensor inside of IMU sensor provides the 3-D rotate angle rate data to the device. It is easy to obtain the rotate angle by once integral calculation. The angles ψ, θ and δ describe an orientation of roll, pitch and yaw respectively.

$$\varphi = \int_0^t \omega_\varphi(t) \tag{5.9}$$

$$\theta = \int_0^t \omega_\theta(t) \tag{5.10}$$

$$\delta = \int_0^t \omega_\delta(t) \tag{5.11}$$

Fig. 5-6 shows a gyroscope rotation data of yaw and yaw angle. This test setup is clockwise 180 degree $\rightarrow$ anticlockwise 180 degree $\rightarrow$ anticlockwise 180 degree $\rightarrow$ clockwise 180 degree in turn. This result shows the rotate angles can be obtained by gyroscope in any time, and reset to be zero while rotate rate is zero. By applying this yaw data, human can operate the orientation of the device easily. Here, the gyroscope rotation data of yaw is just a testing result.

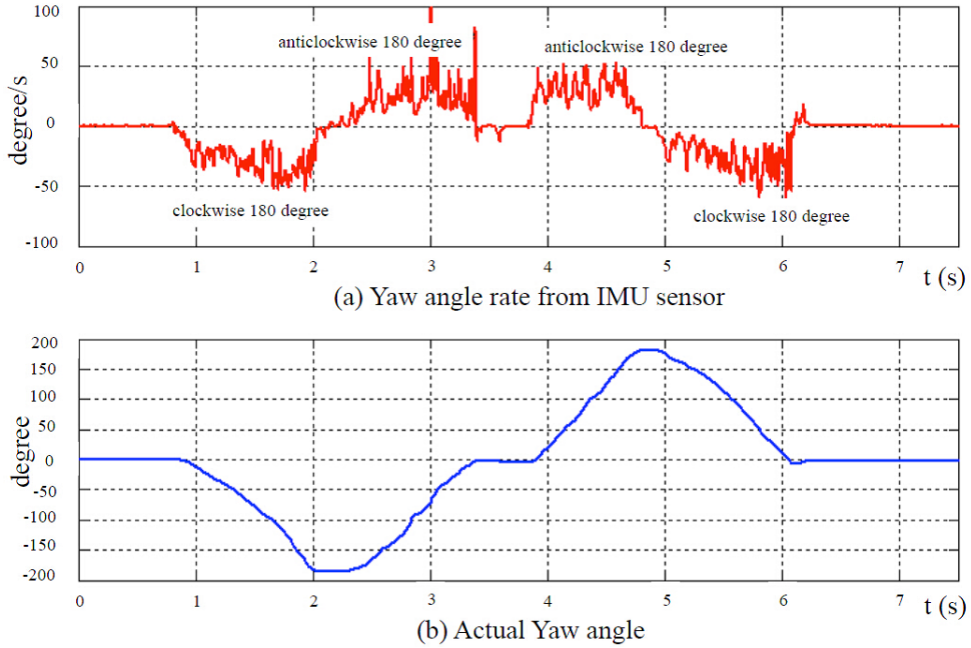

Fig. 5-6: Rotation data for testing (yaw).

5.3 System Modeling

Fig. 5-8 shows the system controller diagram. In standing phase, the manipulator motors do not work but only the encoders of the motors supply the rotating commands to the device wheels. In walking phase, the IMU sensor supplies moving commands to the device wheels, the manipulator motors should go back to the initial position and keep fixing by the zero rotating command. In this case, the manipulator can lead and pull the hand of human. Fig. 6-3 shows the modeling of the device and manipulator. R_x, R_y and R_z are real coordinates of the device and mobile manipulator. There are two links and two motors of this manipulator. In the standing phase, link 1 can compensate the position error while forward or backward walking, and link 2 can correct the rotation angle while human and device change their orientation.

Assuming the device system frame as one link and the big two wheels as one link's motor, ψ_0, ψ_1 and ψ_2 are the rotation angles for each link. $\sum W$ is the world coordinates, W_X, W_Y and W_Z are world coordinates of device and manipulator. Fig. 5-4 shows original data, acceleration after filter and calibrated velocity. By applying compliance control, the filtered acceleration drift can be corrected. It indicates the velocity offset can be reduced and zero velocity is working while human stop walking. Zero velocity is important for this system if the users are the elders. From the kinematics of this device

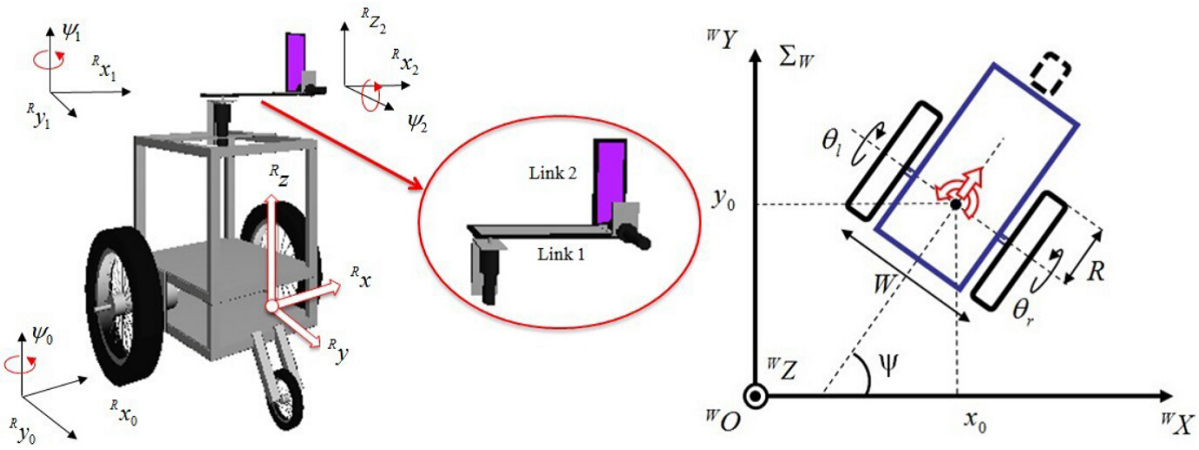

Fig. 5-7: Walking assist device modeling.

system, the relationship of device position and rotation angle is,

$$\boldsymbol{v}_c^{cmd} = \begin{bmatrix} \dot{x}_0 \\ \dot{y}_0 \\ \dot{\psi} \end{bmatrix} = \boldsymbol{J}_p \begin{bmatrix} \dot{\theta}_r \\ \dot{\theta}_l \end{bmatrix} \tag{5.12}$$

where the Jacobian matrix is,

$$\boldsymbol{J}_p = \begin{bmatrix} \frac{R}{2}cos\psi & \frac{R}{2}cos\psi \\ \frac{R}{2}sin\psi & \frac{R}{2}sin\psi \\ \frac{R}{W} & -\frac{R}{W} \end{bmatrix} \tag{5.13}$$

And the pseudo-inverse matrix of Jacobian is,

$$\boldsymbol{J}_p^+ = (\boldsymbol{J}_p^T \boldsymbol{J}_p)^{-1} \boldsymbol{J}_p^T \tag{5.14}$$

Substitute eq. (5.13),

$$\boldsymbol{J}_p^+ = \begin{bmatrix} \frac{cos\psi}{R} & \frac{sin\psi}{R} & \frac{W}{2R} \\ \frac{cos\psi}{R} & \frac{sin\psi}{R} & -\frac{W}{2R} \end{bmatrix} \tag{5.15}$$

Then the deformation of eq. (5.12) is,

$$\begin{bmatrix} \dot{\theta}_r \\ \dot{\theta}_l \end{bmatrix} = \boldsymbol{J}_p^+ \begin{bmatrix} \dot{x}_0 \\ \dot{y}_0 \\ \dot{\psi} \end{bmatrix} \tag{5.16}$$

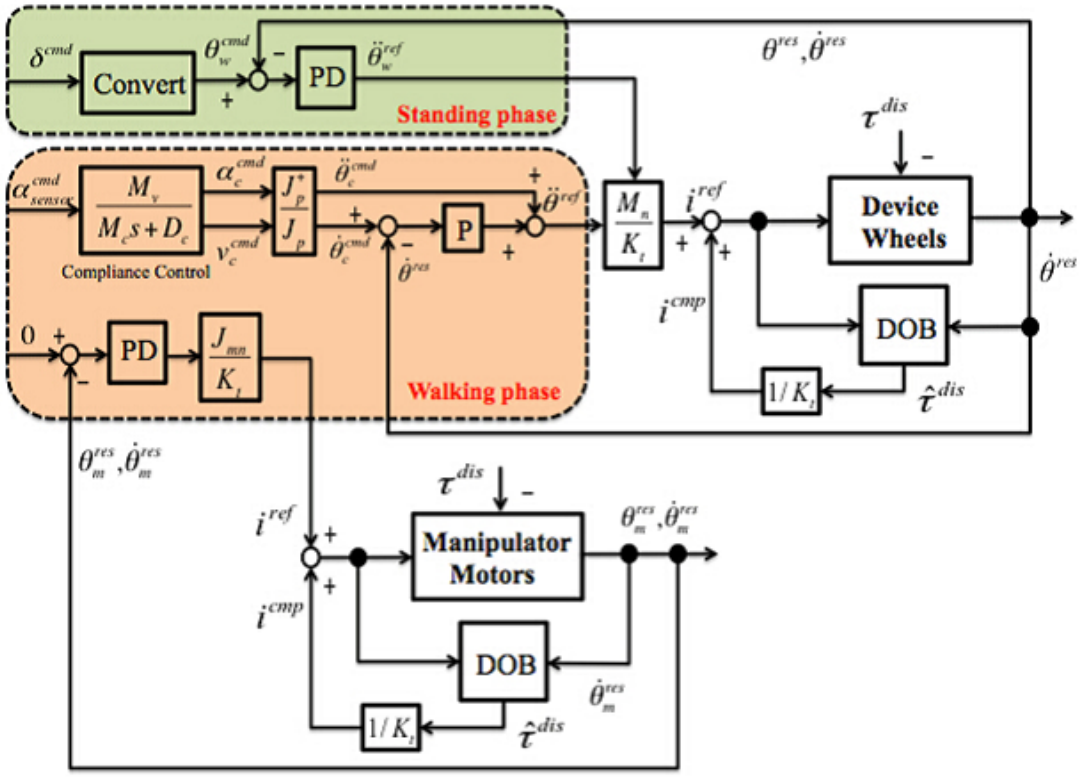

Fig. 5-8: System controller design.

Doing once derivation and neglecting an enough small term,

$$\begin{bmatrix} \ddot{\theta}_r \\ \ddot{\theta}_l \end{bmatrix} = \boldsymbol{J}_p^{+}\boldsymbol{\alpha}_c^{cmd} + \dot{\boldsymbol{J}}_p^{+}\boldsymbol{v}_c^{cmd} \approx \boldsymbol{J}_p^{+}\begin{bmatrix} \ddot{x}_0 \\ \ddot{y}_0 \\ \ddot{\psi} \end{bmatrix} \tag{5.17}$$

The dynamics of this device system is,

$$\boldsymbol{\tau} = \boldsymbol{M}\ddot{\boldsymbol{\theta}}^{ref} \tag{5.18}$$

Assuming the device energy is,

$$K = \frac{mR^2}{8}(\dot{\theta}_r + \dot{\theta}_l)^2 + \frac{1}{2}J_w(\dot{\theta}_r + \dot{\theta}_l)^2 + \frac{1}{2}J_\psi[\frac{R}{W}(\dot{\theta}_r - \dot{\theta}_l)]^2 \tag{5.19}$$

Then eq. (5.18) can be expressed as,

$$\begin{bmatrix} \tau_r \\ \tau_l \end{bmatrix} = \boldsymbol{M}\ddot{\boldsymbol{\theta}}^{ref} = \begin{bmatrix} \frac{mR^2}{4} + J_w + \frac{J_\psi R^2}{W^2} & \frac{mR^2}{4} - \frac{J_\psi R^2}{W^2} \\ \frac{mR^2}{4} - \frac{J_\psi R^2}{W^2} & \frac{mR^2}{4} + J_w + \frac{J_\psi R^2}{W^2} \end{bmatrix} \begin{bmatrix} \ddot{\theta}_r^{ref} \\ \ddot{\theta}_l^{ref} \end{bmatrix} \tag{5.20}$$

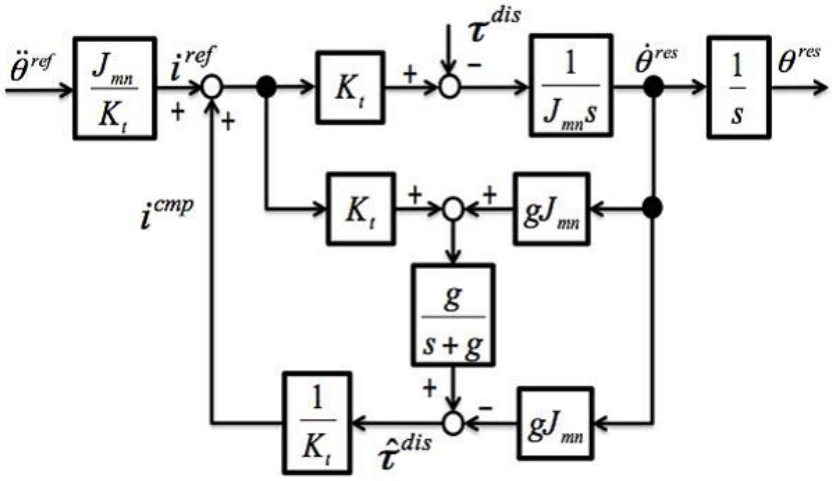

Fig. 5-9: Disturbance observer block diagram.

Table 5.1: Parameters of DOB.

Variables	Unit	Explanation
K_t	Nm/A	Torque constant
J_{mn}	kgm^2	Nominal inertia
τ^{dis}	Nm	Disturbance torque
g	rad/s	Cut-off frequency of DOB

The nominal inertia matrix,

$$\boldsymbol{M}_n = \begin{bmatrix} \frac{mR^2}{4} + J_w + \frac{J_\psi R^2}{W^2} & 0 \\ 0 & \frac{mR^2}{4} + J_w + \frac{J_\psi R^2}{W^2} \end{bmatrix} \tag{5.21}$$

5.4 Controller Design

To reduce the acceleration drift, compliance control based on equivalent acceleration force is designed by,

$$\boldsymbol{F}^{cmd} = M_c \boldsymbol{\alpha}_c^{cmd} + D_c \boldsymbol{v}_c^{cmd} = M_v \boldsymbol{\alpha}_{sensor}^{cmd} \tag{5.22}$$

where M_v is virtual mass that can be defined as 1, thus,

$$\boldsymbol{\alpha}_{sensor}^{cmd} = M_c \boldsymbol{\alpha}_c^{cmd} + D_c \boldsymbol{v}_c^{cmd} \tag{5.23}$$

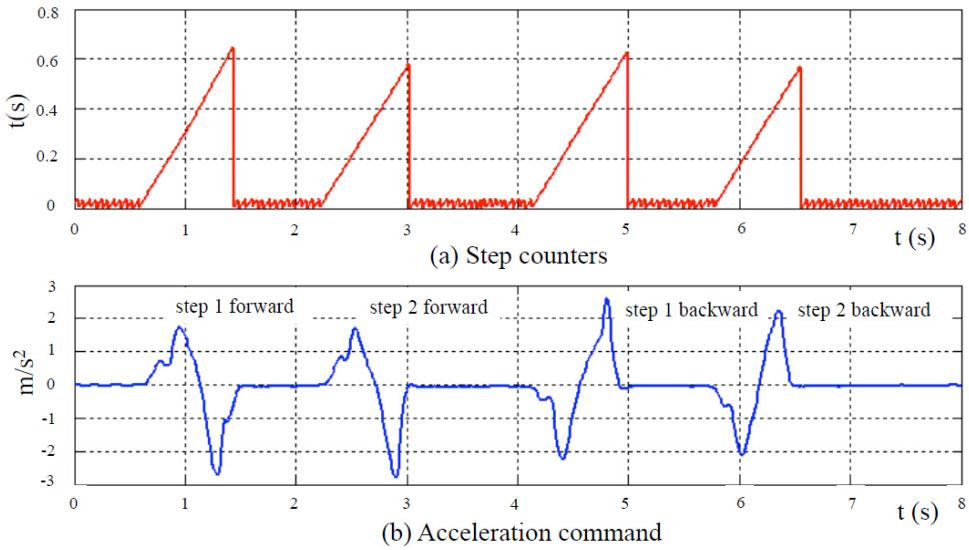

Fig. 5-10: Time counter and filtered acceleration.

The acceleration reference is,

$$\begin{bmatrix} \ddot{\theta}_r^{ref} \\ \ddot{\theta}_l^{ref} \end{bmatrix} = \ddot{\boldsymbol{\theta}}^{ref} = K_p(\dot{\boldsymbol{\theta}}_c^{cmd} - \dot{\boldsymbol{\theta}}^{res}) + \ddot{\boldsymbol{\theta}}_c^{cmd} \tag{5.24}$$

Table 5.2 shows the parameter definitions of the modeling of the device system. There are two DC motors driving the two wheels. A universal wheel that can support the whole device is fixed in the front of the two big wheels. In order to control rotation of the device DC motors well, disturbance observer (DOB) [90] [91] [92] is a good tool for compensating disturbances. Fig. 5-9 shows the diagram of DOB and Table 5.1 shows the definitions of parameters. During the standing phase, by the mobile manipulator, human can compensate the position and orientation errors. And during the walking phase, the manipulator returns to the initial position.

$$\boldsymbol{\theta}_w^{cmd} = \begin{bmatrix} \theta_{rw}^{cmd} \\ \theta_{lw}^{cmd} \end{bmatrix} = \frac{\pi W}{360R} \begin{bmatrix} \delta^{cmd} \\ -\delta^{cmd} \end{bmatrix} \tag{5.25}$$

The relationship between IMU sensor orientation angle and device wheel is shown in eq. (5.25).

5.5 Experiments

The experiment setup is designed to two steps forward and two steps backward. Fig. 5-10 shows the time counter curve and acceleration signal after the filter. The time counter (1000Hz) is applied to

Table 5.2: Parameters of modeling.

Variables	Unit	Explanation
W	m	Space between wheels
R	m	Radius of wheels
x_0, y_0	m	Device position in world coordinates
ψ	rad	Device direction angle
θ_r, θ_l	rad	Rotation angle of wheels
m	kg	Mass of the device
α^m_{sensor}	m/s^2	Horizontal measurement acceleration
α^m_z	m/s^2	Measurement acceleration of z axis
α^m_y	m/s^2	Measurement acceleration of y axis
$\boldsymbol{\alpha}^{cmd}_{sensor}$	m/s^2	Calibrated acceleration
M_c, D_c		Compliance control gain
$\boldsymbol{v}^{cmd}_c$	m/s	Velocity command
$\boldsymbol{\alpha}^{cmd}_c$	m/s^2	Acceleration command
$\boldsymbol{M}_n$		Nominal inertia matrix
K_p		P controller gain
J_w	kgm^2	Inertia of the wheels
J_ψ	kgm^2	Inertia around center of axle

counter the human pitch angle rate. If the counter times are bigger then 50 (counter plus 1 if pitch angle rate is zero) which also means pitch angle is continued to maintain zero for 5 ms. Fig. 5-11 shows the experimental results of velocity response and velocity error. By using DOB, the velocity can be tracked well. Fig. 5-12 shows the position response and position error. In position response plots, red curve is an integral value of velocity command. The blue curve is the real position response of device.

Since the drift of acceleration, the position error also has a drift for each step. The position error can be compensated by human power moving the mobile manipulator. Again, by using compliance control and zero velocity updating, the velocity offset has been reduced. It also shows the acceleration controller is viable for this closed-loop control system. Fig. 5-13 shows the orientation respond and error. It indicates that biggest errors (about 5 degree) are occurring in the period of rapid orientation changing.

Fig. 5-14 shows the real walking assist device. The iBIS system which is a PC based DSP was used

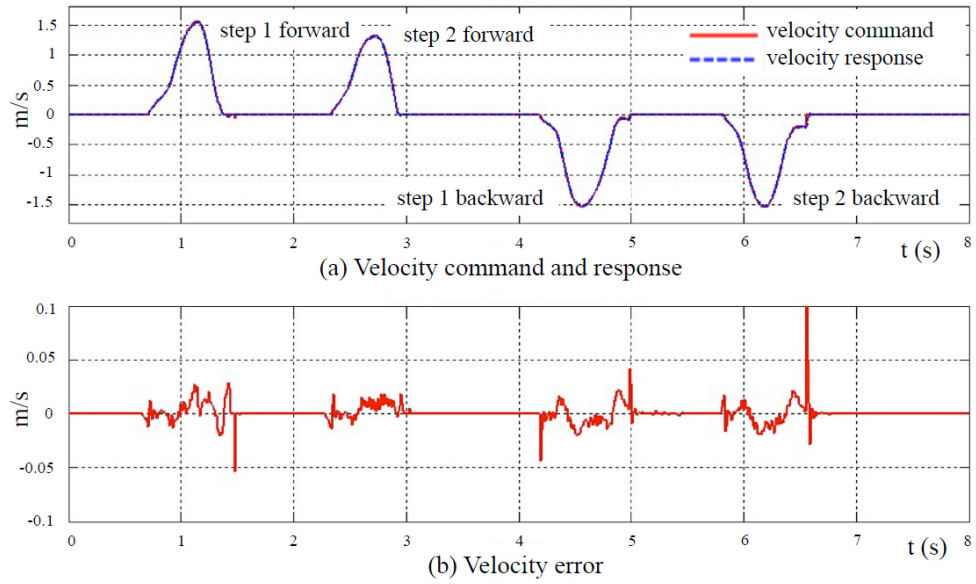

Fig. 5-11: Experimental response (velocity).

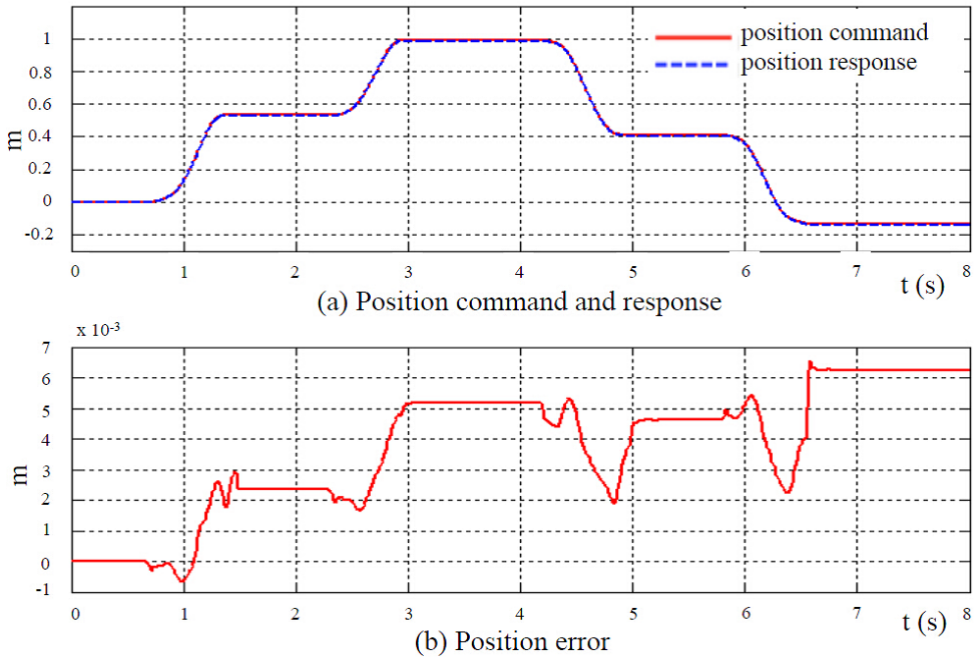

Fig. 5-12: Experimental response (position).

as a processor in this device. A 24V battery was used to supply power for the whole system. The total mass of this device is about 20 kg. It is stable and not easy to move by human force, therefore, as long as the elders to hold this device, it can help the elders with their walking well. The subject of this experiment is a 27 years old man. His height is 175cm and weight is about 60 Kg. In some

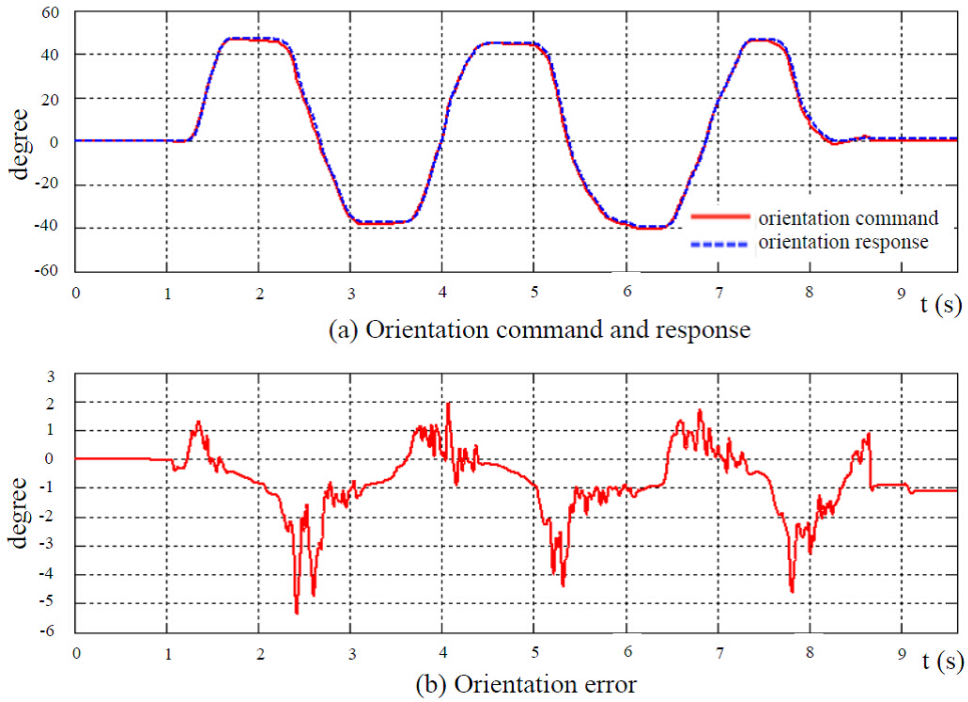

Fig. 5-13: Experimental response (orientation).

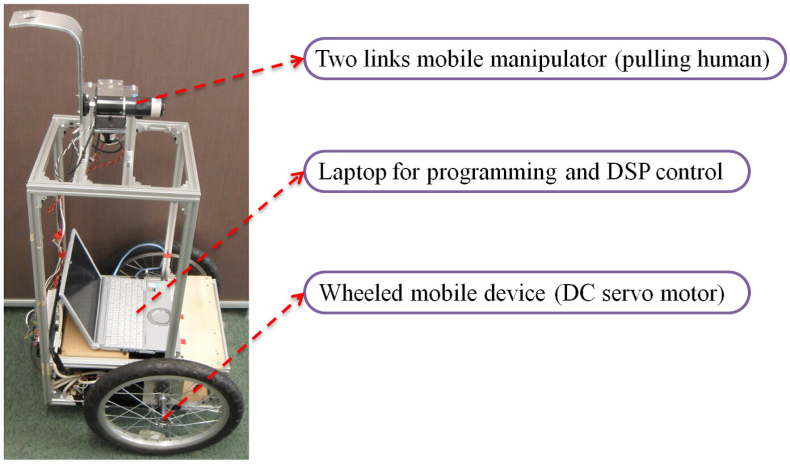

Fig. 5-14: Proposed device photograph.

experiments, the device had a small shake if the human walking fast. That is because of the inertial of device while device stopping and moving again and again. The mechanical structure can be changed, for example, move the two wheels to the backward, the shake problem can be eliminated. Because of the safety problem, the device orientation can only be adjusted in standing phase but not walking phase in this proposed approach. In general, the gait characteristics depend on a subject. Also, some elderly people walk slowly with shuffling and dragging steps. The proposed device is driven by the velocity and

orientation commands from the IMU sensor fixed on human foot. Since the steps are repeated in a cycle for everybody. All of the measurement data can be set to zero when the foot with IMU sensor stopping on the ground. Therefore, the proposed method can be applied to any type of gait.

5.6 Concluding Remarks

In this chapter, a novel walking assist device based on human motion was proposed. By experiments, the device moving together with human synchronously was realized. The manipulator is an optional part of this device. If it is removed away, the position and orientation errors can be compensated by labor power too. Finally, Fig. 5-15 shows a demonstration photograph of the proposed device in the 14^{th} Annual Keio Science and Technology Exhibition (KEIO TECHNO-MALL 2013). Although this research is just conceptual designed and implemented, it can provide a possible solution to help the elderly or patient walk more conveniently and easily in the future society.

Fig. 5-15: A demostration in the KEIO TECHNO-MALL 2013.

Chapter 6

Easy Moving and Self-Balancing Control

6.1 The Purpose of Design (Approach 3)

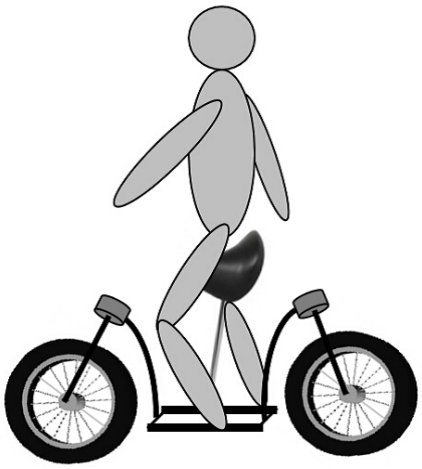

Fig. 6-1: Conceptual sketch of the handleless motorcycle.

After solving the problems such as preventing the elderly or patient from falling down and helping them walking, they also need a more faster and safe transportation method sometimes. Since the two-wheel electric motorcycle has good portability and flexibility, it has become popular in many countries nowadays. However, keeping the motorcycles balanced in full speed range, which is a valuable research in an accelerating ageing society, has not been thoroughly researched. In this study, a novel self-balancing electric motorcycle without the handlebar is put forward to cover this deficiency. By controlling the steering, the balance of the motorcycle can be kept with its wheels swaying. And the motorcycle direction

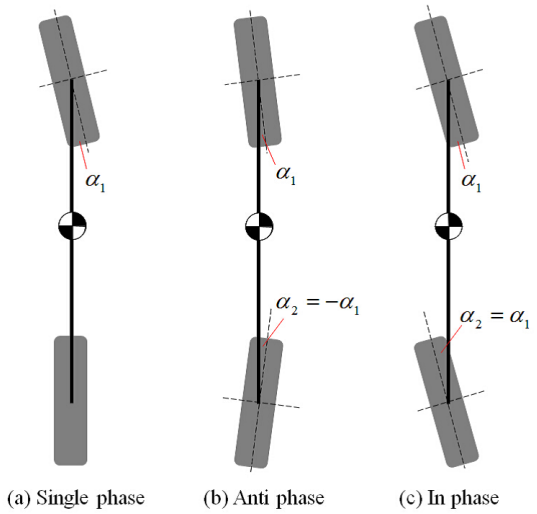

Fig. 6-2: Three kinds of steering modes.

can be controlled by the rider's body. Also, three different steering phases of handleless motorcycles were discussed. The difference of these three modes were shown by the comparison experiments. In order to achieve a full speed range self-balancing motorcycle system, two different modes were applied in zero/low speed and normal/high speed respectively. Fig. 6-1 shows a conceptual sketch of the proposed handleless motorcycle. The stability of them were analysed, and the final experimental results proved them as well.

6.2 Vehicle Modeling

In order to get a self-balancing electric motorcycle, the motorcycle dynamics modeling is described firstly. Fig. 6-2 shows three kinds of steering working modes. Fig. 6-2(a) is single phase mode (SPM) which means only the front steering is rotating; Fig. 6-2(b) is anti phase mode (APM), the front and rear steering rotate in the opposite direction; Fig. 6-2(c) is in phase mode (IPM), the front and rear steering rotate in the same direction. α_1 and α_2 are the steering angles of front and rear wheel respectively.

6.2.1 Dynamics of the SPM and APM

The dynamics of each mode are introduced in this subsection. Even the IPM cannot achieve a good self-balancing performance, its normal dynamics is discussed together. Another new dynamics for the IPM is introduced in the next subsections. Fig. 6-3 shows the geometry parameters of the electric motorcycle. r is radius of wheel and L is wheelbase. β is the angle of steering axis. Assuming the center

of mass (CoM) of the motorcycle is on the middle of wheelbase, thus the distance from CoM to wheel in vertical line is $L/2$. h is the height of CoM, l is the distance between ground contact point of wheels and the cross point of the steering axis extension line with ground.

If the motorcycle runs with constant steering angles and constant speed, the trajectory is a circular

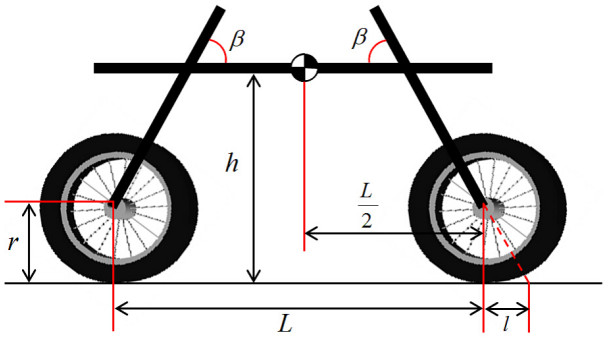

Fig. 6-3: Motorcycle modeling.

orbit. Fig. 6-4 shows the top view of the motorcycle in the world coordinates. R is radius of curvature around center of P_1 or P_2. φ_1 or φ_2 is the angle of motorcycle motion at CoM. The geometry of motorcycle can be calculated by the following equations,

$$R_2 \tan(\varphi_1) = \frac{L}{2} \tag{6.1}$$

$$R_2 \tan(\alpha_1) = L \tag{6.2}$$

$$R \sin(\varphi_1) = \frac{L}{2} \tag{6.3}$$

If the steering angle α_1 and CoM motion angle φ_1 are small, it can be linearized as $\tan(\varphi_1) \approx \varphi_1$, $\tan(\alpha_1) \approx \alpha_1$ and $\sin(\varphi_1) \approx \varphi_1$. In the SPM, α_2 is equal to zero. Denote φ is the direction angle of CoM, then $\varphi = \varphi_1 + \varphi_2$. Therefore, the relationship between α_1 and φ is [46],

$$\varphi = \varphi_1 \approx \frac{\alpha_1}{2} \tag{6.4}$$

$$R \approx \frac{L}{\alpha_1} \tag{6.5}$$

In the APM, α_2 is equal to minus α_1. The relationship between α_1 and φ is,

$$\varphi \approx \alpha_1 = -\alpha_2 \tag{6.6}$$

$$R \approx \frac{L}{2\alpha_1} \tag{6.7}$$

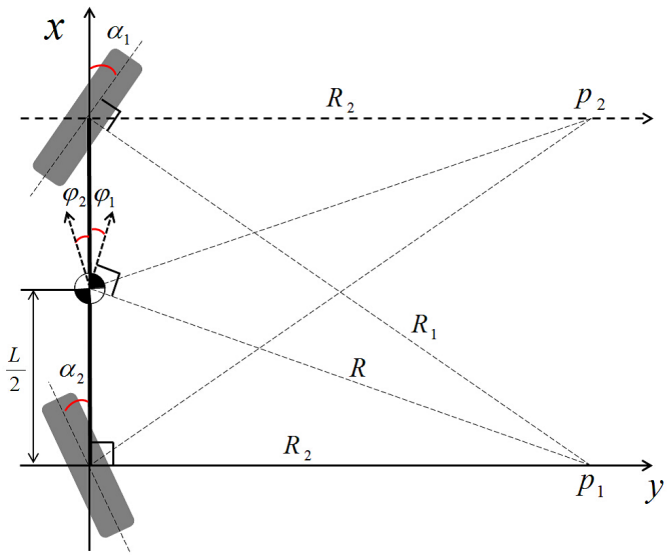

Fig. 6-4: Top view in the world coordinates.

In the IPM, α_2 is equal to α_1. This case is similar to Segway. The direction angle of CoM does not depend on α_1 or α_2 anymore. But φ depends on the different speed of the front and rear wheels.

Fig. 6-5 shows the rear view of the motorcycle with zero steering angles. θ is the camber angle which means the inclination angle of the motorcycle. F is composite force of centrifugal force F_o and steering rotation force F_r.

$$F = F_o + F_r \tag{6.8}$$

Denote the motorcycle moving velocity is v and the total mass is m. For the SPM,

$$F_o = \frac{mv^2}{R} \approx \frac{mv^2\alpha_1}{L} \tag{6.9}$$

And for the APM,

$$F_o \approx \frac{2mv^2\alpha_1}{L} \tag{6.10}$$

For the IPM, in this study, both of the front and rear wheels are designed as the same speed. Thus its centrifugal force is equal to zero. If the steering axis angle β is equal to 90^0, F_r of the SPM can be found as [46],

$$F_r = m(\frac{v}{2}\frac{d\alpha_1}{dt}) \tag{6.11}$$

For the APM, because the two steerings effect have the same direction,

$$F_r = m\frac{vd\alpha_1}{dt} \tag{6.12}$$

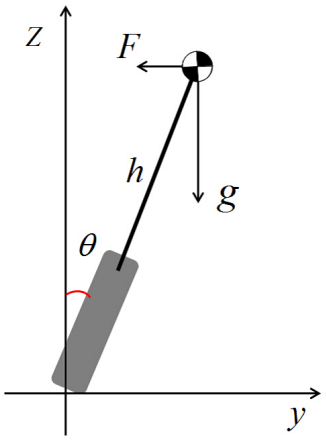

Fig. 6-5: Rear view of a naive motorcycle (both front and rear steering angles are zero).

For the IPM, two steerings effect have the opposite direction, then F is equal to zero. From the Fig. 6-5, the dynamics of the motorcycle can be found by using the Newton's second.

$$mgh\sin\theta - Fh\cos\theta = J\ddot{\theta} \tag{6.13}$$

Assuming the camber angle θ is small, then $\sin\theta \approx \theta$ and $\cos\theta \approx 1$, the dynamics equation can be linearized as,

$$mgh\theta - Fh = J\ddot{\theta} \tag{6.14}$$

where J denotes the moment of inertia of the motorcycle body with respect to the x axis. Substitute the force F, then for the SPM,

$$J\ddot{\theta} - mgh\theta = -\frac{mhv^2\alpha_1}{L} - \frac{mhv\dot{\alpha}_1}{2} \tag{6.15}$$

For the APM,

$$J\ddot{\theta} - mgh\theta = -\frac{2mhv^2\alpha_1}{L} - mhv\dot{\alpha}_1 \tag{6.16}$$

For the IPM,

$$J\ddot{\theta} = mgh\theta \tag{6.17}$$

However, the steering axis angle β is not equal to 90^0. Thus the design of the front fork or rear fork has a major impact on motorcycle dynamics. For the SPM, the steering angle influences the camber angle.

$$\theta_f = \theta - \alpha_1\cos\beta \tag{6.18}$$

and the effective front fork angle is,

$$\alpha_{1f} = \alpha_1\sin\beta \tag{6.19}$$

A new torque is generated by shifting the CoM while the steering is rotating.

$$\tau_f = \frac{-mgl\sin\beta}{2}\alpha_1 \tag{6.20}$$

Then the final dynamics for the SPM is,

$$J\ddot{\theta} - mgh\theta = -\frac{m(hv^2 - \frac{L}{2}gl)\sin\beta}{L}\alpha_1 - \frac{mhv\sin\beta}{2}\dot{\alpha}_1 \tag{6.21}$$

For the APM, the two steerings generate the new torque in the same direction, thus,

$$\tau_f = -mgl\alpha_1\sin\beta \tag{6.22}$$

$$J\ddot{\theta} - mgh\theta = \frac{m(Lgl - 2hv^2)\sin\beta}{L}\alpha_1 - (mhv\sin\beta)\dot{\alpha}_1 \tag{6.23}$$

For the IPM, the two steerings generate the new torque in the opposite direction, thus τ_f is equal to zero.

6.2.2 Kinematics of the IPM

The IPM can make the motorcycle keeping self-balancing even when it stops. Fig. 6-6 shows the IPM modeling of the motorcycle. ϕ is the motorcycle orientation and $W = L\sin\alpha_1 = L\sin\alpha_2$ is the distance of the two wheels. d is the motorcycle straight moving position. θ_f and θ_r are the rotate angles of front and rear wheels respectively. The IPM is similar to the Segway or two-wheel wheelchair. Thus it cannot move lateral direction. Assuming that both front and rear wheels do not slip, then the constraints condition are,

$$\dot{x}\sin\phi - \dot{y}\cos\phi = 0 \tag{6.24}$$

$$\dot{x}\cos\phi + \dot{y}\sin\phi + \frac{L\sin\alpha_1}{2}\dot{\phi} = r\dot{\theta_f} \tag{6.25}$$

$$\dot{x}\cos\phi + \dot{y}\sin\phi - \frac{L\sin\alpha_1}{2}\dot{\phi} = r\dot{\theta_r} \tag{6.26}$$

And the IPM moving velocity $\dot{d}$ and angular velocity $\dot{\phi}$ are obtained as,

$$\dot{d} = \frac{r}{2}(\dot{\theta}_f + \dot{\theta}_r) \tag{6.27}$$

$$\dot{\phi} = \frac{r}{L\sin\alpha_1}(\dot{\theta}_f - \dot{\theta}_r) \tag{6.28}$$

Therefore, kinematics of the IPM obtained as,

$$\begin{bmatrix} \dot{\theta} \\ \dot{d} \\ \dot{\phi} \end{bmatrix} = \begin{bmatrix} 1 & 0 & 0 \\ 0 & \frac{r}{2} & \frac{r}{2} \\ 0 & \frac{r}{L\sin\alpha_1} & -\frac{r}{L\sin\alpha_1} \end{bmatrix} \begin{bmatrix} \dot{\theta} \\ \dot{\theta}_f \\ \dot{\theta}_r \end{bmatrix} = \boldsymbol{J}\dot{\boldsymbol{q}} \tag{6.29}$$

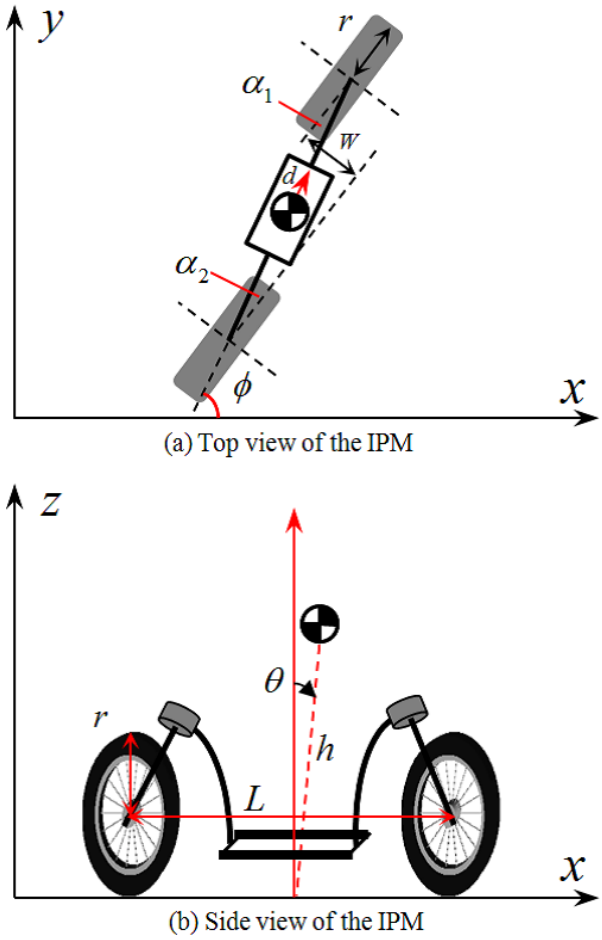

(a) Top view of the IPM

(b) Side view of the IPM

Fig. 6-6: IPM modeling.

And the inverse kinematics is,

$$\begin{bmatrix} \dot{\theta} \\ \dot{\theta}_f \\ \dot{\theta}_r \end{bmatrix} = \begin{bmatrix} 1 & 0 & 0 \\ 0 & \frac{1}{r} & \frac{L\sin\alpha_1}{2r} \\ 0 & \frac{1}{r} & -\frac{L\sin\alpha_1}{2r} \end{bmatrix} \begin{bmatrix} \dot{\theta} \\ \dot{d} \\ \dot{\phi} \end{bmatrix} = \boldsymbol{J}^{-1}\dot{\boldsymbol{X}} \tag{6.30}$$

where, r is wheel radius and L is wheelbase. θ is the motorcycle camber angle (roll angle).

6.2.3 Dynamics of the IPM

Denote $\boldsymbol{q} = [\theta, \theta_f, \theta_r]^T$ and $\boldsymbol{\tau} = [\tau_\theta, \tau_{\theta_f}, \tau_{\theta_r}]^T$. Dynamics of the IPM is obtained by solving Lagrange equation.

$$\boldsymbol{\tau} = \frac{d}{dt}\frac{\partial L}{\partial \dot{\boldsymbol{q}}} - \frac{\partial L}{\partial \boldsymbol{q}}. \tag{6.31}$$

Denote $\boldsymbol{M}$, $\boldsymbol{H}$, $\boldsymbol{G}$ are the inertia, the centrifugal and coriolis force, and the gravity matrices, respectively. Then the dynamics is,

$$\boldsymbol{\tau} = \boldsymbol{M}(\boldsymbol{q})\ddot{\boldsymbol{q}} + \boldsymbol{H}(\boldsymbol{q}, \dot{\boldsymbol{q}}) + \boldsymbol{G}(\boldsymbol{q}) \tag{6.32}$$

$$\boldsymbol{M} = \begin{bmatrix} M_{uu} & M_{ua} & M_{ua} \\ M_{ua} & M_{ff} & M_{fr} \\ M_{ua} & M_{fr} & M_{rr} \end{bmatrix} \tag{6.33}$$

$$\boldsymbol{H} = \begin{bmatrix} H_u \\ H_f \\ H_r \end{bmatrix}, \boldsymbol{G} = \begin{bmatrix} G_u \\ G_f \\ G_r \end{bmatrix} \tag{6.34}$$

where,

$$\begin{aligned}
M_{uu} &= m_b h^2 \\
M_{ua} &= \frac{m_b}{2} hr\cos\theta \\
M_{ff} &= \frac{(m_w + m_b)\, r^2}{4} + J_w + \frac{r^2[J + m_b(h\sin\theta)^2]}{(L\sin\alpha_1)^2} \\
M_{fr} &= \frac{(m_w + m_b)\, r^2}{4} - \frac{r^2[J + m_b(h\sin\theta)^2]}{(L\sin\alpha_1)^2} \\
M_{rr} &= M_{ff} \\
H_u &= -\frac{m_b r^2 h^2}{(L\sin\alpha_1)^2}\sin\theta\cos\theta(\dot{\theta}_f - \dot{\theta}_r)^2 \\
H_f &= \frac{2m_b r^2 h^2}{(L\sin\alpha_1)^2}\sin\theta\cos\theta(\dot{\theta}_f - \dot{\theta}_r)\theta - \frac{m_b hr}{2}\theta^2\sin\theta \\
H_r &= -\frac{2m_b r^2 h^2}{(L\sin\alpha_1)^2}\sin\theta\cos\theta(\dot{\theta}_f - \dot{\theta}_r)\theta - \frac{m_b hr}{2}\theta^2\sin\theta \\
G_u &= -m_b g h\sin\theta \\
G_f &= 0 \\
G_r &= 0
\end{aligned}$$

where, m_b and m_w are the wheelbase and wheel mass respectively. In this study, only straight motion of the IPM is considered, therefore,

$$\tau_w = \tau_f + \tau_r \tag{6.35}$$

$$\theta_w = \theta_f = \theta_r \tag{6.36}$$

where, $\boldsymbol{\tau} = [0, \tau_w]^T$ is the input torque, then the new dynamics is,

$$\boldsymbol{M} = \begin{bmatrix} M_{uu} & M_{ua} \\ M_{ua} & M_{aa} \end{bmatrix} \tag{6.37}$$

$$\boldsymbol{H} = \begin{bmatrix} H_u \\ H_a \end{bmatrix}, \boldsymbol{G} = \begin{bmatrix} G_u \\ G_a \end{bmatrix} \tag{6.38}$$

where,

$$\begin{aligned} M_{uu} &= m_b h^2 \\ M_{ua} &= m_b h r \cos\theta \\ M_{aa} &= 2J_w + \frac{(m_w + m_b)}{2} r^2 + 2m_b \left(\frac{rh \sin\theta}{L \sin\alpha_1} \right)^2 \\ H_u &= 0 \\ H_a &= -\frac{m_b h r}{2} \dot{\theta}^2 \sin\theta \\ G_u &= -m_b h g \sin\theta \\ G_a &= 0 \end{aligned}$$

It indicates that the inertia term M_{aa} depends on the steering angle α_1. For linearization, the nominal inertia matrix is,

$$\boldsymbol{M_n} = \begin{bmatrix} M_{nuu} & M_{nua} \\ M_{nua} & M_{naa} \end{bmatrix} \tag{6.39}$$

where,

$$\begin{aligned} M_{nuu} &= m_b h^2 \\ M_{nua} &= m_b h r \\ M_{naa} &= 2J_w + \frac{(m_w + m_b)}{2} r^2 \end{aligned}$$

6.2.4 SCOB of the IPM

Disturbance observer is widely applied in robotic control [90] [91] [92]. Based on disturbance observer, in this subsection, SCOB for the IPM is introduced. The motion equation of camber (roll) angle

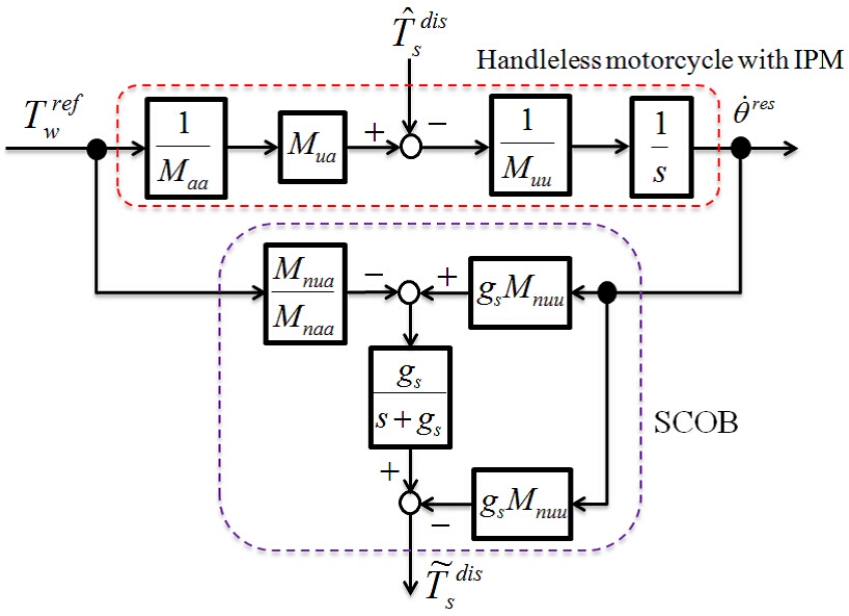

Fig. 6-7: Synthesized camber angle disturbance observer.

and wheel angle are given as eq. (6.40) and eq. (6.41). T_c^{dis} is the camber angle disturbance and T_w^{dis} is the wheel angle disturbance.

$$M_{uu}\ddot{\theta}^{res} + M_{ua}\ddot{\theta}_w^{res} + G_u + H_u + T_c^{dis} = 0 \tag{6.40}$$

$$M_{ua}\ddot{\theta}^{res} + M_{aa}\ddot{\theta}_w^{res} + H_a + T_w^{dis} = T_w^{ref} \tag{6.41}$$

By utilizing the nominal inertia matrix, and synthesizing each disturbance, then,

$$M_{nuu}\ddot{\theta}^{res} + M_{nua}\ddot{\theta}_w^{res} = -\hat{T}_c^{dis} \tag{6.42}$$

$$M_{nua}\ddot{\theta}^{res} + M_{naa}\ddot{\theta}_w^{res} = T_w^{ref} - \hat{T}_w^{dis} \tag{6.43}$$

Define wheel angle disturbance containing camber angle interaction torque, therefore,

$$M_{naa}\ddot{\theta}_w^{res} = T_w^{ref} - \hat{T}_w^{dis} \tag{6.44}$$

Substituting eq. (6.44), eq. (6.42) becomes,

$$M_{nuu}\ddot{\theta}^{res} + \frac{M_{nua}}{M_{naa}}T_w^{ref} = -\left(-\frac{M_{nua}}{M_{naa}}\hat{T}_w^{dis} + \hat{T}_c^{dis}\right) \tag{6.45}$$

Regarding right side equation as synthesized camber angle disturbance, then,

$$M_{nuu}\ddot{\theta}^{res} + \frac{M_{nua}}{M_{naa}}T_w^{ref} = -\hat{T}_s^{dis} \tag{6.46}$$

where $\hat{T}_s^{dis}$ is the synthesized camber angle disturbance. SCOB estimates the synthesized camber angle disturbance $\hat{T}_s^{dis}$ by using camber angle acceleration and wheel torque reference. But the IMU sensor measures the camber angle velocity. Therefore,

$$\begin{aligned} \tilde{T}_s^{dis} &= -\frac{g_s}{s+g_s}\left(\frac{M_{nua}}{M_{naa}}T_w^{ref} - M_{nuu}g_s\dot{\theta}^{res}\right) \\ &- M_{nuu}g_s\dot{\theta}^{res} \end{aligned} \tag{6.47}$$

where g_s is cut off frequency for pseudo differentiator. $\tilde{T}_s^{dis}$ contains camber angle disturbance and wheel angle disturbance. Fig. 6-7 shows the block diagram of SCOB.

6.3 Controller Design

For the SPM, $\alpha_2 = 0$ and α_1 is controlled by steering motor. For the APM, $\alpha_1 = -\alpha_2$, It means that the front and rear steerings are rotating in the reverse motion. If the motorcycle moving speed is not very high and the steering angle is small, it is assumed that this linearized model is enough. From eq. (6.23), the camber angle θ depends on the steering angle α_1 or α_2. Denote $\alpha = |\alpha_1|$, the desired steering angle α_d can be given by,

$$\alpha_d = K_m(\theta_d - \theta) + K_d(0 - \dot{\theta}). \tag{6.48}$$

where, K_m and K_d are the PD gains respectively. Then the steering acceleration reference $\ddot{\alpha}^{ref}$ is determined by,

$$\ddot{\alpha}^{ref} = \ddot{\alpha}_d + K_n(\dot{\alpha}_d - \dot{\alpha}) + K_a(\alpha_d - \alpha). \tag{6.49}$$

where, K_n and K_a are the rotate angle velocity and rotate angle gains respectively. Fig. 6-8 shows posture control block diagram for the moving self-balancing electric motorcycle.

Consider about the transfer function for the SPM from its final dynamics eq. (6.21),

$$G_s = \frac{\theta(s)}{\alpha_1(s)} = -\frac{\frac{mhv\sin\beta}{2}s + \frac{m(hv^2 - Lgl/2)\sin\beta}{L}}{Js^2 - mgh} \tag{6.50}$$

It is an unstable system. If $v < \sqrt{Lgl/h}$, it has one pole and one zero in the right-half plane. Such a system is not easy to control robustly when the pole and zero are too close. But the problem with right-zeros can be eliminated by introducing active control [46]. If there is a human rides on the motorcycle, she/he must produces an active force on it. Denote the external force applied to the CoM is τ_e and define the steering command as,

$$\alpha_1 = -k_i\tau_e + k_j\theta \tag{6.51}$$

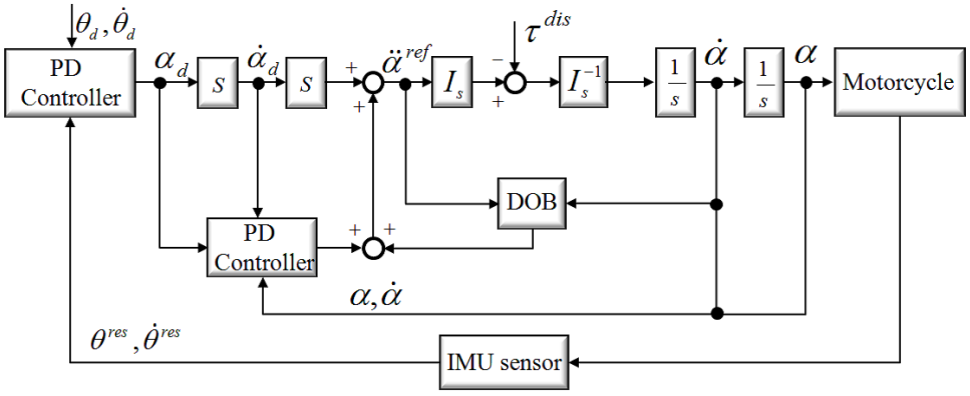

Fig. 6-8: Posture control for the SPM and APM.

where τ_e includes the rider's active force and fork or steering rotation effection force τ_f. In the experiments, the external force τ_e can be assumed as the product of camber acceleration and total mass. Both of camber acceleration and camber angle θ can be measured by the IMU sensor fixed on the motorcycle. Then it yields a new closed-loop system,

$$J\ddot{\theta} + k_j \frac{mhv\sin\beta}{2}\dot{\theta} + \left[k_j \frac{m(hv^2 - \frac{L}{2}gl)\sin\beta}{L} - mgh\right]\theta = k_i \frac{mhv\sin\beta}{2}\dot{\tau}_e + k_i \frac{m(hv^2 - \frac{L}{2}gl)\sin\beta}{L}\tau_e \tag{6.52}$$

the system is stable if $k_j > 0$ and

$$v > \sqrt{\left(\frac{1}{k_j \sin\beta} + \frac{l}{2h}\right) gL} \tag{6.53}$$

By the same principle, the new closed-loop system for the APM is,

$$J\ddot{\theta} + k_j mhv\sin\beta\dot{\theta} + \left[k_j \frac{m(2hv^2 - Lgl)\sin\beta}{L} - mgh\right]\theta = k_i mhv\sin\beta\dot{\tau}_e + k_i \frac{m(2hv^2 - Lgl)\sin\beta}{L}\tau_e \tag{6.54}$$

this system is stable if $k_j > 0$ and

$$v > \sqrt{\left(\frac{1}{2k_j \sin\beta} + \frac{l}{2h}\right) gL} \tag{6.55}$$

Fig. 6-9 shows the root locus by variable speed and k_j for eq. (6.52). k_i is a constant 0.1, k_j and v are variable values. It indicates that the stable system requires a bit larger value for k_j and v. That also means that the self-balancing with straight heading is possible. The motorcycle orientation is controlled by the

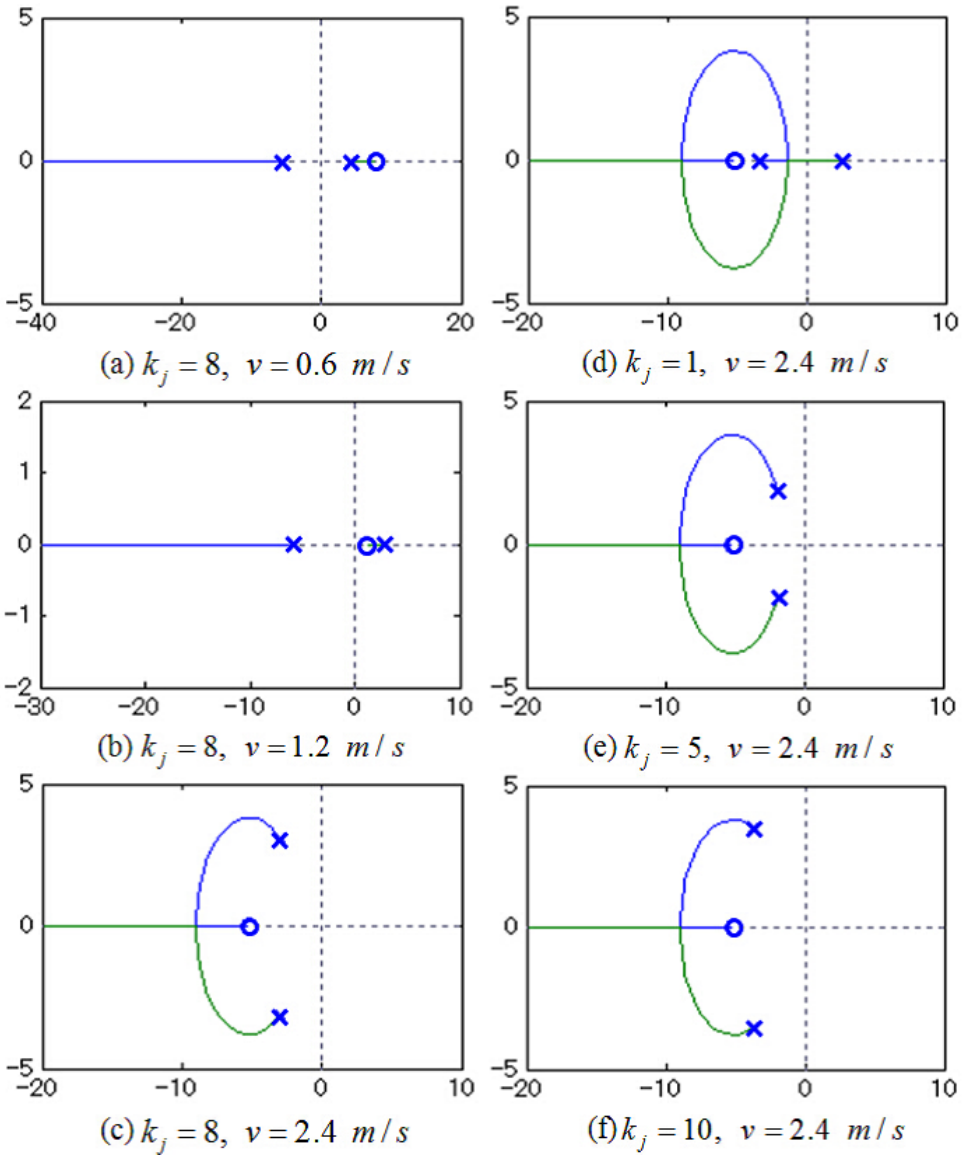

Fig. 6-9: Root locus by variable speed and k_j.

rider's body. It means that if the CoM is changed by human body, the orientation is forced to change. But after the human body recovers to the vertical state, self-balancing with straight heading works again. For the IPM, because the self-balancing method is different, its kinematics and dynamics are introduced in the following subsections.

6.3.1 Lyapunov-based control for the IPM

For the IPM, $\alpha_1 = \alpha_2$. It means that the front and rear steerings are rotating in the same motion. Similar to Segway, the self-balancing is achieved by wheels moving. In this section, Lyapunov-based

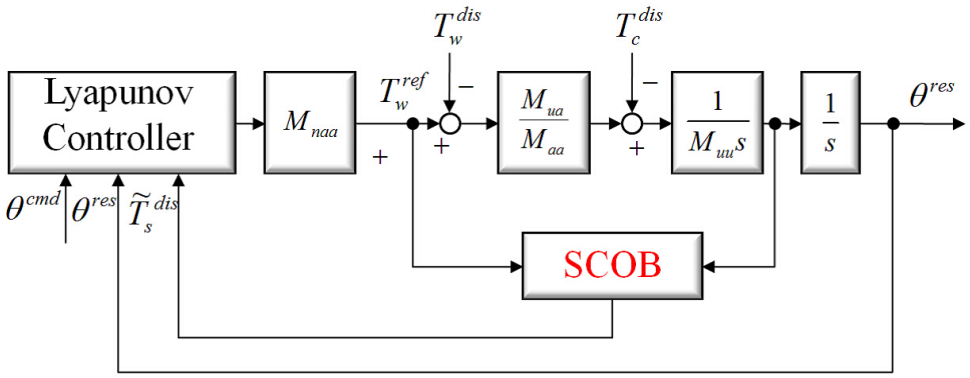

Fig. 6-10: Lyapunov control for the IPM.

control is used for the self-balancing stability. The candidate of Lyapunov function V is defined as,

$$V = \frac{1}{2}K_1(\theta^{cmd} - \theta^{res})^2 + \frac{1}{2}K_2(\dot{\theta}^{cmd} - \dot{\theta}^{res})^2 \tag{6.56}$$

By once derivation,

$$\begin{aligned} \dot{V} &= (\dot{\theta}^{cmd} - \dot{\theta}^{res}) \\ &\quad \left[K_1(\theta^{cmd} - \theta^{res}) + K_2(\ddot{\theta}^{cmd} - \ddot{\theta}^{res})\right] \end{aligned} \tag{6.57}$$

From the SCOB, eq. (6.57) is rewritten as,

$$\begin{aligned} \dot{V} = (\dot{\theta}^{cmd} - \dot{\theta}^{res}) \\ \left[K_1(\theta^{cmd} - \theta^{res}) + \ddot{\theta}^{cmd} - \frac{K_2}{M_{nuu}}(M_{nua}\ddot{\theta}_w^{ref} + \hat{T}_s^{dis})\right] \end{aligned} \tag{6.58}$$

The acceleration of translational distance $\ddot{\theta}_w^{ref}$ is determined as eq. (6.59) to make $\dot{V}$ semi-negative.

$$\begin{aligned} \ddot{\theta}_w^{ref} &= \frac{M_{nuu}}{M_{nua}}\left[\frac{K_1}{K_2}(\theta^{cmd} - \theta^{res}) + \frac{K_3}{K_2}(\dot{\theta}^{cmd} - \dot{\theta}^{res})\right] \\ &\quad -\frac{1}{M_{nua}}\tilde{T}_s^{dis} \\ &= \frac{M_{nuu}}{M_{nua}}\left[K_p(\theta^{cmd} - \theta^{res}) + K_v(\dot{\theta}^{cmd} - \dot{\theta}^{res})\right] \\ &\quad -\frac{1}{M_{nua}}\tilde{T}_s^{dis} \end{aligned} \tag{6.59}$$

where $\tilde{T}_s^{dis}$ is obtained by SCOB. If $\hat{T}_s^{dis}$ equals to $\tilde{T}_s^{dis}$, eq. (6.58) can be changed to eq. (6.60) by substituting eq. (6.59).

$$\dot{V} = -K_3\left(\dot{\theta}^{cmd} - \dot{\theta}^{res}\right)^2 \leq 0 \tag{6.60}$$

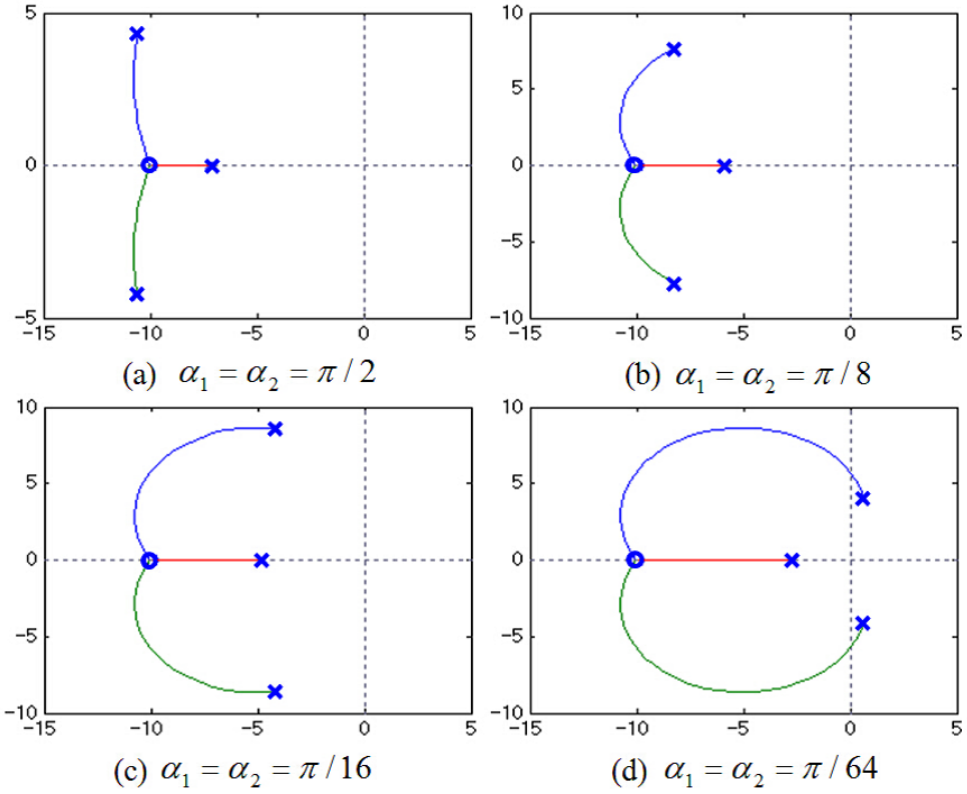

Fig. 6-11: Root locus by variable steering angle.

Then by Lasalle's theorem, $\theta_p \rightarrow 0, \dot{\theta}_p \rightarrow 0$ are guaranteed. Thus, the control input to stabilize wheelchair is decided as eq. (6.59). Fig. 6-10 shows Lyapunov control block diagram for the IPM. In the study, Lyapunov controller gain, K_1, K_2, K_2 are redesigned by K_p, K_v as following,

$$K_p = \frac{K_1}{K_2}$$
$$K_v = \frac{K_3}{K_2}$$

Because the inertia term M_{aa} is depending on the steering angle α_1, the stability is also depending on the steering angle α_1. The transfer function for the IPM system with SCOB is given by [61],

$$G_s = \frac{\theta^{res}}{\theta^{cmd}} = \frac{s^3 + B}{As^3 + B} \tag{6.61}$$

where,

$$A = \frac{M_{uu}M_{aa}M_{nua}}{M_{nuu}M_{naa}M_{ua}}$$
$$B = (K_v + g_s)s^2 + (K_p + K_v g_s)s + K_p g_s$$

Fig. 6-11 shows the root locus by varying steering angle for SCOB. In this root locus, $K_p = 100$, $K_v = 20$ and $g_s = 10$. It indicates that the IPM system becomes unstable if steering angle is small. If the steering angle is 90 degree, the IPM becomes Segway, and the stability is good. But if the steering angle is close to zero degree, the IPM becomes unstable systems.

6.4 Experiments

In this section, experiment procedures and results are explained. In order to compare with the performance of the three kinds of steering working modes, all of the three types (SPM, APM and IPM) are confirmed by the posture control firstly. After this comparison, the IPM is confirmed by Lyapunov control. Fig. 6-12 shows a experiment photograph of the real handleless electric motorcycle. An iBIS system which is a PC based DSP was used as a processor in this vehicle. A 24V battery was used to supply power for the whole system. An IMU sensor is fixed on the top of the motorcycle to measure the gyro (roll angular rate) , camber (roll) angle and yaw angle. Table 1 shows physical parameters of the motorcycle and actuators.

6.4.1 Experiment procedures

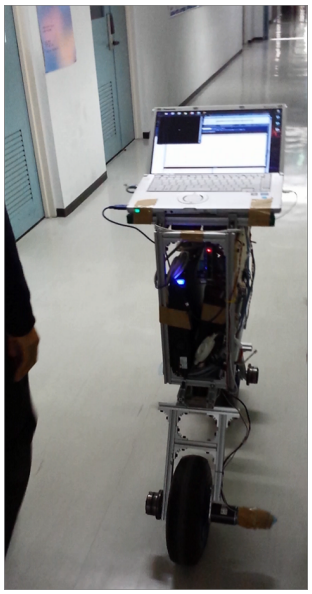

Fig. 6-12: Experiment photograph on a straight way.

(1). Applying the posture controller, implement the SPM, APM and IPM experiments respectively.

Table 6.1: Physical parameters of the motorcycle.

Name	Value
Wheel radius r [m]	0.13
Structure wheelbase L [m]	0.63
Distance l [m]	0.48
Steering axis angle β [^{0}]	30
CoM vertical position h [m]	0.8
Mass of the motorcycle body m_b [kg]	22.1
Mass of the motorcycle wheel m_w [kg]	1.5
Total mass of the motorcycle m [kg]	25.1
Maximum angel of the master θ_m [rad]	0.47
Normal speed of driving wheel ω [rpm]	60
Motorcycle normal moving speed v [m/s]	0.82
Rotary encoder resolution R_e [PPR]	400000
Gear reduction of motors G_r	100

The motorcycle moving speed v is a constant, and it is set as a normal value 1.47 km/h. A laptop is fixed on the top of the motorcycle, it can read and monitor the system data in real time. All experiments are implemented on a long passageway.

(2). In order to prove that the SPM stability with posture control is depending on variable moving speed, we implement the SPM experiments by variable speed. The moving speed is operated by the master. The maximum operation angle θ_m is 0.47 rad, and the corresponding speed is 0 km/h. The minimum master angle θ_m is 0 rad, and the corresponding speed is 2.94 km/h.

(3). To prove that the IPM stability with Lyapunov control is depending on variable steering angle, we implement the IPM experiments at zero speed by variable steering angle. The steering angle is operated by the master too. The operation range is from 0 rad to 0.47 rad. The steering angle is equal to minus angle of the master.

(4). When the motorcycle moves with normal or high speed ($v > 2.94$ km/h), we implement the experiments as the SPM with posture control. When the motorcycle stops or moves with slow speed ($v < 0.2$ km/h), we implement the experiments as the IPM with Lyapunov control. The master switching angle for Lyapunov control to posture control is 0.4 rad.

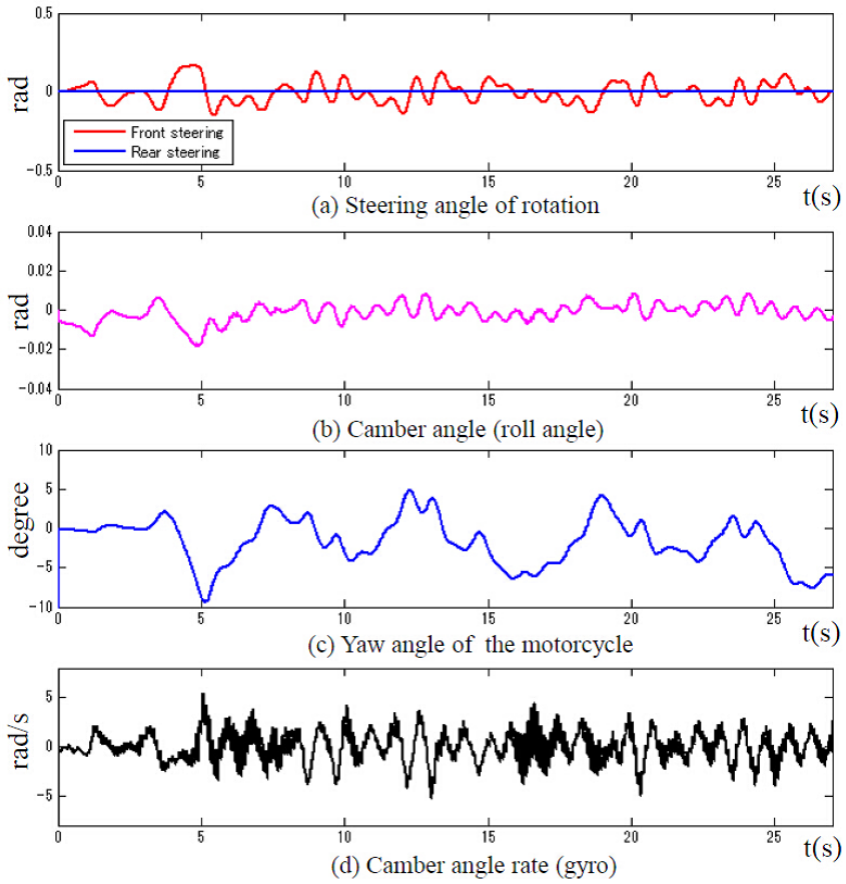

Fig. 6-13: The SPM performance on a straight way.

6.4.2 Experiment results

When the electric motorcycle runs at a high speed, it is more easy to keep self-balancing. However, if the electric motorcycle can keep self-balancing at a normal speed, the performance comparison is more meaningful. Therefore, in this study, the motorcycle runs as a normal speed (1.47 km/h). Fig. 6-13, Fig. 6-14 and Fig. 6-15 are the results of experiment procedure (1). Where, Fig.6-13 shows the SPM performance on a straight way. Fig. 6-13(a) indicates the angle of the front and rear steering rotation. They play a major role in keeping self-balancing. Fig. 6-13(b) shows the camber angle of the electric motorcycle body. It is the direct expression of self-balancing. Fig. 6-13(c) indicates the yaw angle of the motorcycle body. This is a parameter to measure the orientation when the motorcycle running on the straight way. Fig. 6-13(d) shows the camber angle rate. It is the angle rate command for the steering. Fig. 6-14 shows the IPM performance on the straight way. Fig. 6-14(a) and (b) indicate the steering rotation amplitude is bigger than the SPM, but the motorcycle body sway frequency is smaller than the

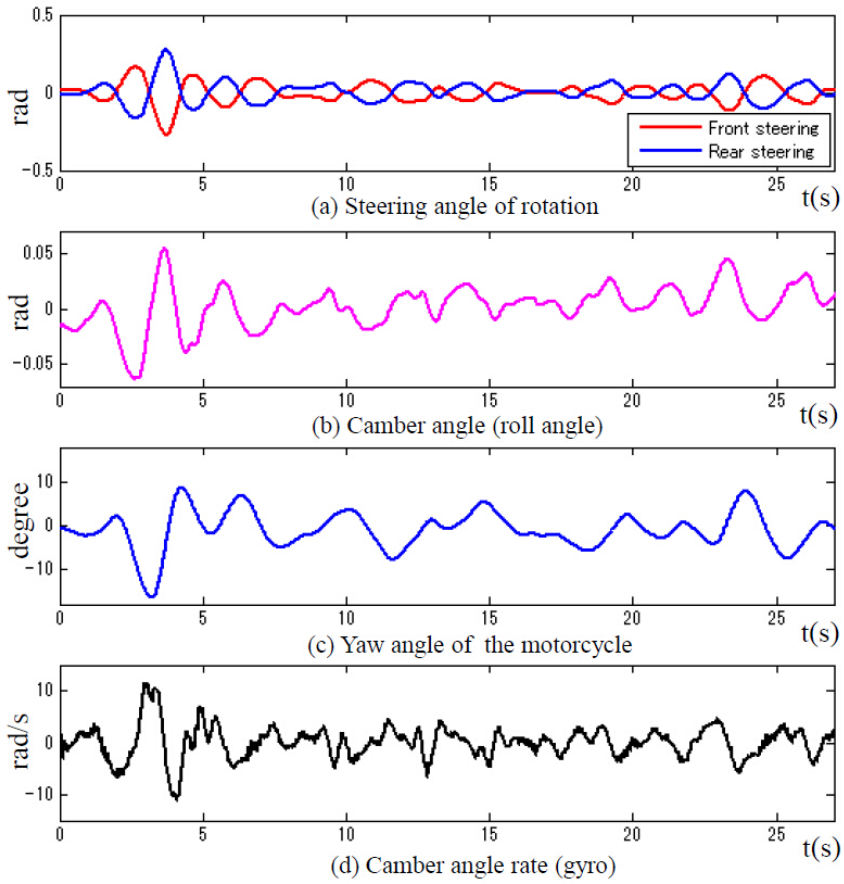

Fig. 6-14: The APM performance on a straight way.

SPM. Fig. 6-14(c) and (d) indicate the APM has a bigger yaw angle and camber angle rate than the SPM. Because the IPM is similar to Segway, if the experiment is only implemented by steering control, it is not easy to keep self-balancing. The results are shown in Fig. 6-15. It indicates that the IPM could not keep self-balancing after 10 seconds. And Fig. 6-15(c) shows the motorcycle orientation could not be changed during the moving. That is why the IPM cannot keep self-balancing for a longer time.

Based on the results of experiment procedure (1), we choose the SPM as the normal or high speed running mode for the motorcycle. Fig. 6-16 shows results of the SPM moving by variable speed of experiment procedure (2). The green shadow area is normal speed result. Fig. 6-16(a) indicates the master angle, front steering angle and rear steering angle. Fig. 6-16(b) and (c)show the camber angle and camber angle rate respectively. By changing the master angle, the motorcycle runs at different speed. When the motorcycle runs at a high speed, the swaying frequency becomes small but amplitude becomes bigger. The results show that the SPM can keep self-balancing at normal or high speed well. However, the SPM cannot keep self-balancing at zero or slow speed.

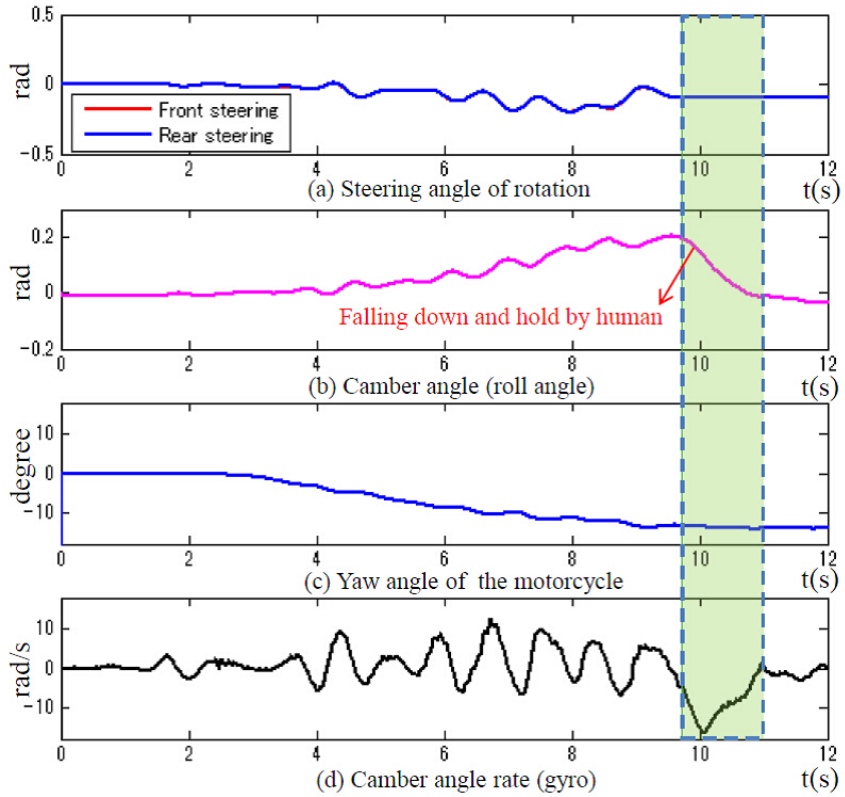

Fig. 6-15: The IPM performance without speed control on a straight way.

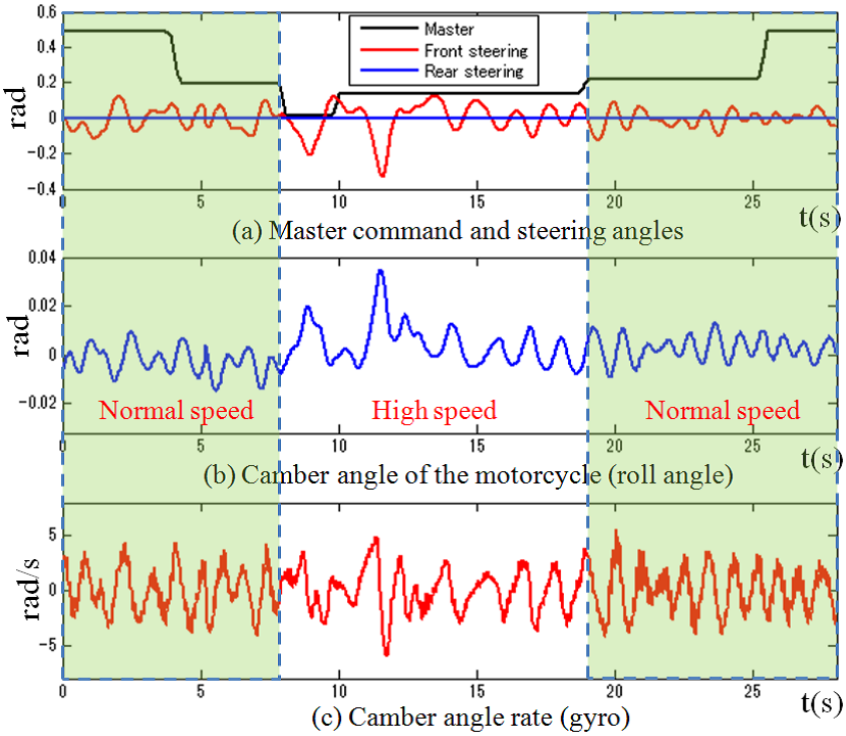

Fig. 6-16: The SPM runs by variable speed on a straight way.

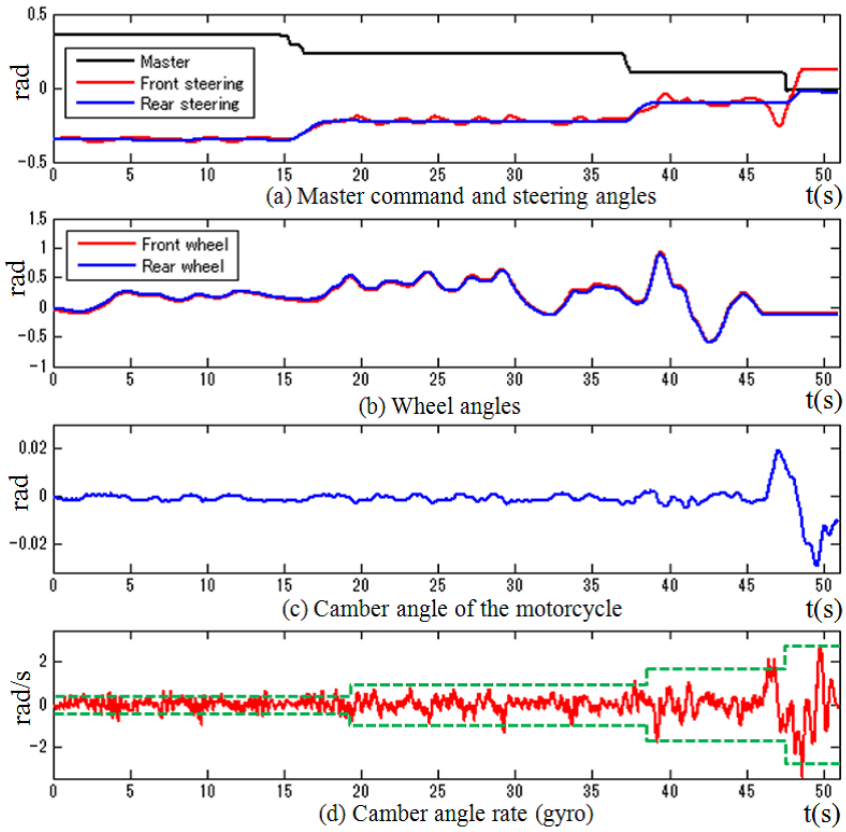

Fig. 6-17: The IPM with Lyapunov control stands by variable steering angle.

In order to achieve the self-balancing at zero or slow speed, we apply the IPM with Lyapunov control. Then results of experiment procedure (3) are shown in Fig. 6-17. For this stability testing, the motorcycle wheel motors are not controlled by the master. Only the SCOB controls the wheel motors. From 0 second to 15 seconds, the master angle is 0.47 rad and the steering angles α_1, α_2 are -0.47 rad. The IPM can stand well at zero speed. From 16 seconds to 37 seconds, the steering angles are -0.25 rad. The IPM can stand well at zero speed too, but Fig. 6-17(d) shows the amplitude of camber angle rate becoming bigger. From 38 seconds to 47 seconds, the steering angles are -0.12 rad. The IPM can stand at zero speed, but the amplitude of camber angle rate becoming bigger and bigger. After 48 seconds, the steering angles are close to 0 rad. The IPM cannot stand at zero speed easily anymore. This experiment proved the root locus by variable steering angle of Fig. 6-11.

Based on the SPM stability with normal or high speed and the IPM stability with zero or slow speed, we propose the final handleless electric motorcycle as Fig. 6-18. It combines the advantages of the SPM and IPM. The master controls the steering angles and motorcycle speed at the same time. When the motorcycle moves with normal or high speed, the SPM with posture controller is used. When it stops or

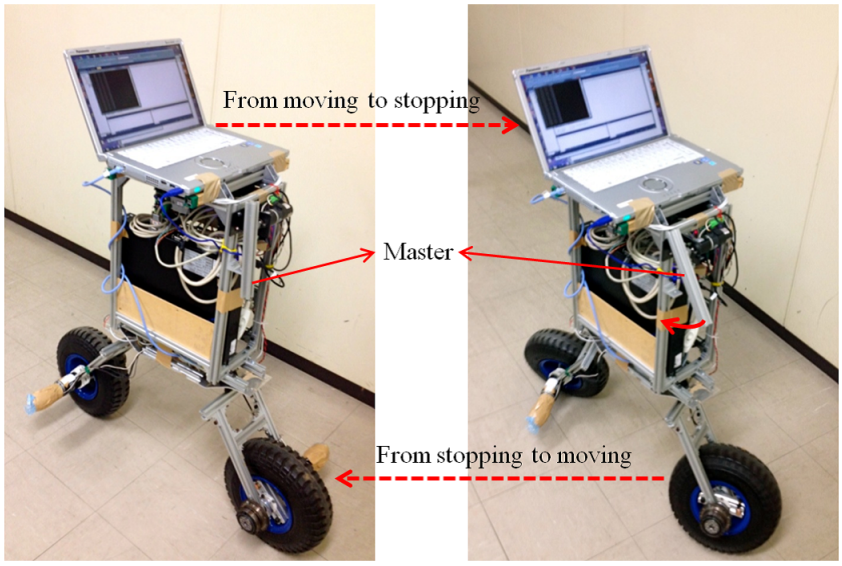

(a) Posture of normal/high speed (b) Posture of zero/low speed

Fig. 6-18: A photograph of the final handleless motorcycle.

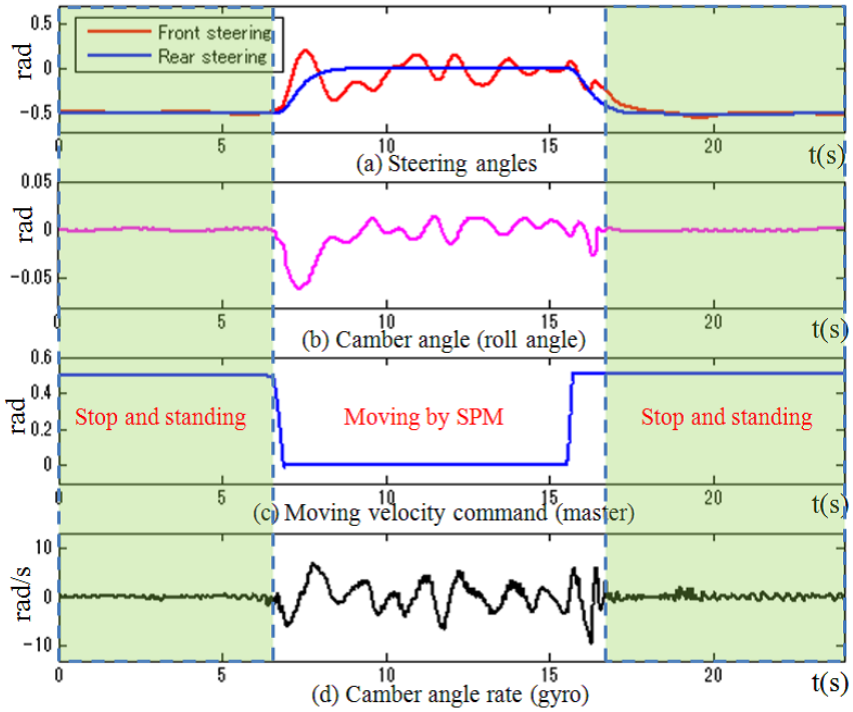

Fig. 6-19: Final and total results of the proposal.

moves with slow speed, the IPM with Lyapunov control is applied. Finally, the integrated and total experiment results are shown in Fig. 6-19. From 0 second to 7 seconds, the motorcycle keeps standing by the IPM with Lyapunov control. From 8 seconds to 16 seconds, the motorcycle moves at a normal speed by the SPM with posture control. After 17 seconds, the motorcycle stops and stands again. Fig. 6-19(b) shows camber angle data, it indicates that the motorcycle can keep self-balancing in full speed range.

6.5 Concluding Remarks

In the chapter, three kinds of steering working modes (SPM, APM and IPM) of the handleless electric motorcycle were introduced firstly. The comparison experiment results are also discussed. The SPM has the best self-balancing stability when the motorcycle moves with a speed. Its speed can be controlled by rider's feet in the practical application. The APM only has the fastest turning performance. The IPM is not easy to keep self-balancing without speed control. But the IPM with Lyapunov control has a good standing stability. Therefore, in the final handleless electric motorcycle, we combined the advantages of the SPM and IPM. In addition, because the orientation of motorcycle was controlled by rider's body, it is possible to get a stable electric motorcycle robot system without the handlebar in full speed range. Finally, Fig. 6-20 shows a demonstration photograph of the expected handleless motorcycle with a rider. Although this research is still relatively immature, it can provide a solution to help the elderly or patient move more conveniently and easily in the future society.

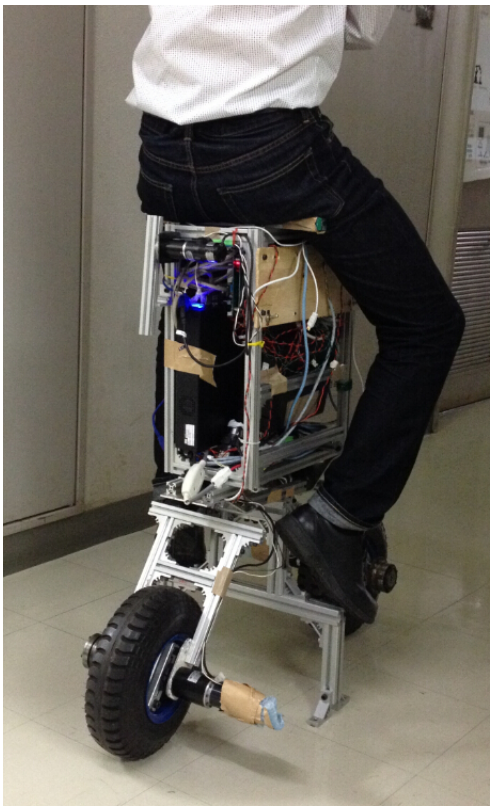

Fig. 6-20: A photograph of the expected handleless motorcycle with a rider.

Chapter 7

Conclusions

This chapter concludes the dissertation and provides a summary of the major results and contributions of this work. Also, a discussion of directions for future work is provided finally.

7.1 Summary

According to the aging population problem, this work presented three solutions to help the elderly or patient walk and move more conveniently and easily from three different aspects. From chapter 4 to chapter 6, the conceptual design and control of these walking and transportation assist devices were introduced. All of them are intended to help the elderly or patient walk or move independently. Different design objectives for the three solutions are summarized below.

- The multi-legged walking assist device (approach 1) focuses on preventing the elderly fall down and enhancing their walking ability, it is suitable for the elderly or patient who have very poor walking ability. The moving speed is the slowest correspondingly.

- The walking assist cart operated by human foot (approach 2) focuses on giving a hand to the elderly when they walking, it is suitable for the elderly or patient who have a better walking ability but cannot walk without walking assist devices. The device easily moves beside the user and coordinate with his or her steps, and moving speed is depend on the users' habits.

- The self-balancing two-wheel electric motorcycle (approach 3) focuses on providing a fast and safe transportation solution for the elderly or patient. It can keep self-balancing not only at high

speed but also at low and zero speed. It is suitable for the elderly or patient who have a better walking ability and want to move fast. Its moving speed is the fastest correspondingly.

Although these researches are still relatively immature, it can provide solutions to help the elderly or patient move more conveniently and easily in the future society. The major contributions of them is providing some novel ideas, designs and control methods to help the elderly or patient who want to walk or move conveniently and independently. In the field of man-machine cooperation control, considering human motion is a development trend. This is why the chapter 2 studied the human motion measurement method by IMU sensors firstly. The IMU sensor fixed on chest could not measure body moving motion well but it could easily measure human posture motion by Euler angles. Because Euler angles were obtained by the IMU sensor directly. The other IMU sensor fixed on foot could measure human walking motion well by filters and some gait recognition algorithms.

In order to control the proposed devices accurately and robustly, chapter 3 introduced the DOB, RTOB and SCOB detailedly. DOB was used in DC motor control to achieve high performance robust systems. It was applied in all proposed devices, since the actuators were DC motors. RTOB was utilized in torque/force sensorless control of manipulator systems. It was only applied in the approach 1. SCOB was designed for the inverted pendulum systems. It was suitable not only for the one-wheeled inverted pendulum system, but also for the self-balancing two-wheel electric motorcycle system. All of the observers were based on the disturbance compensation theory of DOB.

7.2 Directions for Future Works

Successful walking and transportation assistance systems have to increase the assist devices' safety and be acceptable for the user. A natural direction for the proposals is to focus on the elderly or patient acceptance issues. Therefore, more perfect functions, more safer and more practical systems are required. Specifically, for the multi-legged walking assist device (approach 1), two 3 DOF manipulators need to be considered. Then it is possible to consider about the other kinds of falling down motions. In addition, variable impedance should be designed to increase the performance, based on different cases. For the walking assist cart operated by human foot (approach 2), applying two IMU sensors to detect human walking motion is a solution of smooth moving of the device. And also, avoiding the problem of elders' falling down needs to be considered. For the self-balancing two-wheel electric motorcycle (approach 3), a seat may be fixed on the motorcycle, then it can be ridden by human. Considering the body effect of the

rider, another IMU sensor should be applied to measure the rider's posture motion. Also, a self-balancing of orientation controller should be studied.

In addition, from the general design, determining users' intent may also play a role in the human acceptance of walking and transportation assist devices. For example, due to the physical agility, if the elderly or patient brain tries to do some actions but their limbs could not work, the proposed devices should not assist this. One solution is including the brainwave control if the brainwave technology becomes mature enough in the future. There is a big researching value for future work in modern walking and transportation assist devices. These devices hold the potential of helping thousand of unattended elderly or patients in this more and more serious aging society.

References

[1] Homepage of National Institute of Population and Social Security Research
http://www.ipss.go.jp/ (accessed: May 1, 2015)

[2] Homepage of Ministry of Health, Labour and Welfare
http://www.mhlw.go.jp/ (accessed: May 1, 2015)

[3] Homepage of Health and Welfare Information Association
http://www.hcrjapan.org/ (accessed: May 1, 2015)

[4] Y. Ikeuchi, J. Ashihara, Y. Hiki, H. Kudoh and T. Noda, "Walking assist device with bodyweight support system", in *Proceedings of IEEE/RSJ International Conference on Intelligent Robots and Systems*, pp. 4073 – 4079, Oct. 2009.

[5] K. Yasuhara, K. Shimada, T. Koyama, T. Ido, K. Kikuchi, and Y. Endo, "Walking assist device with stride management system", *Honda R&D Technical Review*, Vol.21, No.2, pp. 54–62, Oct. 2009.

[6] Homepage of Honda Robotics
http://www.honda.co.jp/robotics/ (accessed: May 1, 2015)

[7] H. Herr, "Exoskeletons and orthoses: classification, design challenges and future directions", *Journal of Neuro Engineering and Rehabilitation*, vol. 6, no. 1, pp. 1–9, 2009.

[8] K. Yamawaki, R. Ariyasu, S. Kubota, H. Kawamoto, Y. Nakata, K. Kamibayashi, Y. Sankai, K. Eguchi, and N. Ochiai, "Application of robot suit HAL to gait rehabilitation of stroke patients: a case study", *Springer Berlin Heidelberg*, pp. 184–187, 2012.

[9] A. Tsukahara, Y. Hasegawa, and Y. Sankai, "Gait support for complete spinal cord injury patient by synchronized leg-swing with HAL", in *Proceedings of the 2011 IEEE/RSJ International Conference on Intelligent Robots and Systems (IROS2011)*, pp. 1737–1742, 2011.

[10] D. Matsuura, R. Inose, and Y. Takeda, "Motion control algorithm of walking assist machine using crutches to achieve variable gait style and step length", in *Proceedings of the International Workshop and Summer School on Medical and Service Robotics (MESROB2014)*, July, 2014.

[11] M. Higuchi, M. Ogata, S. Sato, and Y. Takeda, "Development of a walking assist machine using crutches (Composition and basic experiments)", *Journal of Mechanical Science and Technology*, vol. 24, no. 1, pp. 245–248, 2010.

[12] H. Yasuhisa, T. Iwano, and K. Kosuge, "Control of wearable walking helper on slope based on integration of acceleration and GRF information", in *Proceedings of 2008 IEEE/RSJ International Conference on Intelligent Robots and Systems*, pp. 3731–3736, 2008.

[13] C. Zhu and A. Kawamura, "Walking principle analysis for biped robot with ZMP concept, friction constraint, and inverted pendulum model", in *Proceedings of 2003 IEEE/RSJ International Conference on Intelligent Robots and Systems*, pp. 364–369, 2003.

[14] A. Suzumura and Y. Fujimoto, "Real-time motion generation and control systems for high wheel-legged robot mobility", *IEEE Trans. on Industrial Electronics*, vol. 61, no. 7, pp. 3648–3659, 2014.

[15] R. Annicchiarico, C. Barru, T. Benedico, F. Campana, U. Corts, and A. Mart'nez-Velasco, "The i-Walker: an intelligent pedestrian mobility aid", in *Proceedings of the 2008 conference on ECAI 2008: 18th European Conference on Artificial Intelligence*, pp. 708–712, 2008.

[16] M. Watanabe and T. Murakami, "Walker's motion based control of two-wheel mobile manipulator", in *Proceedings of the 13th International Workshop on Advanced Motion Control (AMC2012)*, pp. 1–6, 2012.

[17] N. Hata, and Y. Hori, "Stride width estimation and walking stabilization control for personal walking assist", in *Proceedings of the IEEJ Industry Applications Society Conference*, vol. 2, pp. 125–130, 2005.

[18] H. Kawamoto, S. Lee, S. Kanbe, and Y. Sankai, "Power assist method for HAL-3 using EMG-based feedback controller", in *Proceedings of IEEE International Conference on Systems, Man, and Cybernetics*, pp.1648–1653, 2003.

[19] K. Sagawa, Y. Satoh, and H. Inooka, "Non-restricted measurement of walking distance", in *Proceedings of IEEE International Conference on Systems, Man, and Cybernetics*, pp. 1847–1852, 2000.

[20] O. H. Madgwick, J. L. Harrison, and R. Vaidyanatha, "Estimation of IMU and MARG orientation using a gradient descent algorithm", in *Proceedings of IEEE International Conference on Rehabilitation Robotics (ICORR)*, pp. 1–7, 2011.

[21] A. M. Sabatini, C. Martelloni, S. Scapellato, and F. Cavallo, "Assessment of walking features from foot inertial sensing", *IEEE Transactions on Biomedical Engineering*, vol. 52, no. 3, pp. 486–494, 2005.

[22] F. Cavallo, A. M. Sabatini, and V. Genovese, "A step toward GPS/INS personal navigation systems: Real-time assessment of gait by foot inertial sensing", in *Proceedings of IEEE/RSJ International Conference on Intelligent Robots and Systems*, pp. 1187–1191, 2005.

[23] A. M. Sabatini, "Quaternion-based extended Kalman filter for determining orientation by inertial and magnetic sensing", *IEEE Transactions on Biomedical Engineering*, vol. 53, no. 7, pp. 1346–1356, 2006.

[24] E. Foxlin, "Pedestrian tracking with shoe-mounted inertial sensors", *IEEE Computer Graphics and Applications*, vol. 25, no. 6, pp. 38–46, 2005.

[25] O. Bebek, M. A. Suster, S. Rajgopal, M. J. Fu, X. Huang, M. C. Cavusoglu, D. J. Young, M. Mehregany, A. J. van den Bogert, and C. H. Mastrangelo, "Personal navigation via high-resolution gait-corrected inertial measurement units", *IEEE Transactions on Instrumentation and Measurement*, vol. 59, no. 11, pp. 3018–3027, 2010.

[26] C. Zhou, J. Downey, D. Stancil, and T. Mukherjee, "A low-power shoe-embedded radar for aiding pedestrian inertial navigation", *IEEE Transactions on Microwave Theory and Techniques*, vol. 58, no. 10, pp. 2521–2528, 2010.

[27] I. P. I. Pappas, M. R. Popovic, T. Keller, V. Dietz, and M. Morari, "A reliable gait phase detection system", *IEEE Transactions on Neural Systems and Rehabilitation Engineering*, vol. 9, no. 2, pp. 113–125, 2001.

[28] Y. W. Guo, B. Y. Huang, G. R. Zhao, B. Q. Liu, and L. Wang, "Analysis of filtering methods for 3D acceleration signals in body sensor network", in *Proceedings of the International Symposium on Bioelectronics and Bioinformatics (ISBB)*, pp. 263–266, 2011.

[29] C. Y. Lee, and J. J. Lee, "Estimation of walking behavior using accelerometers in gait rehabilitation", *International Journal of Human-Friendly Welfare Robotic Systems*, vol. 3, no. 2, pp. 32–35, 2002.

[30] X. Yun, J. Calusdian, E. R. Bachmann, and R. B. McGhee, "Estimation of human foot motion during normal walking using inertial and magnetic sensor measurements", *IEEE Transactions on Instrumentation and Measurement*, vol. 61, no. 7, pp. 2059–2072, 2012.

[31] X. Yun, E. R. Bachmann, H. M. IV, and J. Calusdian, "Self-contained position tracking of human movement using small inertial/magnetic sensor modules", in *Proceedings of IEEE International Conference on Robotics and Automation*, pp. 2526–2533, 2007.

[32] S. W. Lee and K. Mase, "Activity and location recognition using wearable sensors", *IEEE Pervasive Computing*, vol. 1, no. 3, pp. 24–32, 2002.

[33] C. Randell, C. Djiallis, and H. Muller, "Personal position measurement using dead reckoning", in *Proceedings of the 7th IEEE International Symposium on Wearable Computers*, pp. 166–173, 2003.

[34] X. Yun and E. R. Bachmann, "Design, implementation, and experimental results of a quaternion-based Kalman filter for human body motion tracking", *IEEE Transactions on Robotics*, vol. 22, no. 6, pp. 1216–1227, 2006.

[35] A. V. Beznos, A.M. Formal'sky, E. V. Gurfinkel, D. N. Jicharev, A. V. Lensky, K. V.Savitsky, and L.S. Tchesalin, "Control of autonomous motion of two-wheel bicycle with gyroscopic stabilisation", in *Proceedings of International Conference on Robotics and Automation*, pp. 2670–2675, 1998.

[36] B. T. Thanh and M. Parnichkun, "Balancing control of bicyrobo by particle swarm optimization-based structure-specified mixed $H_2/H\infty$ control", *International Journal of Advanced Robotic Systems*, vol. 5, no. 4, pp. 395–402, 2008.

[37] M. Yamakita and A. Utano, "Automatic control of bicycle with a balancer", in *Proceedings of the International Conference on Advanced Intelligent Mechatronics*, pp. 1245–1249, 2005.

[38] A. Murayama and M. Yamakita, "Development of autonomous bike robot with balancer", in *Proceedings of the SICE Annual Conference*, pp. 1048–1052, 2007.

[39] H. Niki and T. Murakami, "An approach to self stabilization of bicycle motion by handle controller", *IEEJ Transactions on Industry Applications*, vol. 125, no. 8, pp. 779–785, 2005.

[40] Y. Tanaka and T. Murakami, "Self sustaining bicycle robot with steering controller", in *Proceedings of IEEE International Workshop Advanced Motion Control*, pp. 193–197, 2004.

[41] J. D. G. Kooijman, J. Merjaard, J. M. Papadopoulos, A. Ruina, and A. Schwab, "A bicycle can be self-stable without gyroscopic or caster effects", *Science*, vol. 332, pp. 339–342, 2011.

[42] L. Keo and M. Yamakita, "Controlling balancer and steering for bicycle stabilization", in *Proceedings of IEEE/RSJ International Conference on Intelligent Robots and Systems*, pp. 4541–4546, 2009.

[43] L. Keo and M. Yamakita, "Control of an autonomous electric bicycle with both steering and balancer controls", *Advanced Robotics*, vol. 25, no.1, pp. 1–22, 2011.

[44] Y. Zhang, J. Li, J. Yi, and D. Song, "Balance control and analysis of stationary riderless motorcycles", in *Proceedings of IEEE International Conference on Robotics and Automation*, pp. 3018–3023, 2011.

[45] Y. Zhang, K. Chen, and J. Yi, "Rider trunk and bicycle pose estimation with fusion of force/inertial sensors", *IEEE Transactions on Biomedical Engineering*, vol. 60, no. 9, pp. 2541–2551, 2013.

[46] K.J. Astrom, R.E. Klein and A. Lennartsson, "Bicycle dynamics and control", *IEEE Control Systems Magazine*, vol. 25, no. 4, pp. 26–47, 2005.

[47] D. J. N. Limebeer and R. S. Sharp, "Bicycles, motorcycles, and models", *IEEE Control System Magazine*, vol. 26, no. 5, pp. 34–61, 2006.

[48] Y. Tanaka and T. Murakami, "A study on straight-line tracking and posture control in electric bicycle", *IEEE Transactions on Industrial Electronics*, vol. 56, no. 1, pp. 159–168, 2009.

[49] J. Yi, D. Song, A. Levandowski, and S. Jayasuriya, "Trajectory tracking and balance stabilization control of autonomous motorcycles", in *Proceedings of IEEE International Conference on Robotics and Automation*, pp. 2583–2589, 2006.

[50] S. Lee and W. Ham, "Self-stabilzing strategy in tracking control of unmanned electric bicycle with mass balance", in *Proceedings of IEEE/RSJ International Conference on Intelligent Robots and Systems*, pp. 2200–2205, 2002.

[51] T. Fujikawa and S. Nakajima, "Proposal for an IR system to support automatic control for a personal mobility vehicle", in *Proceedings of the 2012 IEEE International Conference on Robotics and Biomimetics*, pp. 2207–2212, 2012.

[52] H. L Mohamed-Nour, J. W. Quigley, and R. Das, "Design considerations in an efficient electric motorcycle", in *Proceedings of the Battery Conference on Applications and Advances*, pp. 283–288, 1997.

[53] R. Nagendran and K. K. Senthil, "Hybrid electric bike with three speed transmission system an energy efficient bike for next generation", in *Proceedings of IEEE International Conference on Computer Engineering and Technology*, pp. 133–135, 2010.

[54] U. Nenner, R. Linker, and P. O. Gutman, "Robust feedback stabilization of an unmanned motorcycle", *Control Engineering Practice*, vol. 18, no. 8, pp. 970–978, 2010.

[55] T. K. Dao and C. K. Chen, "Path tracking control of a motorcycle based on system identification", *IEEE Transactions on Vehicular Technology*, vol. 60, no. 7, pp. 2927–2935, 2011.

[56] R. Frezza, A. Beghi, and A. Saccon, "Model predictive for path following with motorcycles: application to the development of the pilot model for virtual prototyping", in *Proceedings of IEEE Conference on Decision and Control*, vol. 1, pp. 767–772, 2004.

[57] T. Kimura, Y. Ando and E. Tsujii, "Development of new concept two-wheel steering system for motorcycles", *SAE Technical Paper*, No. 2013–32–9106, 2013.

[58] C. Nakagawa, Y. Suda, K. Nakano and S. Takehara, "Stabilization of a bicycle with two-wheel steering and two-wheel driving by driving forces at low speed", *Journal of Mechanical Science and Technology*, vol. 23, no. 4, pp. 980–986, 2009.

[59] H.G. Nguyen, J. Morrell, K. Mullens, A. Burmeister, S. Miles, N. Farrington, K.Thomas and D.W. Gage, "Segway robotic mobility platform", in *Proceedings of the International Society for Optics and Photonics*, pp. 207–220, 2004.

[60] K. Hirata and T. Murakami, "A realization of step passage motion in two-wheel wheelchair systems utilizing variable repulsive compliance control", in *Proceedings of the International Symposium on Industrial Electronics*, pp. 1–6, 2013 .

[61] D. Aiko, K. Hirata, and T. Murakami, "Analytical design of a robust motion controller for a two-wheeled wheelchair system", in *Proceedings of 16th International Conference on Advanced Robotics*, pp. 1–6, 2013.

[62] A. Nakamura and T. Murakami, "A stabilization control of two wheels driven wheelchair", in *Proceedings of IEEE/RSJ International Conference on Intelligent Robots and Systems*, pp. 4863–4868, 2009.

[63] X. Yun and Y. Yamamoto, "Internal dynamics of a wheeled mobile robot", in *Proceedings of IEEE/RSJ International Conference on Intelligent Robots and Systems*, pp. 1288–1294, 1993.

[64] K. Hirata and T. Murakami, "Stability analysis of disturbance observer based controllers for two-wheel wheelchair systems", *Advanced Robotics*, vol. 28, no. 7, pp. 467–477, 2014.

[65] T. Kawamura and T. Murakami, "Vibration suppression for uprising control of two-wheel driven wheelchair", in *Proceedings of the 37th Annual Conference of IEEE Industrial Electronics Society (IECON'11)*, pp. 3323–3328, 2011.

[66] A. P. KW and T. Murakami, "Vibration suppression of two-wheel mobile manipulator using resonance-ratio-control-based null-space control", *IEEE Transactions on Industrial Electronics*, vol. 57, no. 12, pp. 4137–4146, 2010.

[67] A. Dinale, K. Hirata, M. Zoppi, and T. Murakami, "Parameter design of disturbance observer for a robust control of two-wheeled wheelchair system", *Journal of Intelligent and Robotic Systems*, vol. 57, no. 12, pp. 4137–4146, 2010.

[68] M. Junichi, Y. Kaida, and T. Murakami, "$v - \dot{\phi}-$coordinate-based power-assist control of electric wheelchair for a caregiver", *IEEE Transactions on Industrial Electronics*, vol. 55, no. 6, pp. 2517–2524, 2008.

[69] S. Tashiro and T. Murakami, "Step passage control of a power-assisted wheelchair for a caregiver", *IEEE Transactions on Industrial Electronics*, vol. 55, no. 4, pp. 1715–1721, 2008.

[70] K. Nakano and T. Murakami, "An approach to guidance motion by gait-training equipment in semipassive walking", *IEEE Transactions on Industrial Electronics*, vol. 55, no. 4, pp. 1707–1714, 2008.

[71] S. Tsuyoshi and T. Murakami, "Power-assist control of pushing task by repulsive compliance control in electric wheelchair", *IEEE Transactions on Industrial Electronics*, vol. 59, no. 1, pp. 1707–1714, 2012.

[72] M. T. Ravichandran and A. D. Mahindrakar, "Robust stabilization of a class of underactuated mechanical systems using time scaling and Lyapunov redesign", *IEEE Transactions on Industrial Electronics*, vol. 58, no. 9, pp. 4299–4313, 2011.

[73] S. Riachy, Y. Orlov, T. Floquet, R. Santiesteban, and J. P. Richard, "Second order sliding mode control of underactuated mechanical systems I: local stabilization with application to an inverted pendulum", *International Journal of Robust and Nonlinear Control*, vol. 18, no. 4-5, pp. 529–543, 2008.

[74] J. X. Xu, Z. Q. Guo, and T. H. Lee, "Design and implementation of integral sliding-mode control on an underactuated two-wheeled mobile robot", *IEEE Transactions on Industrial Electronics*, vol. 61, no. 7, pp. 3671–3681, 2014.

[75] L. Marton, A. S. Hodel, B. Lantos, and J. Y. Hung, "Underactuated robot control: comparing LQR, subspace stabilization, and combined error metric approaches", *IEEE Transactions on Industrial Electronics*, vol. 55, no. 10, pp. 3724–3730, 2008.

[76] C. Acar and T. Murakami, "Underactuated two-wheeled mobile manipulator control using nonlinear backstepping method", in *Proceedings of the 34th Annual Conference of IEEE Industrial Electronics Society*, pp. 1680–1685, 2008.

[77] A. Ferreira, F. J. Bejarano, and L. M. Fridman, "Robust control with exact uncertainties compensation: with or without chattering", *IEEE Transactions on Control Systems and Technology*, vol. 19, no. 5, pp. 969–975, 2011.

[78] S. Lin, C. Tsai, and H. Huang, "Adaptive robust self-balancing and steering of a two-wheeled human transportation vehicle", *Journal of Intelligent and Robotic Systems*, vol. 62, no. 1, pp. 103–123, 2011.

[79] C. Yang, Z. Li, and J. Li, "Trajectory planning and optimized adaptive control for a class of wheeled inverted pendulum vehicle models", *IEEE Transactions on Industrial Electronics*, vol. 43, no. 1, pp. 24–36, 2013.

[80] O. Tomoaki and T. Murakami, "A stabilization control of bilateral system with time delay by vibration index-Application to inverted pendulum control", *IEEE Transactions on Industrial Electronics*, vol. 56, no. 5, pp. 1595–1603, 2009.

[81] A. Tsuchiya and T. Murakami, "Characteristic analysis of feedback control system with simplified disturbance compensator", in *Proceedings of the 29th Annual Conference of the IEEE Industrial Electronics Society*, vol. 3, pp. 2817–2822, 2003.

[82] E. Yamanaka, T. Murakami, and K. Ohnishi, "Cooperative motion control by human and mobile manipulator", in *Proceedings of the 7th International Workshop on Advanced Motion Control*, pp. 494–499, 2002.

[83] H. Ohara and T. Murakami, "Tracking control of a compact electrical vehicle trailer based on equivalent dynamics model", in *Proceedings of the 8th International Workshop on Advanced Motion Control*, pp. 183–186, 2004.

[84] M. Defoort and T. Murakami, "Sliding-mode control scheme for an intelligent bicycle", *IEEE Transactions on Industrial Electronics*, vol. 56, no. 9, pp. 3357–3368, 2009.

[85] Homepage of Berkeley Robotics & Human Engineering Laboratory
http://bleex.me.berkeley.edu/ (accessed: May 1, 2015)

[86] Homepage of CYBERDYNE Inc.
http://www.cyberdyne.jp/english/products/HAL/ (accessed: May 1, 2015)

[87] Homepage of RT. Works Co., Ltd.
http://www.rtworks.co.jp/ (accessed: May 1, 2015)

[88] Homepage of Murata Manufacturing Co., Ltd.
http://www.murata.com/ (accessed: May 1, 2015)

[89] Homepage of Toyota Motor Corp.
http://www.toyota.com.hk/innovation/ (accessed: May 1, 2015)

[90] K. Ohishi, K. Ohnishi, and K. Miyachi, "Torque – speed regulation of DC motor based on load torque estimation method", in *Proceedings of the International Power Electronics Conference, IPEC-Tokyo*, pp. 1209–1218, 1983.

[91] K. Ohnishi, "Robust motion control using disturbance observer", *Journal of the Robotics Society of Japan*, vol. 11, no. 4, pp. 486–493, 1993.

[92] K. Ohnishi, M. Shibata, and T. Murakami, "Motion control for advanced mechatronics", *IEEE/ASME Transactions on Mechatronics*, vol. 1, no. 1, pp. 56–67, 1996.

[93] T. Murakami and K. Ohnishi, "An adaptive force control of redundant manipulator based on joint acceleration controller", in *Proceedings of the International Conference on Industrial Electronics, Control and Instrumentation*, pp. 1043–1048, 1991.

[94] T. Murakami, F. Yu, and K. Ohnishi, "Torque sensorless control in multidegree-of-freedom manipulator", *IEEE Transactions on Industrial Electronics*, vol. 40, no. 2, pp. 259–265, 1993.

List of Achievements

Journal Papers

[1] Chuan Yang, and Toshiyuki Murakami, "Walking-Assist Principle Analysis for a Multi-Legged System," in *IEEJ Journal of Industry Applications*, vol. 4, no. 3, pp. 294–300, 2015. ISSN: 2187–1094

[2] Chuan Yang, and Toshiyuki Murakami, "Novel Walking Assist Device Based on Mobile Manipulator and Inertial Measurement Unit," in *IEEJ Journal of Industry Applications*, vol. 3, no. 5, pp. 381–387, 2014. ISSN: 2187–1094

Other Journal Paper

[1] Wonhee Kim, Chuan Yang, and Chung Choo Chung, "Design and Implementation of Simple Field-Oriented Control for Permanent Magnet Stepper Motors Without DQ Transformation," in *IEEE Transactions on Magnetics,*, vol. 47, no. 10, pp. 4231–4234, 2011. ISSN: 0018–9464

International Conference Papers

[1] Chuan Yang, Seonghye Kim, Takahiro Nozaki, and Toshiyuki Murakami, "A Self-Balancing Performance Comparison of Three Modes of Handleless Electric Motorcycles," in *13th IEEE International Conference on Industrial Informatics, INDIN 2015, Cambridge, UK*, (6 pages) July, 2015.

[2] Chuan Yang, and Toshiyuki Murakami, "A Study on Self-Balancing Electric Motorcycles with Two-Wheel Steering," in *7th International Conference on Information and Automation for Sustainability, ICIAfS 2014, Colombo, Sri Lanka*, pp. 1–6, Dec., 2014.

[3] Chuan Yang, and Toshiyuki Murakami, "An Approach to Walking Assist Control by a Multi-Legged System in Human Gait Motion," in *40th Annual Conference of the IEEE Industrial Electronics Society, IECON 2014, Dallas, TX, USA*, pp. 5236–5241, Oct., 2014.

Other International Conference Paper

[1] Toshiyuki Kurabayashi, Chuan Yang, and Toshiyuki Murakami, "An Advanced Position Control of Overhead Crane by Sway Suppression Method Emulating Natural Damping," in *International Power Engineering Conference, IPEC 2014, Hiroshima, Japan*, pp. 1962–1967, May, 2014.

Domestic Conference Paper

[1] Chuan Yang, and Toshiyuki Murakami, "A Novel Walking Assist Robot Based on IMU Sensor and Mobile Manipulator," in *Papers of the IEEJ Technical Meeting on Industrial Instrumentation and Control, Tokyo, Japan*, IIC 2013(159-164), pp. 23–28, Sept., 2013.

Other Domestic Conference Paper

[1] Chuan Yang, Won hee Kim, Dong Gyu Gang, Donghoon Shin, and Chung Choo Chung, "Position PID Control with Current PI for Stepper Motors," in *KIEE Summer Conference, Busan, Korea*, pp. 1637–1638, July, 2010.

Exhibition

[1] Chuan Yang and Toshiyuki Murakami, "Novel Walking Assist Device," in *14th Annual Keio Science and Technology Exhibition (KEIO TECHNO-MALL 2013), Tokyo International Forum*, Dec. 13th, 2013.